Formation of Meso-Structured Multi-Scale Porous Titanium Dioxide by Combined Soft-Templating, Freeze-Casting and Hard-Templating Using Cellulose Nanocrystals

Nizar Zahed

Thesis submitted to the faculty of the Virginia Polytechnic Institute and State University in partial fulfillment of the requirements for the degree of
Master of Science

in

Materials Science and Engineering

Carolina Tallón Galdeano

Earl J. Foster

Christopher R. Winkler

November 26, 2018

Blacksburg, Virginia

Keywords: titania, macrochannel, template-free self-assembly, cellulose nanocrystals, nanoparticles, mesoporous

Formation of Meso-Structured Multi-Scale Porous Titanium Dioxide by Combined Soft-Templating, Freeze-Casting and Hard-Templating Using Cellulose Nanocrystals

Nizar Zahed

Abstract (Academic)

This thesis identifies a facile and versatile technique for creating multi-scale porous titania with tunable meso-scale morphology. Three templating approaches were simultaneously utilized in achieving this; namely, soft-templating by template-free self-assembly of an aligned macroporous structure, freeze-casting for the preservation of particle dispersion found in suspension, and hard-templating by the use of cellulose nanocrystals (CNCs) as sacrificial material. A systematic study was conducted wherein three synthesis parameters (water content, alcohol solvent content, and drying method) were varied in the hydrolysis of titanium tetra-isopropoxide (TTIP) by the sol-gel method to determine their contribution to the formation of multi-scale porous titania exhibiting aligned macrochannels and mesoporosity. The optimal synthesis settings for producing multi-scale porous titania were identified as H_2O/TTIP molar ratio of 30, without any isopropanol (acting as solvent), and freeze-drying after freezing at -40°C. Subsequently, CNCs were added in various quantities (0-50vol%) to the hydrolysis of TTIP using these optimized settings to achieve more direct and precise control of the final titania meso-structure. Morphological studies revealed that the final titania bodies maintained the formation of macrochannels 1-3 μm in diameter as a result of hydrolysis in excess water in the absence of an organic solvent and exhibited successful templating mutually affected by CNC addition and freeze-casting. Freeze-drying preserved particle dispersion in the colloid suspension, hindering agglomeration otherwise found after oven-drying and enhanced the CNCs' role of disrupting titania aggregation and increasing interconnectivity. Thus, meso-structured multi-scale porous titania was prepared by a combined templating strategy using template-free self-assembly, freeze-casting, and CNC hard-templating.

Formation of Meso-Structured Multi-Scale Porous Titanium Dioxide by Combined Soft-Templating, Freeze-Casting and Hard-Templating Using Cellulose Nanocrystals

Nizar Zahed

Abstract (General Audience)

Titanium dioxide (TiO_2) has been shown to exhibit desirable properties including physical and chemical stability and biocompatibility making it a material of great interest in a variety of fields including pigments and biomedicine. Furthermore, the material's photocatalytic activity (i.e. ability to absorb light energy to generate usable charge) has led to its implementation in solar cells, in the production of hydrogen as an eco-friendly fuel, and in decontaminating water from organic pollutants. While TiO_2 has shown great promise in these applications, there remains a need to identify a simple strategy to synthesize TiO_2 with a tunable multi-scale porous structure with pores of different sizes and shapes to improve its performance. To this end, a facile and versatile procedure was used to prepare multi-scale porous TiO_2 with tunable morphology. In investigating the effect of water content, alcohol content and drying method on the final morphology, a multi-scale structure was achieved by synthesizing TiO_2 in the absence of an alcohol solvent and within a new moderate range of water content that had not been previously explored. Lacking an effective and easy strategy to further manipulate the multi-scale morphology, this self-assembly technique was modified by incorporating cellulose nanocrystals (CNCs) into the synthesis procedures to further tune the structure on the nanometric scale by altering the final porosity and surface area. The final TiO_2 samples exhibited multi-scale porous structures that could be manipulated by combining the self-assembly and CNC-templating techniques in an adaptable strategy to tailor the TiO_2 morphology for its various uses in photocatalysis and biomedicine.

Acknowledgements

I would like to thank the Materials Science and Engineering (MSE) department for providing me with a GTA position which helped tremendously in covering the costs of pursuing my Master's degree. I am also grateful to the Dr. Gary S. Clevinger, Sr. Memorial Endowed scholarship for the award which further assisted in funding the degree.

Additional thanks are owed to the MSE department for their support and for providing some of the instruments necessary for completing the work herein presented. I would like to specifically acknowledge Dr. Thomas Staley and Hesham Elmkharram for their assistance, training, and counsel on the BET and XRD machines, respectively. I would also like to acknowledge Steve McCartney and Dr. Chris Winkler at the Nanoscale Characterization and Fabrication Laboratory (NCFL) for their assistance and expertise on the SEM and TEM. Additional thanks are owed to Dr. Chris Winkler for capturing all the TEM images used in analyzing and characterizing samples and for serving on my review committee.

I would like to thank Dr. Carolina Tallón and Dr. E. Johan Foster for their continued support and invaluable guidance during my pursuit of this degree. The work described in this thesis document would not have been possible without their counsel and encouragement.

I would like to acknowledge the Foster Advanced Materials Group and the Tallón Research Group for their support, assistance and comradery inside and outside the lab. I specifically want to name David Hicks for writing the "pore-gram" which I used to analyze the macrochannels observed in this work.

Finally, I would like to thank my family and friends for their unwavering support. I would like to specifically acknowledge my brother Malek Zahed, Priya Venkatraman, Rose Roberts, and Tamy and Pedro Guimaraes whose friendship, advice, and ideas were indispensable.

Table of Contents

List of Figures

List of Tables

Common Abbreviations

TTIP — Titanium tetra-isopropoxide

IPA — Isopropyl alcohol / Isopropanol

CNC — Cellulose nanocrystals

FD — Freeze-dried

OD — Oven-dried

RT — Room temperature dried

SEM — Scanning electron microscope/microscopy

TEM — Transmission electron microscope/microscopy

XRD — X-ray diffraction

BET — Brunauer-Emmett-Teller

BJH — Barrett-Joyner-Halenda

SSA — Specific surface area

G — Green (dried sample before sintering)

S — Sintered

Chapter 1. Introduction

Ceramics constitute a class of materials that are generally characterized by their strong and brittle behavior, thermal resistant properties, and superior performance at elevated temperatures. Traditional ceramics such as clay, cement, and porcelain have been around for millennia and have found applications that range from structural products to thermal barriers and abrasives. However, in the past century, closer investigation of this class of materials and control of the structure and processing have revealed a host of tunable properties. This has allowed the development of a new category of advanced and functional ceramics to be applied to the fields of aerospace, electronics, communication, bioengineering, and energy harvesting.

Porous ceramics in particular have received much attention for their potential use in a wide variety of fields ranging applications in fluid filtration (water, air, and molten metal) [1–7], biomedicine [8, 9], electronics [10, 11], and aerospace [12]. Control of the porous structure in a ceramic body allows for the tailoring of the sample for certain applications, which may require different pore characteristics and pore generation schemes for optimal performance.

1.1. Pore Characterization and Terminology

As Franks et al. describe, there are three main characteristics to define porosity: size, type, and distribution [13]. The International Union of Pure and Applied Chemistry (IUPAC) has assigned the terms “micropore,” “mesopore” and “macropore” for classifying pore size [14]. Micropores exhibit pore diameters less than 2 nm and macropores have pore sizes larger than 50 nm, while mesopores are pores with sizes lying within the range of 2-50 nm. The smaller dimensions of micro- and mesopores grant them large surface-to-volume ratios, making them principal contributors to a porous material’s surface area and instrumental in preparing efficient catalyst materials. The larger macropores offer more substantial pore volume, have more suitable dimensions for cell scaffolding [8] and can assist with fluid transport such as in photocatalytic water purification [15], electrolyte diffusion in Li-ion batteries [16] and actively cooled ceramics in ultra-high temperature environments [17].

IUPAC further categorizes a pore as open or closed based on whether or not it is accessible by fluid transport from the external surface of the body. Open pores are required for applications such as fluid filtering, biomedicine, and photocatalysis for which the success of the material necessitates fluid flow from the exterior environment into the sample via these open pores. On the other hand, a closed pore is isolated from other pores and the external surface and is entirely encircled and blocked by the solid material. Closed pores are typically not desired when they occur as a result of insufficient densification, but are useful in preparing thermally insulative materials [18]. Along with "open" and "closed" porosity, Franks et al. also list "cellular" porosity as a pore type [13]. Green and Colombo discussed materials with cellular porosity and described these materials as being more than 70% porous and exhibiting large pores and narrow pore walls [19]. These are characteristic of emulsion-templated ceramics and find applications in thermal insulation [20] and molten-metal filtration [21] among others. These three porosity types are represented in Figure 1.1 (I, II).

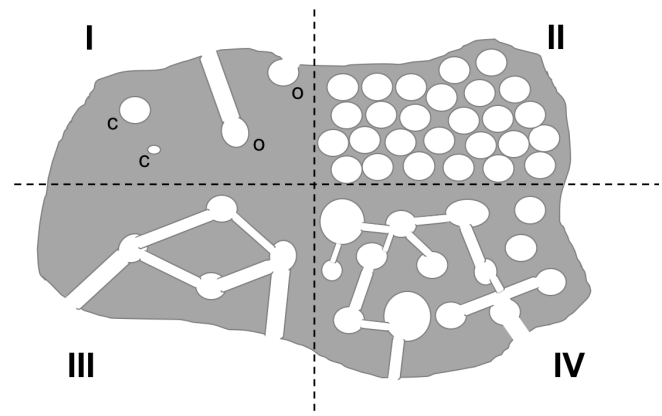

Figure 1.1: Schematic of the various pore characteristics. Quadrant I shows the difference between open (o) and closed (c) pores. Quadrant II represents cellular porosity. Quadrant III is an example of interconnected porosity. Quadrant IV represents multi-scale porosity with a collection of open, closed, and interconnected pores of varying sizes

Porosity can additionally be characterized by its distribution. Interconnected porosity is one in which there exists a path connecting a series of open pores as schematically shown in Figure 1.1 (III). This is a crucial feature for applications that depend on material and fluid interactions such as biomedical scaffolds and photocatalysis. Samples exhibiting multiple-sized pores can be classified as hierarchical or multi-scale. The differentiating factor is that hierarchical porosity necessitates pores of the same type (open, closed, or cellular), while multi-scale porosity, as shown in Figure 1.1 (IV), is associated with materials of differently sized and typed pores. Materials exhibiting multi-scale or hierarchical porosity (often used interchangeably in literature) have garnered much attention in recent years for their advantageous properties and improved efficiency in catalytic applications [15, 22], biomedicine [8, 9], and sensing [23, 24].

There are various methods to produce porous ceramics, but preparation of multi-scale porous materials usually requires more labor-intensive procedures.

1.2. Processing Techniques of Porous Ceramics

Ceramics with tunable porosity and morphology are commonly prepared in suspensions because colloidal processing offers a versatile technique that is easily scalable. Therefore, understanding colloidal processing techniques for stabilizing particle dispersions is fundamental.

1.2.2. Colloidal Processing

Colloidal processing involves the suspension of ceramic particles, typically smaller than a few micrometers, in a solvent and whose motion is characterized and determined by Brownian mechanics and interparticle forces. When the particles are too large or interparticle forces are not well managed and cause the formation of aggregates, gravity forces overwhelm the interparticle forces and result in unstable conditions and sedimentation. Therefore, colloidal suspensions are stabilized by manipulating attractive-repulsive forces to prevent aggregation of particles. Attractive forces by van der Waals interaction are always in effect. If unchecked, these forces lead to particle agglomeration, risking the stability of the colloidal system and resulting in random and unregulated particle assemblies and morphologies [13]. In turn, this jeopardizes the effectiveness of templating strategies used in preparing porous ceramic materials.

Ceramic nanoparticles in aqueous suspensions inherently possess surface charges, owing to their interactions with water molecules in the form of adsorption and dissociation [13, 25]. For example, surface hydroxyl groups may experience the following surface interactions [13]:

Acidic environment: $M–OH + H^+ \rightarrow M–OH_2^+$ (Eq. 1.1)

Basic environment: $M–OH + OH^- \rightarrow M–O^- + H_2O$ (Eq. 1.2)

By whichever avenue these surface charges form, a mixture of ceramic particles in a suspension may exhibit positively and negatively charged surfaces, whose ratio depends on the pH of the suspension. The pH at which the surface charges are completely balanced is known as the isoelectric point (IEP) or point of zero charge (PZC). Below the IEP, particles have a net positive surface charge, whereas pH values above the IEP cause particles to take on a net negative surface charge. Quantification of surface charge in suspension can be conducted using a combination of

dynamic light scattering and electrophoresis to calculate the zeta-potential (ζ-potential), or electrical potential difference between the particle surface and the suspension medium (solvent). Hence, the IEP coincides with the pH value for which the zeta-potential is zero.

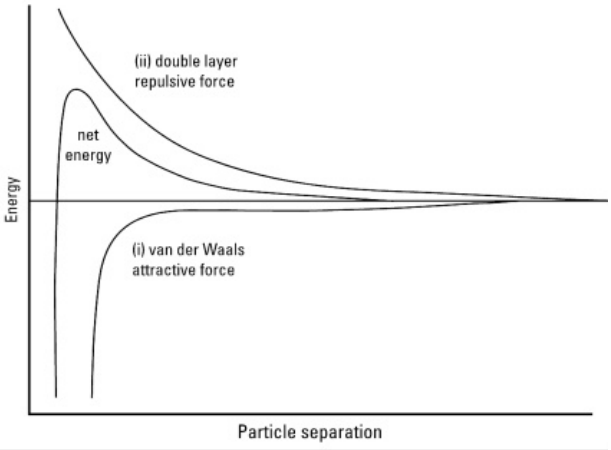

Figure 1.2: Dependence of (i) van der Waals attractive forces, (ii) double layer (EDL) repulsive forces, and net energy on the particle separation distance show a maximal repulsive force at a critical distance below which van der Waals forces dominate [28]

The surface charges which form comprise the first of an electrical double layer (EDL) constituting the Derjaguin-Landau-Verwey-Overbeek (DLVO) theory governing colloidal stability [26, 27]. A layer of counterions originating from the suspension are attracted to the oppositely charged surface to form a diffuse second layer. This EDL promotes the stability of the suspension by Coulombic repulsive forces of like-charged layers. Figure 1.2 qualitatively shows the dependence of van der Waals attractive and double layer (EDL) repulsive energies on the interparticle distance. Therefore, one method of ensuring colloidal stability is by electrostatic stabilization in which suspension pH is adjusted appropriately such that it does not coincide with the IEP to cause surface charges, forming an EDL to overcome the ubiquitous van der Waals attractive forces (see Figure 1.3a for schematic representation) [29–31]. Thus, manipulation of solid particle surface charges allows the stabilization of a colloidal suspension and control of interparticle interactions and can be achieved by considering the isoelectric point and adjusting suspension pH accordingly.

Particle surface charges can also be used to adsorb surfactants and manage repulsive forces by steric interactions [31, 32]. The adsorbed surfactant molecules contribute to the repulsive forces in two ways: (1) the molecule wants to maintain its natural shape and will repel any particle from attempting to change its shape as schematically represented in Figure 1.3b; (2) when the molecule is large enough, it can hinder van der Waals attraction between particles by preventing the particles from reaching the critical interparticle distance at which these attractive forces begin to dominate (Figure 1.2). Introduction of surfactants to sterically manipulate the

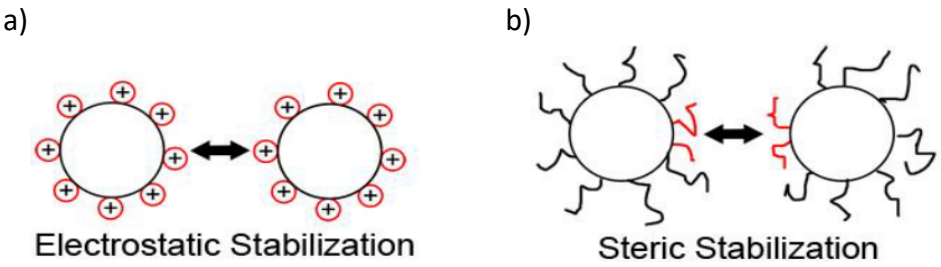

Figure 1.3: Schematic of particle-particle interactions stabilized by a) electrostatic and b) steric repulsion mechanisms [33]

interparticle repulsion forces presents another method to stabilize a colloidal suspension of ceramic nanoparticles.

Colloidal processing and stabilization techniques are significant factors in preparing porous ceramics as they grant control over particle-particle interactions in suspension and provide tunability of particle packing and morphology. Moreover, colloidal processing of ceramic suspension is a versatile technique with high tolerance for additives, shaping strategies, and various templating approaches.

1.2.3. Soft-Templating

Soft-templating presents one of the least complex templating methods to prepare porous ceramics, wherein surfactants and dispersants are typically used as stabilizers and pore-directing agents. In particular, amphiphilic surfactants have been used to stabilize mixtures of hydrophilic and hydrophobic domains and produce pores by removing of one of the phases. For example,

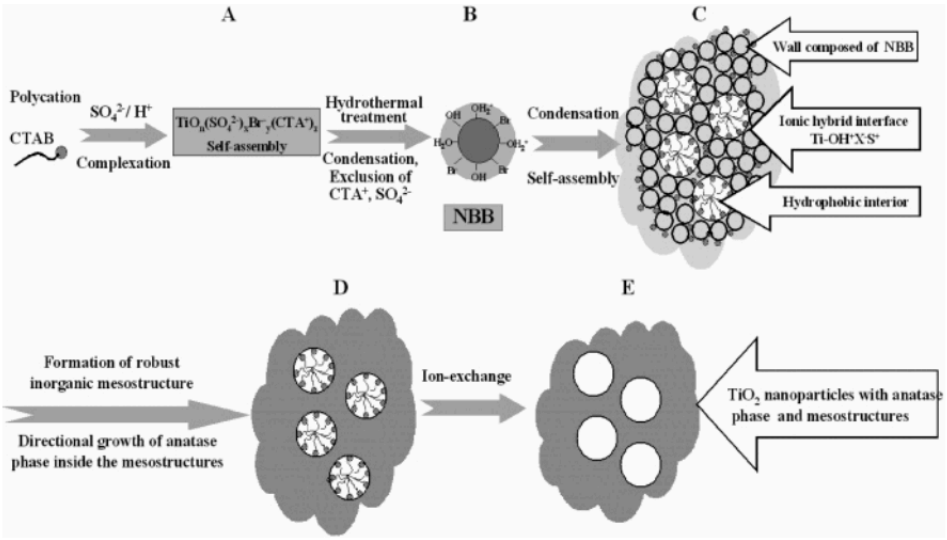

Figure 1.4: Formation mechanism of the production of mesoporous titania using CTAB as a directing and pore-forming agent (reprinted with permission from ref. [34]; copyright 2005 American Chemistry Society)

Peng et al. used cetyltrimethylammonium bromide (CTAB) as a directing and pore-forming agent to produce mesoporous titania with a stable wall of anatase titania nanoparticles [34]. This was achieved according to the mechanism in Figure 1.4 by the adsorption of the CTAB cationic head to the negatively charged nanoparticle surface and arrangement of CTAB tails into hydrophobic spheroidal domains. Subsequent ion-exchange treatment removed the surfactant and resulted in the mesoporous structure. A similar technique is used in employing surfactants to stabilize emulsions for forming ceramics exhibiting cellular porosity.

1.2.3.1. Emulsion Formation

Surfactants are often used to stabilize emulsions for pore generation in colloidal suspensions, usually resulting in a ceramic exhibiting cellular porosity. The foams can be generated by either introducing gas bubbles into the suspension [35, 36] or mixing immiscible liquids to form oil-in-water type emulsions [37, 38]. The preferential interaction of particles with one phase and removal of the other phase leads to the formation of the porous structure. De Moraes et al. synthesized silicon nitride (Si_3N_4) foam by the emulsification process with the mixture of immiscible liquids [37]. Dispersion of colloidal particles was assisted by thermally treating Si_3N_4 powders to form a silica layer at the surface and by addition of PAA to the suspension. Octane was added to form an emulsion in the aqueous suspension, which was stabilized by the nonionic surfactant Tween 80 and subsequently dried in air and rapidly sintered in vacuum. This resulted in highly interconnected porosity with a cellular porous structure with upwards of 80% porosity. The authors found that the porosity could be tailored within the range 79-86% by varying the amount of octane added (50-70 vol%), while emulsion pore size could be tuned with stirring velocity. Towata et al. used melted paraffin in water and stabilized this emulsion with surfactant sodium di(2-ethyl- hexyl) sulfosuccinate to create porous zirconia [38]. A mixture of the immiscible liquids and the surfactant was prepared at elevated temperature and sonicated for 30 minutes to incorporate small paraffin emulsions in water before the solution was quickly cooled to solidify the paraffin droplets in suspension. A mixture of zirconium normal butoxide and stabilizer triethanolamine in water was prepared and mixed with the paraffin-water emulsion to hydrolyze the zirconia precursor and allow its deposition on the paraffin droplets. Heat treatment crystallized the zirconia particles and removed the paraffin emulsion template

leaving behind a zirconia body with cellular porosity, whose pore size could be tailored between 20 nm and 2 µm by varying the amount of surfactant added as can be seen in Figure 1.5.

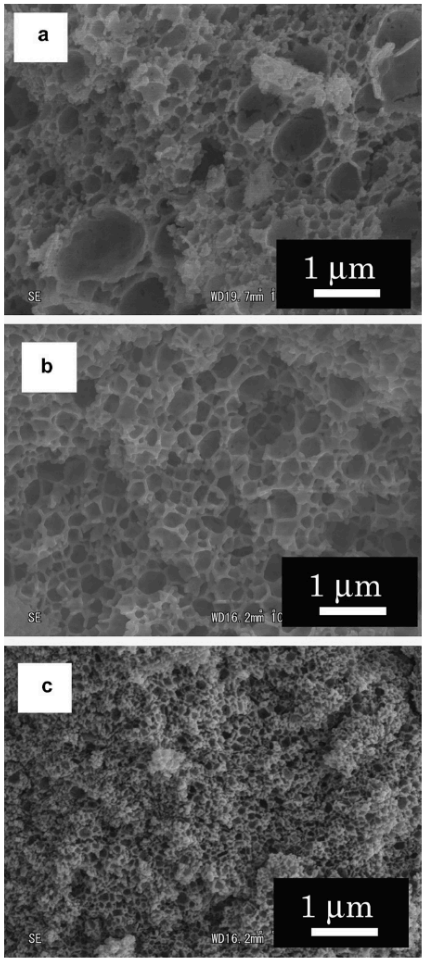

Figure 1.5: SEM images show change in emulsion cell size with increasing concentration of surfactant [38]

An alternative method for emulsifying colloidal suspensions is through foaming by introduction of gas from an external source, such as by agitation or its generation internally as a byproduct of an intermediate reaction. Sepulveda et al. introduced gas bubbles into a colloidal suspension by foaming an aqueous suspension of hydroxyapatite (HA) by agitation with a double-blade mixer and stabilized the emulsion with nonionic surfactant Tergitol TMN10 [35]. Gel-casting by in-situ polymerization of acrylic monomers and subsequent drying and sintering produced highly porous HA with relative porosities ranging 72-90%, minimal closed porosity, high surface area, variable permeability, and good mechanical properties. Aside from agitation, foams can be prepared by the formation and containment of gas bubbles produced by an intermediate reaction within the precursor suspension. Idesaki and Colombo used this alternative method to synthesize Ni-containing SiOC foams for hydrogen production [36]. A mixture of polyphenylmethylsiloxane (PPMS), nickel (III) acetylacetonate ($Ni(acac)_2$) and azodicarbonamide (ADA) was prepared and heat treated at 250°C to intrinsically produce gas bubbles by the decomposition of ADA and the polycondensation reaction of the polymer precursor [39]. The cross-linking behavior of molten PPMS contained the gas bubbles within itself and the foamed PPMS was either extracted by ethanol or directly pyrolyzed in an argon atmosphere to produce SiOC containing nitrogen sourced from $Ni(acac)_2$. The authors concluded that while all samples tested exhibited large porosity (70-78%), ethanol extraction resulted in the largest composition of open porosity (70%).

Thus, emulsion formation for preparing porous ceramics can be achieved by mixing two immiscible liquids to form an oil-in-water type emulsion or by introducing and stabilizing gas bubbles in the suspension. The preferential interaction of solid particles with one phase produces highly porous bodies exhibiting cellular porosity in the macropore size range. However, it is very difficult to template mesopores and, by extension, a multi-scale porous structure with this technique.

1.2.3.2. Template-Free Self-Assembly

One of the simplest processes in soft-templating corresponds to the template-free synthesis of porous ceramics. The generation of the porous structure usually is initiated by (often chemical) interaction between reacting species and leads to the template-free fabrication of porous ceramics. Ghosh, Roy, and Naskar prepared uniquely structured, mesoporous CuO with dumbbell-like morphology by the hydrothermal treatment of $Cu(NO_3)_2$ [40]. The precursor was dissolved in water with urea and calcined at 300°C after hydrothermal treatment, resulting in the oriented growth of rod-shaped particles and their self-assembly into the dumbbell morphology with an average pore size of 23 nm. The authors offered a formation mechanism attributing the unique morphology to the presence of urea and the interaction of its decomposition products with the ceramic precursor in the aqueous medium. This led to the self-assembly of CuO without the need for a template or surfactant. Yang et al. also used urea in the formation of self-assembled ferric oxide (α-Fe_2O_3) microspheres with unconventional morphology [41]. These mesoporous ceramic structures were synthesized by the hydrothermal treatment of $FeSO_4 \bullet 7H_2O$ with ascorbic acid and urea in water and subsequent calcination of resultant $FeCO_3$ at 500°C. The authors found that the morphology seen in Figure 1.6 and phase composition can be tailored such that homogeneous microspheres composed of "trilobed wheel-like structures" could be formed at moderate reaction temperatures and urea content. Liu et al. prepared

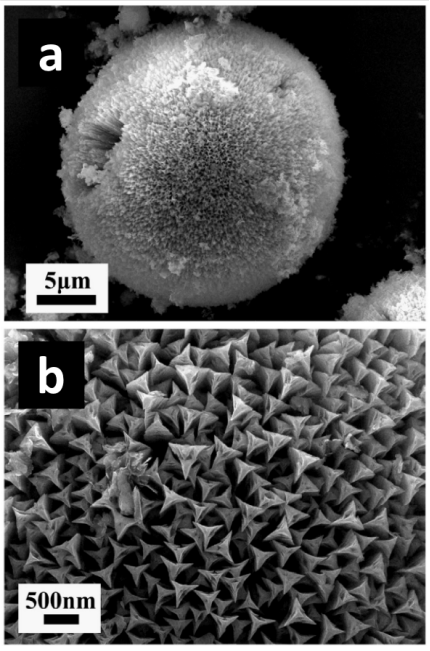

Figure 1.6: Morphology of hierarchical Fe_2O_3 prepared by template-free self-assembly in the presence of urea [41]

hierarchically porous vanadium nitride (VN) by nitration-induced phase separation at high temperature. The authors mixed aqueous solutions of $Zn(NO_3)_2 \bullet 6H_2O$ and NH_4VO_3 before aging and drying the mixture to form $Zn_3(OH)_2(V_2O_7) \bullet (H_2O)_2$ microspheres [42]. Annealing of these spheres in a NH_3 environment at 650°C led to the selective removal of a ZnO sacrificial phase and gave way to the production of hierarchically nanostructured VN microspheres. Literature reports of the template-free synthesis of porous ceramics have shown its great potential in producing hierarchical and multi-scale porous structures initiated by interactions among reactive species that cause unique morphologies simultaneously at the meso- and macro-scales.

Despite this plethora of techniques, soft-templating generally does not grant good pore definition nor direct control of pore generation. Pores form from the arbitrary arrangement of surfactant-stabilized emulsions or anarchic reagent interactions and phase-separated domains. Although numerous additives can be used to try to manage pore generation, this would negate the simplicity of the soft-templating technique, making it equal in complexity to alternative templating methods. Moreover, packing of particles during drying occurs randomly and cannot be precisely controlled. The template-free approach is a promising option for producing multi-scale porous ceramics. However, the lack of control over the mesostructure and a one-to-one pore-templating method leading to less defined pores require addressing.

1.2.4. Hard-Templating

As an alternative technique, hard-templating makes use of sacrificial material that can be faithfully mimicked to create positive or negative replicas whose morphology is directly controlled by the chosen template. Hard-templating requires the preparation of the template structure, its impregnation by a ceramic precursor solution, its extraction by thermal or chemical treatment, and synthesis of the desired ceramic chemistry and crystallinity. A multitude of templates have been used to produce porous ceramic materials ranging from polymer microspheres to biological structures and other porous ceramic morphologies.

1.2.4.1. Polymer Templates

Polymer templates exhibiting different structures have been employed as hard-templates for production of porous ceramics. One benefit of using polymeric materials is that they can be easily removed by heat treatment to simultaneously decompose the template and sinter the

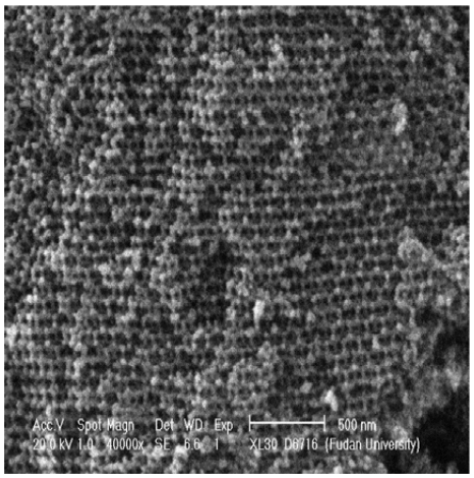

Figure 1.7: Cellular porosity of titania by hard-templating of PS spheres [43]

ceramic material in a single step. Fu et al. took advantage of this technique to synthesize mesoporous titania using polystyrene microspheres (PS) [43]. The microspheres were prepared by emulsion polymerization and packed by water solvent evaporation. The packed PS spheres were then soaked in a titania precursor solution and centrifuged three times before being calcined to simultaneously remove the polymer template and produce mesoporous anatase titania. The titania structure faithfully replicated the negative space of the packed PS spheres as shown in Figure 1.7 and produced titania walls with cellular porosity whose pore size corresponded directly to the size of the polymer template. Another benefit of polymeric materials is that they can take on numerous forms (e.g. microspheres, fibers, sponges), making them versatile hard-templates to create ceramic materials with various morphologies. Medri, Mazzocchi and Bellosi prepared ZrB_2-based sponges using various templates and techniques, including two commercially available polyurethane (PU) ester reticulate foams with different pore sizes [12]. Previously prepared raw material powder was suspended in an aqueous slurry using polyelectrolyte for electro-steric stabilization, Dolapix PC33 as dispersant and added high molecular weight polyacrylic acid to improve the adhesion of the slurry to the templates used. The porous ceramic bodies were prepared by dipping the PU sponges in the slurry, draining any excess from the template, drying and sintering at 500°C. The resultant ceramic sponges faithfully replicated the different PU templates used and exhibited over 85% porosity. Thus, the properties and performance of the final ceramic can be readily tuned by making appropriate adjustments to the template morphology. This fine tunability of morphology and ability to remove the template in a single burn-out and sintering step due to polymers' relatively low decomposition temperatures make polymer materials a relatively easy-to-work-with option for templating porous ceramic materials.

1.2.4.2. Ceramic Templates

As a substitute for polymers, porous ceramic materials can serve as templates for production of other porous ceramics. Ceramic templates are sometimes preferred over polymer ones to ensure faithful replication of the template morphology during sintering of the precursor material by eliminating the risk of structure collapse from premature template removal. Moreover, while certain templating techniques may result in the desired morphology, they may not be universally suitable for all synthesis routes and ceramic chemistries. In these cases, the use of an intermediate template can be employed to attain the desired structure in the final material. For example, silica is often used as an intermediate template for the fabrication of porous titania due to the latter's volatile and difficult-to-manage synthesis. Lee et al. synthesized porous titania by a two-step hard-templating approach consisting of producing mesoporous silica and its use as a template for mesoporous titania [44]. This was achieved by preparing a stable colloidal dispersion of silica nanospheres from the base-catalyzed hydrolysis-condensation reaction of tetraethyl orthosilicate (TEOS) followed by addition of citric acid (CA) as a non-surfactant template. Subsequent drying and calcining formed CA-templated mesoporous silica (CMS), whose pores directly correlated to the distribution of CA in the composite. For the second templating step, the authors impregnated the CMS with a titanium isopropoxide (TTIP) ethanolic solution and submerged this TTIP-CMS composite in a water/ethanol solution to hydrolyze the TTIP precursor before calcining the ceramic composite. Extraction of the silica intermediate template was performed by chemical etching with NaOH, resulting in mesoporous titania. Electron microscopy (Figure 1.8) revealed that the final titania bodies exhibited a network of interconnected mesopores in place of the silica template. Thus, Lee et al. produced a positive replica of citric acid by the use of silica as an intermediate hard-template. In some instances, morphology unique to a particular ceramic material may serve to be advantageous in another material that exhibits more

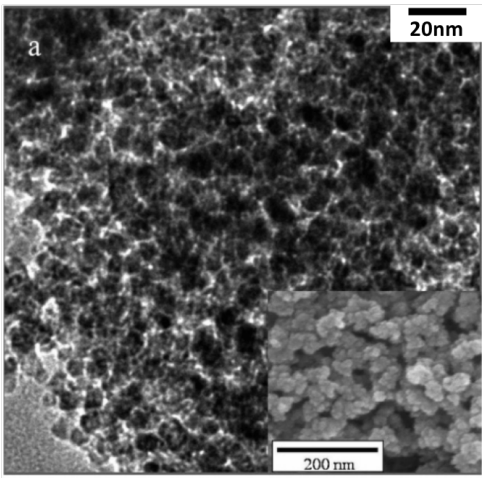

Figure 1.8: TEM and SEM (inset) images show mesoporous titania by two-step hard-templating of citric-acid templated silica (adapted with permission from ref. [44]; copyright 2007 American Chemistry Society)

interesting application potential. Zhao et al. synthesized mesoporous silica shells for drug release by hard-templating of hematite (Fe_2O_3) spheres and spindles [45]. Previously prepared hematite particles were dispersed in a basic solution of isopropyl alcohol, water and ammonia before dropwise addition of a TEOS and n-octadecyltrimethoxysilane (C18TMS) mixture. Coated particles were collected, calcined at 550°C, and etched with HCl, leaving behind the mesoporous silica shells, which exhibited large surface area values (350-650 m^2/g), high drug storage capacity, and tunable shell thickness as a function of precursor solution composition. With hematite determining the macrostructure and C18TMS serving as the meso-template, this dual templating allowed the formation of these multi-scale porous silica shells. However, unless multiple templates are used, hard-templating usually results in a single-scale porous structure.

1.2.4.3. Bio-templates

Recent attention has been directed at natural biomaterials as templates due to their naturally occurring, evolutionarily advanced and often hierarchical morphologies. Shin and Exarhos used the porous structure of poplar and pine wood as a template to create SiO_2 and SiC replicas [46]. Pieces of wood were soaked in a precursor solution for several hours before being dried and calcined to remove the wood template. Figure 1.9 shows that the authors could influence whether a positive or negative replica was generated by controlling the pH of the precursor solution. SEM images showed that when wood was soaked in an acidic solution, a positive silica replica formed, whereas a negative replica resulted from soaking in neutral and basic solutions. Biomorphic SiC structures were produced in a similar fashion by thermally treating the dried precursor-wood composites in a tube furnace in the absence of oxygen to

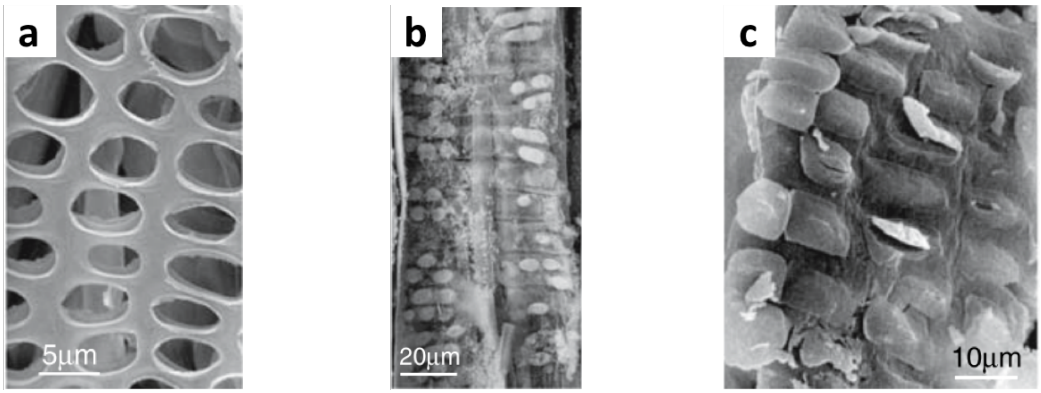

Figure 1.9: Silica replica of poplar wood produced in a) acidic, b) neutral, and c) basic precursor solutions [46]

promote the carbonization of silica with the wooden templates. Thus, the authors prepared SiO_2 and SiC bodies exhibiting hierarchical structures whose morphology could be tailored by choice of wooden template and by appropriately adjusting pH of the dip solution. Similarly, Sieber and colleagues infiltrated rattan plants with alumina, mullite, and zirconia solutions to mimic its naturally occurring porous structure [47]. The authors achieved this by the sol-gel reaction of ceramic precursors, numerous infiltration processes, pyrolysis of composite samples, and final sintering for full template removal. The porous ceramic bodies exhibited 75-94% porosity, but maintained high relative densities within the skeletal structure of the samples due to the repeated infiltration of precursor solutions at various stages in the experimental procedure. The work done by Sieber et al. [47] shows the versatility of the bio-templating technique in generating and replicating hierarchical structures across various ceramic materials. Biomaterials have been shown to be very promising hard-templates for porous ceramic materials and serve as molds to replicate the evolutionarily advantageous hierarchical structures found in nature.

1.2.5. Freeze-Casting

Freeze-casting (also known as ice-templating) has garnered some momentum in recent years in the fabrication of porous ceramic materials [48–52]. Freezing of solvent and subsequent sublimation provides multiple advantages over traditional solvent removal methods, particularly in the fabrication of porous ceramic materials. For example, rapid freezing can prevent particle aggregation and sedimentation by locking in place the dispersion of particles as they are positioned in the colloidal suspension. Thus, freeze-casting can preserve the particle distribution and results in mesoporous structures [49, 53]. At slower freezing rates and when the freezing is applied from a particular location, ice growth can occur directionally resulting in aligned pores after drying. This technique is most often used when ice-templating macroporous ceramic materials.

Naglieri et al. studied the ice-templating behavior of a SiC aqueous system [54]. SiC powder mixed with alumina and yttria, which served as sintering aids, was suspended in water at various solid loadings using polyethylene glycol as an organic binder at pH of 10 (adjusted with ammonium hydroxide). The suspension was directionally frozen at varying cooling rates before being freeze-dried, treated at 450°C for binder burn-out and sintered in argon at elevated

temperatures. The authors concluded that ice growth behavior transformed from lamellar to dendritic to isotropic in nature with increasing solid content and cooling rate allowing them to control solid lamella thickness and spacing. Ice growth behavior can also be changed using additives. Ren, Zeng, and Jiang ball-milled commercial TiO_2 powder with poly(vinyl alcohol) (PVA) and dispersant ammonium polyacrylate in water to obtain a stable dispersion, which was then directionally frozen at -18°C, freeze-dried, and sintered at 1000°C [55]. They studied the effect of changing the PVA amount on the freezing behavior and found that, as can be seen in Figure 1.10, increasing the PVA content resulted in more columnar ice growth instead of dendritic growth as evidenced by the dried samples. Thus, the growth of ice crystals during freezing of colloidal suspension and by extension the pore characteristics of the final ceramic can be tuned by adjusting the suspension parameters (solid loading, freezing rate, binder addition) to produce the desired porosity. Even so, ice-templating at relatively slow freezing rates alone typically produces macroporous structures, while mesoporosity can be achieved by accelerated freezing and preservation of particle dispersion in the colloidal suspension.

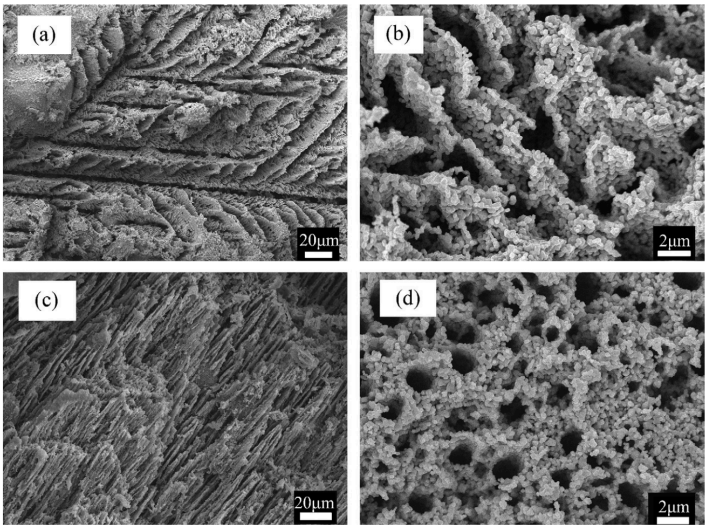

Figure 1.10: SEM images of ice-templated titania show the dependence of ice-growth behavior and final morphology on PVA content at (a, b) 3wt% and (c, d) 6wt% [55]

1.2.6. Combined-Templating

In an attempt to combine the advantages of individual methods, some groups have investigated the simultaneous use of multiple templating techniques to prepare multi-scale porous ceramics. Hu et al. used polymeric microspheres as a hard-template and amphiphilic triblock copolymer Pluronic P123 as surfactant to produce 3D ordered macro-/mesoporous TiO_2 [56]. As sacrificial material, they chose PMMA spheres synthesized by an emulsifier-free emulsion polymerization process and soaked them with a titania precursor solution containing the P123 surfactant. After thermal treatment and soft- and hard-template removal, a multi-scale porous

titania structure formed with cellular macropores as faithful replicas of the PMMA spheres and mesopores in the struts as a result of steric repulsive forces induced by P123. Naglieri and Colombo combined the emulsion and ice-templating techniques to produce hierarchically porous SiC microspheres [57]. Polycarbosilane (PCS) was dissolved in cyclohexane and slowly added into an aqueous solution of nonionic surfactant Tween 80 to form a surfactant stabilized oil-in-water emulsion. This mixture was directionally frozen and freeze-dried to remove the water and cyclohexane solvents from the emulsion and continuous phases. After oxidation and sintering in argon, the remaining solids exhibited hierarchical porosity consisting of directionally porous microspheres. As can be seen in Figure 1.11, by changing the freezing and sintering temperatures, the authors could tailor the hierarchical porosity of the final ceramic microspheres, which exhibited relatively high surface areas. Although limitations of individual templating techniques restrict the preparation of multi-scale porous ceramics, it has been shown that a combination of non-competing templating techniques, such as freeze-casting, template-free soft-templating, and use of a nanometric sacrificial material, can grant a method for producing and tuning multi-scale porosity in a ceramic body via colloidal processing.

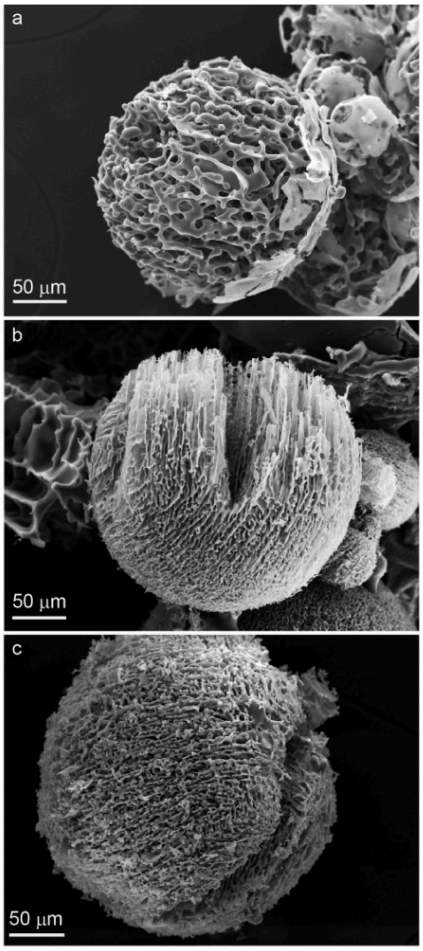

Figure 1.11: Hierarchically porous SiC microspheres prepared by combined emulsion formation and ice-templating at a) -30°C, b) -60°C, and c) -100°C [57]

1.3. Titanium Dioxide (titania, TiO_2)

Recent attention in the past few decades has been directed at titanium dioxide (titania, TiO_2) as a ceramic of interest for numerous applications because it is cheap, chemically and physically inert, and biocompatible. These properties lead to the implementation of titania in various fields, ranging from its use as a pigment in paints and as a UV-blocking agent in sunscreens [58, 59], to biomedicine for tissue engineering, biosensing and drug delivery systems [8, 9]. Furthermore, the energy band gap of 3.2 eV of its metastable anatase phase allows this oxide to

serve in multiple photoelectric applications, including as an electrode material for Li-ion batteries [10, 11], and as a photocatalyst material in dye sensitized solar cells [60, 61], for hydrogen gas generation via water splitting [62–65], and water/air purification by decomposition of selective organic pollutants [66, 67]. Titania's performance in these applications has been shown to improve with a multi-scale porous morphology. Considering photocatalysis as one example more closely, a multi-scale porous morphology specifically consisting of open pores in the macro- and meso-scale has been reported to outperform materials with a monomodal pore size distribution.

1.3.2. Multi-Scale Titania for Photocatalysis

One of the most enticing applications of titania is its use as a photocatalyst for the degradation of organic pollutants in water. As a semiconductor material, titania exhibits a split electronic band structure with a valence band (VB) and conduction band (CB) separated by an energy band gap (E_g). This allows titania to be used in numerous photoelectric applications including photocatalysis by the excitation of electrons across the energy band gap (E_g) and utilization of charges generated (e^-/h^+ pair). The size of E_g and relative placement of the bands are crucial factors in determining the performance and suitable applications of semiconductor materials. The larger band gap of anatase (3.2eV) and the prime position of its bands relative to reduction-oxidation potentials make it the favored polymorph for photoelectric applications. However, this wide band gap limits the efficiency of titania as a solar light harvesting material, requiring photons in the ultraviolet range to excite electrons across the band gap. To overcome this challenge, the morphology and crystallinity of TiO_2 are often tuned to maximize its photocatalytic efficiency [68, 69].

Photocatalytic efficiency can be improved by tuning morphology to maximize surface area. The increase in surface area corresponds to an increase in potential reaction sites and enhances the probability of charge utilization. High surface area can be achieved by two methods: synthesis of nanoparticles and assembly of a controllable porous structure. First, nanoparticles exhibit a higher area-to-volume ratio, thus improving photocatalytic activity by two approaches. An increase in this ratio maximizes the number of available surface sites for reduction-oxidation reactions, while also reducing opportunity for charge recombination. The latter of these is achieved by reducing the distance the excited charges must travel, increasing the probability of

successful charge transport to the reaction sites at the surface where they can be exploited. Second, a porous body by definition will have more exposed surfaces than a dense material, thus preserves the effectiveness of the increased available surface introduced by the synthesis of nanoparticles. While meso- and micropores are the most significant contributors to surface area, literature has shown that a multi-scale porous structure may be more advantageous [70–72]. This improvement in photocatalytic activity from a multi-scale porous catalyst is accredited to the continued presence of meso-/micropores that maintain a relatively high surface area and complimentary effects of macropores, which improve light scattering and material flow through the catalyst. The scattering of incident light exposes more internal surfaces to irradiation, resulting in an increase in active sites and e^-/h^+ pair generation. Macropores also facilitate material flow through the titania photocatalyst as in the case of water/air purification, which promotes material adsorption onto active surfaces by exposing more material to reaction sites and rendering the photocatalyst more efficient [15, 22].

In terms of crystallinity, although anatase has been shown to be the superior polymorph due to its favored electric band structure, literature reports that a mixed-phase titania behaves more favorably and efficiently than pure anatase [73–77]. The improved photocatalytic activity of mixed-phase titania systems is attributed to the formation of a heterojunction. The interaction between the two phases with appropriate band placements can decrease e^-/h^+ pair recombination and increase the charge carrier lifetime. As schematically shown in Figure 1.12, this is achieved by the separation of the electron-hole pair across different crystals by the transport of an excited electron from one CB to an adjacent crystal with a lower CB, and/or of a generated hole in the VB to another VB at a higher relative electron energy potential. Therefore, crystallinity can also play a significant role when determining the performance of titania in certain applications.

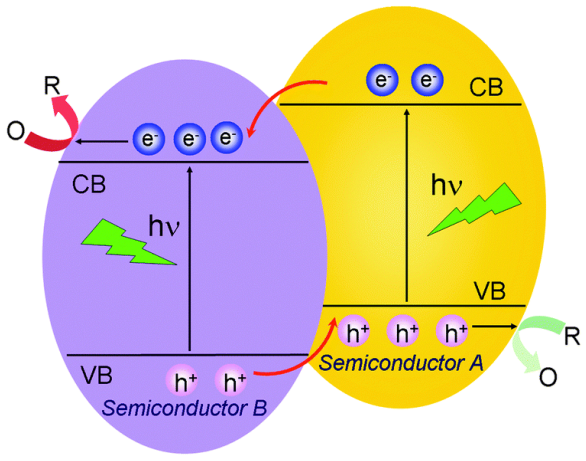

Figure 1.12: Schematic representation of the separation of generated electron/hole pairs in a heterojunction as has been reported to occur in biphasic titania [78]

1.3.3. Titania Polymorphs

Titania has numerous crystallographic polymorphs, most notable of which are anatase, brookite, and rutile, whose structures differ in the arrangement of TiO_6 octahedra. Rutile represents the thermodynamically stable phase exhibiting a tetragonal crystal structure, wherein each octahedron is coordinated to two edge-shared octahedra and eight corner-shared octahedra, and crystallizes at temperatures ranging 600-1000°C [73, 79–83]. However, the metastable tetragonal anatase phase, composed of an octahedron with four edge-shared and four corner-shared octahedra is known to outperform rutile in certain applications such as photocatalysis due to its more favorable electronic band structure [75, 81, 84, 85]. Unlike anatase and rutile, brookite expresses an orthogonal crystal structure with three edge-shared octahedra and its synthesis in a pure phase has proven very challenging, hindering sufficient characterization of its individual properties [73, 76].

Since rutile is thermodynamically stable at all temperatures and pressures, synthesis of the metastable phases (anatase and brookite) and transitions among the three phases are strongly dependent on reaction kinetics, crystal size, and particle packing [81]. For example, in the nanoparticle regime, anatase prevails as the stable phase due to its lower surface energy and to the sensitivity of rutile to surfaces and defects. In fact, while the bulk stability of the phases in decreasing order follows rutile, brookite, anatase, this sequence reverses when discussing nanoparticles [86]. Zhang and Banfield conducted thermodynamic and kinetic analyses and concluded that anatase is the most stable phase for particle sizes less than 11nm, brookite in the range of 11-35nm and rutile above 35nm [87]. Zhu et al. prepared titania samples of varying particle size and crystal composition and similarly calculated the free energies of the three common polymorphs and found the same order in stability [88]. However, they deduced that the critical particle sizes for the anatase-to-brookite and brookite-to-rutile transitions are 4.9nm and 30nm, respectively.

Aside from particle size, environmental conditions such as particle packing and solution chemistry can significantly affect phase stability. For example, Finnegan, Zhang, and Banfield show that solution pH can determine crystallinity [89]. The authors show that below the point of zero charge of titania, reported to lie between pH values of 5 and 7 [89–93], rutile nanoparticles

are more stable, whereas anatase becomes more stable in more basic conditions. Moreover, the wide range of crystallization temperatures reported for rutile is due to the sensitivity of its phase stability to surface energies. Rutile has been shown to nucleate at particle surfaces and interfaces such as at the neck of joined particles [87, 94, 95]. Zhang et al. specifically stated that rutile transformation preferentially occurs at interfaces at low sintering temperatures below 620°C, but that a surface nucleation mechanism dominates at higher temperatures [94]. Thus, particle packing can be a determining factor of phase stability and transformation mechanics, with a denser packing facilitating rutile nucleation at lower sintering temperatures. Since particle size, particle packing and reaction kinetics are significant factors in determining phase stability, it is crucial to choose the appropriate synthesis route to achieve the desired crystallographic and morphological characteristics.

1.3.4. Synthesis

Most literature approaches rely on pairing a synthesis route using a titania precursor with a suitable templating technique to generate titania nanoparticles directly assembled in a porous structure. While non-aqueous methods exist such as oxidation of titanium [96] and thermolysis of precursors [73, 97, 98], aqueous routes are more commonly employed for the controlled synthesis of porous nanosized titania. Synthesis involves the hydrolysis and condensation reaction of a ceramic precursor, commonly a titanium salt (e.g. $TiCl_4$) or titanium alkoxide in an aqueous solution according to the following equations,

Hydrolysis: $TiA_4 + 4H_2O \rightarrow Ti(OH)_4 + 4HA$ (Eq. 1.3)

Condensation $Ti(OH)_4 \rightarrow TiO_2 + 2H_2O$ (Eq. 1.4)

where A symbolizes the anion (Cl^- or alkoxide). The reaction of ceramic precursor with water in the hydrolysis stage (Eq. 1.3) creates $Ti(OH)_4$ nuclei which transform to TiO_2 via the condensation reaction (Eq. 1.4) by inorganic polymerization of the hydroxyl units into a network of TiO_6 octahedra. The formation of the network and resultant characteristics, such as crystallinity and particle size, size distribution and aggregation can be tailored by adjusting the synthesis route and parameters chosen. The aqueous-driven synthesis techniques usually fall within one of two categories: hydrothermal synthesis or sol-gel synthesis.

Hydrothermal synthesis is conducted in an autoclave reactor in the presence of water at high temperature (>100°C) and pressure to simultaneously form and crystallize titania nanoparticles. This technique grants fine control of synthesis conditions (temperature, pressure) while also allowing tuning of environmental chemistry with pH adjustments and use of additives. For example, Peng et al. hydrothermally treated $Ti(SO_4)_2$ with water and surfactant CTAB to synthesize mesoporous nanosized titania that exhibited high surface area even after calcination for improved crystallinity [34]. Li et al. prepared titania nanotube arrays by the combined hydrothermal and hard-templating techniques using ammonium hexafluorotitanate as ceramic precursor and an anodic aluminum oxide template [99]. The treatment was applied at 140°C for 60-180 mins and resulted in a continuous and porous titania surface. Figure 1.13 shows the tunability of the final morphology with varying hydrothermal treatment time. Rashad and Shalan also used hydrothermal treatment in the preparation of titania nanoparticles at 100°C for 24 hours [100]. They used TTIP as a precursor adjusted at a pH of 7 with ammonium hydroxide and found that the resultant morphology can be tuned by the addition of different surfactants. Control of particle size and polymorph nucleation and growth make the hydrothermal synthesis of titania an enticing method. However, this can require long hydrothermal reaction times and expensive equipment and sets limitations on the templating techniques that can be used to achieve multi-scale porous titania.

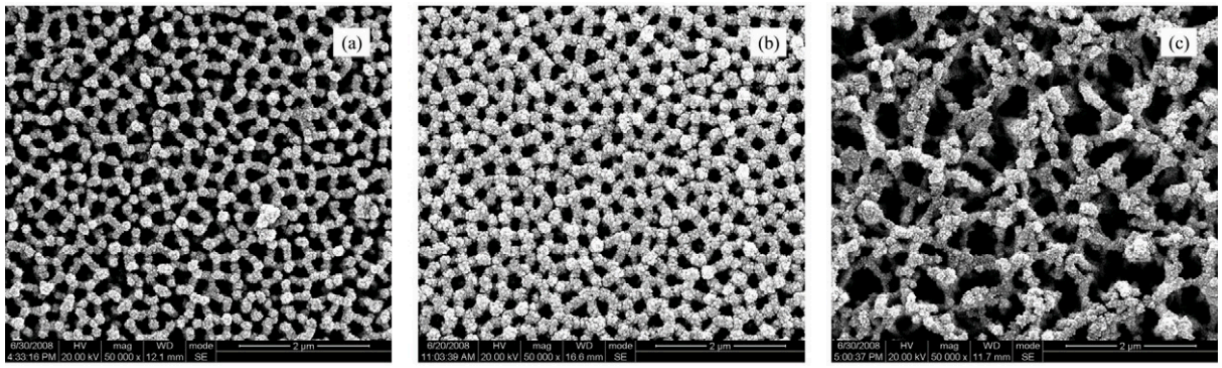

Figure 1.13: SEM images of titania nanotubes produced by Li et al. show the dependence of morphology on the hydrothermal treatment time after a) 60 mins, b) 90 mins, and c) 120 mins [99]

On the other hand, sol-gel synthesis is usually conducted in ambient conditions and permits the use of various strategies to fabricate multi-scale porous titania. The versatility of this technique allows the typically volatile reaction to be managed by manipulating synthesis

parameters including temperature, additives, solvent, and hydrolysis ratio (H_2O/TiA_4 molar ratio). Zheng et al. used [Emim]Br (1-ethyl-3- methyl-imidazolium bromide) as an additive to control the ratio of rutile to anatase in the hydrolysis of $TiCl_4$ in an aqueous HCl solution aged at 100°C for 24 hours [98]. They showed that higher additive concentration favored rutile nucleation in a rod-like morphology. They also found that lower HCl concentration resulted in higher rutile content and attributed this to the different arrangement of intermediary monomers during the condensation reaction, causing the variation in anatase-rutile composition. Shin et al. showed that the addition of nitric acid to the sol-gel hydrolysis of titanium tetraisopropoxide (TTIP) promoted dissolution of an amorphous phase and subsequently facilitated the transformation to the anatase phase before re-precipitating in the stable rutile phase over a period of 24 hours [101]. Khalil et al. looked at the effect of adding acetic acid to the hydrolysis of TTIP and found that its presence hindered the progression of the hydrolysis reaction, as evidenced by the increase in carbon content in dried samples, revealing that the sample still contained unreacted TTIP [102]. The authors also concluded that the addition of acetic acid affected the polymerization rate of hydrolysis products and caused morphological changes in the final sintered samples which exhibited smaller specific surface area values than samples prepared in the absence of acetic acid.

Several groups also have investigated the effect of a variety of other synthesis parameters, such as alcohol solvent on managing the typically volatile hydrolysis of titania precursors. Vorkapic and Matsoukas systematically identified hydrolysis and peptization temperature and amount and molecular weight of alcohol solvent as significant factors in determining the stability and aggregation of titania primary particles at a high hydrolysis ratio (H_2O/Ti molar ratio = 220) [103]. According to this work, smaller particle sizes (measured by dynamic light scattering and TEM) were achieved at hydrolysis temperatures at and above room temperature, peptization at 50°C, and in the absence of any alcohol. The authors claimed that parameters that deviate from these optimal settings tend to encourage aggregation of primary particles. Song and Pratsinis studied the effects of amount and choice of organic alcohol on porosity and phase composition of titania in the hydrolysis of TTIP at a constant H_2O/TTIP molar ratio of 20 [104]. They discovered that the addition of solvent retarded the hydrolysis reaction of TTIP such that the dried powders

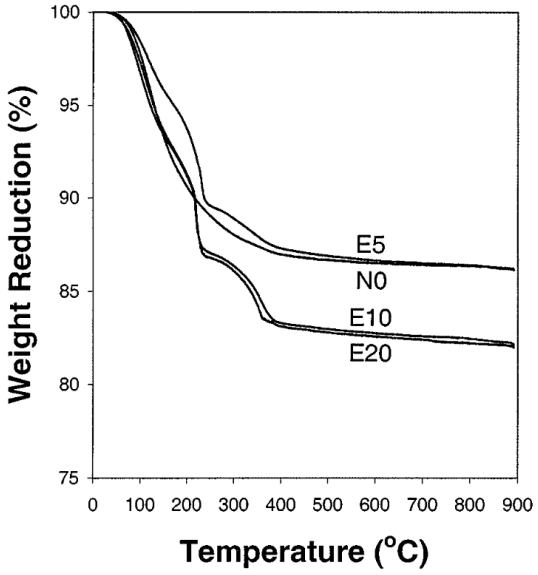

Figure 1.14: Samples prepared at ethanol/TTIP molar ratio values of 0, 5, 10, and 20 exhibited higher residual organic content when TTIP was hydrolyzed in the presence of ethanol [104]

exhibited amorphous behavior, whereas the powders prepared in the absence of solvent displayed anatase peaks in XRD. The impeded hydrolysis rate in the presence of alcohol solvent was further evidenced by thermogravimetric analysis (TGA) shown in Figure 1.14, which revealed higher residual organic content found in these materials after drying. Furthermore, the authors concluded from nitrogen adsorption-desorption analysis that the bimodal porosity found in all samples was partially dependent on the alcohol. They observed a decrease in average intraparticle pore size with increasing methanol and ethanol content, while a constant value was seen with varying amounts of isopropanol and sec-butanol. Therefore, while the addition of alcohol solvent helped manage the typically volatile hydrolysis rate of TTIP, Song and Pratsinis showed that the choice of organic alcohol solvent can affect the morphology and porosity observed in the final ceramic [104]. Khalil et al. also studied the effect of organic solvent choice (isopropanol and n-heptane) on the hydrolysis of TTIP and found that the choice of solvent affected the aggregation rate and resultant morphology [102]. While aprotic n-heptane allowed fast aggregation and formation of open bulk structures, the protic isopropanol hindered aggregation resulting in more compact bulk structures with smaller specific surface areas. Thus, the nature and amount of alcohol added to the sol-gel reaction of a titania precursor can significantly affect the hydrolysis rate and morphology of the final titania samples.

Water content (often reported as H_2O/Ti molar ratio) has also been shown to affect the final titania product. The work found in literature studying the correlation between water content and morphology and crystallinity of titania can be classified according to the range of H_2O/Ti molar ratio values investigated as low (below a value of 20) [80, 102, 105–107] and high (above 100) [70, 106–109]. Ding, Qi, and He investigated the effect of water content at low hydrolysis ratio values ranging from 1 to 4 on the sol-gel reaction of titanium butoxide (TBOT) in

the presence of ethanol and HCl and found that phase transformation temperature and crystallite size slightly differed even within the small range of H_2O/Ti molar ratio values tested [80]. For example, XRD conducted on samples annealed at different temperatures revealed small differences at 823 K, with the sample prepared at a ratio of 1 exhibiting fractional rutile formation along with anatase, while the sample prepared at a H_2O/Ti ratio of 4 only showed anatase behavior with the rutile peak not appearing until after heat treatment at 873 K. Furthermore, average crystallite size calculated using the Scherrer equation was found to also depend on hydrolysis ratio. At all annealing temperatures tested, the lower hydrolysis ratio corresponded to lower crystallite size values. Khalil et al. also studied the effect of water content on the formation of titania in the hydrolysis of TTIP using n-heptane or isopropanol as solvent [102]. The authors concluded that the change of H_2O/Ti ratio from 1 to 8 does not cause many changes in the presence of n-heptane, but when isopropanol was used as a solvent, an increase in water content resulted in a decrease in aggregation rate and increase in bulk compactness and particle size.

Song and Pratsinis [107] and Hanaor et al. [106] independently studied the effect of H_2O/Ti ratio at low and high values on the hydrolysis of TTIP in the presence of an organic solvent. Song and Pratsinis [107] used ethanol as solvent and considered ratio values of 5, 20, 200, and 1000, whereas Hanaor et al. [106] investigated H_2O/Ti ratio values of 6 and 100 in the hydrolysis of TTIP in the presence of isopropanol. Both groups concluded that samples prepared at low ratio values did not undergo full hydrolysis and exhibited amorphous behavior until after calcining at 300-400°C, whereas the samples prepared at the high ratio values experienced complete hydrolysis of the precursor and consequently showed anatase peaks in XRD analysis after drying before sintering. These changes rippled through to changes in rutile transformation temperature, average crystallite size, and surface area at various sintering temperatures. Both sets of authors demonstrated that samples prepared at low H_2O/Ti ratio values, exhibited larger specific surface area values among dried samples, but that they were overtaken by the samples prepared at high ratio values after sintering. This trend is attributed to the different phase behavior of samples. Before sintering, the smaller particles of the amorphous samples prepared at low H_2O/Ti ratio values provided more surface than already crystalline titania particles of samples prepared at high ratio values. However, calcination of the amorphous samples triggered rapid nucleation and

growth of crystalline domains, resulting in larger particles and subsequently smaller surface areas.

Grzeskowiak et al. hydrolyzed TTIP in the presence of isopropanol at high H_2O/TTIP ratios ranging 85-400 and concluded that crystalline content in dried samples increased with increasing water content [109]. They also found that the pore size distribution peak shifted to slightly larger pores and exhibited a higher mesopore volume with increasing hydrolysis ratio after calcination at 500°C, which resulted in larger surface area values. Aside from phase behavior and mesoporosity measured by N_2 adsorption, hydrolysis of titanium alkoxides at high H_2O/Ti molar ratio values has been shown to affect the macro-scale morphology of final titania samples, particularly in the absence of a retarding agent, such as an organic solvent. Collins et al. reported the spontaneous formation of aligned macrochannels in the hydrolysis of various titanium alkoxides in an aqueous ammonia solution at a high H_2O/Ti molar ratio (approximately 150) [108]. Figure 1.15 shows the presence of these channels in the sample prepared by hydrolysis of titanium tetra-butoxide. Yu, Su, and Cheng similarly fabricated hierarchical titania by this template-free approach by hydrolyzing TBOT at H_2O/Ti molar ratios exceeding 190 in the absence of any additives [70]. Both sets of authors attributed the spontaneous self-assembly to the accelerated hydrolysis rate and formation of microphase-separated regions of titania nanoparticles and water channels caused by the high H_2O/Ti ratio values used. Thus, amount of water used in the hydrolysis of titanium precursors via the sol-gel method provides an effective tool for managing degree of hydrolysis completion, phase behavior, and morphology simultaneously on the meso- and macroscales. However, more studies are needed to investigate the effects of water content in a more moderate range of H_2O/Ti ratio between 20-100.

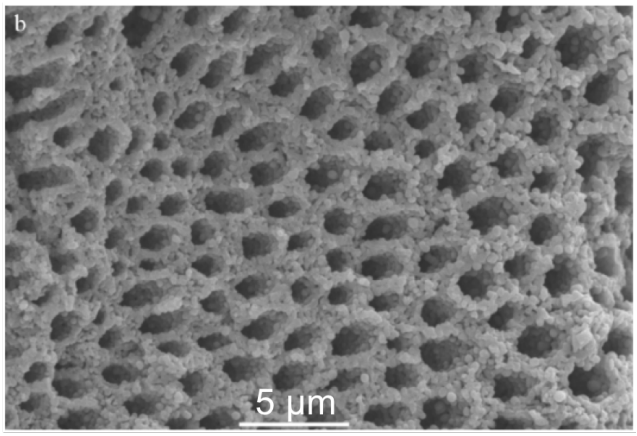

Figure 1.15: Image of macrochannels first reported by Collins et al. in the hydrolysis of TBOT at high H_2O/Ti molar ratio values [108]

Literature has shown that synthesis parameters such as organic solvent addition and hydrolysis ratio (H_2O/Ti molar ratio) play crucial roles in determining the hydrolysis rate, phase evolution, porosity and morphology. Groups have used various synthesis methods spanning various titania precursors and wide ranges of water amounts and organic solvent additions, making it nearly impossible to identify the effect of individual synthesis parameters on the final titania. Furthermore, while some groups have shown the ability to synthesize multi-scale porous titania by sol-gel reaction of titanium alkoxides at high H_2O/Ti ratio values, there still remains two main scientific questions. First, what roles do individual synthesis parameters such as water content at moderate H_2O/Ti ratio values play in creating multi-scale titania exhibiting aligned macrochannels similar to those observed in literature? Second, can the meso-structure of these multi-scale porous titania be tailored by some technique such as hard-templating in a combined templating strategy without disrupting the formation of the macrochannels?

1.4. Cellulose Nanocrystals

Cellulose is the most abundant, naturally occurring, renewable biomaterial in the world and can be sourced from plants, tunicates, and certain bacteria and algae. Its superior chemical and physical properties provide plant cell walls with structure support and strength. Furthermore, its nanometric size and inert nature make this biomaterial a very promising hard-

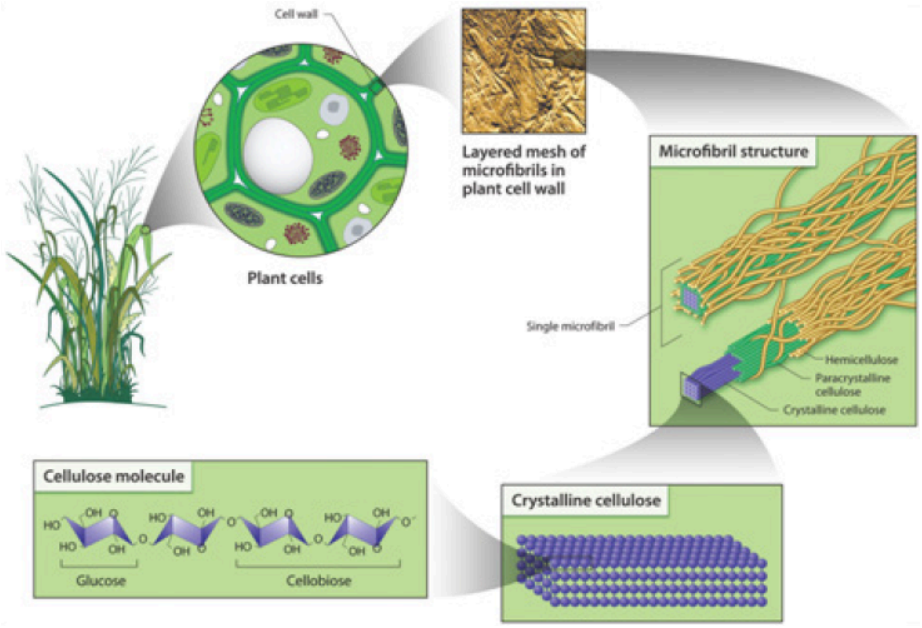

Figure 1.16: Schematic representation of the source of cellulose from plants and its chemical structure [110]

template in the production of porous materials. Extraction of the crystalline regions known as cellulose nanocrystals (CNCs) can be successfully achieved by acid hydrolysis, in which the source material composed of cellulose, hemicellulose and lignin (see schematic in Figure 1.16) is subjected to strong acids (e.g. H_2SO_4, HCl). The acids preferentially attack the less crystalline regions of the material and leave behind crystalline nanocellulose whiskers at the core of the microfibers, which are more resistant to attack. The acid is then diluted and separated along with the impurities from the CNCs by centrifugation and dialysis. The dimensions of CNCs vary from one source to the next and depend on the extraction parameters used (significant factors of acid hydrolysis are temperature, agitation, and time) and can range 5-50 nm in width and 100 nm-5 µm in length [111]. CNCs used in this research were extracted from wood pulp and exhibit dimensions in the lower range with widths of 5-20 nm and lengths of 100-200 nm (Figure 1.17).

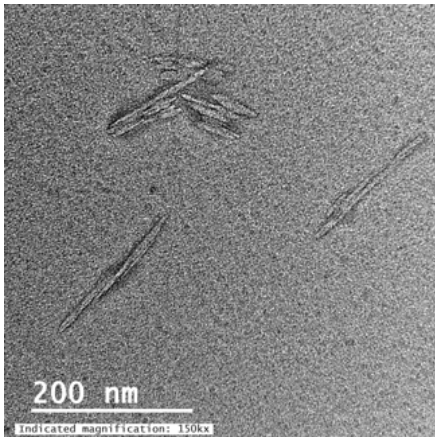

Figure 1.17: TEM image provided by Ms. Kelly Stinson-Bagby of never-dried wood pulp CNCs stained with NanoVan

As a high molecular weight homopolymer, cellulose is chemically composed of glucose ($C_6H_{12}O_6$) with a repeat segment consisting of a dimer exhibiting a 180° corkscrew. Each glucose unit takes on a chair conformation and contains three hydroxyl groups, which play a crucial role in determining the properties of CNCs including its hydrophilic nature and tendency to agglomerate. The abundant surface hydroxyl groups equip CNCs with the ability to form interparticle hydrogen bonds [112]. Thus, aqueous suspensions of CNCs can exhibit a variety of phases ranging from well-dispersed colloidal suspensions to gels. The colloidal stability and determination of phase of an aqueous suspension are based on DLVO theory and depend on the balance between van der Waals attractive forces and electrostatic repulsive forces. Since repulsive forces can be tailored in order to stabilize colloidal suspensions, several groups have investigated the effects of colloidal concentration, surface charges (measured by ζ-potential) and ionic strength on the stability of aqueous CNC suspensions [113–119]. For example, increasing the ionic strength of solution by addition of salts (e.g. NaCl) tends to decrease the critical aggregation concentration (which signifies the onset of aggregation) by shielding surface charges,

effectively reducing repulsive forces, and permitting CNC-CNC interactions and agglomeration, rendering the suspension unstable [113–115]. It has also been shown that increasing the CNC concentration causes the suspensions to shift in nature from a near-Newtonian viscous fluid (at < 3wt%) characteristic of a stable colloidal suspension, through one exhibiting some shear thinning behavior attributed to weak interactions (at ~3-7wt%), to a gel with properties characteristic of a viscoelastic solid (at > 7wt%) [115–117]. The tendency of surface hydroxyl groups to form hydrogen bonds and cause CNCs to agglomerate makes it a challenge to prepare stable colloidal aqueous suspensions. Although these hydroxyl groups are the source of this difficulty, they also can serve as the solution as they are readily modifiable.

Chemical modifications are often employed to replace the surface hydroxyl groups with alternative end groups to deter attraction among cellulose strands by inducing electrostatic charge repulsion. Extraction of CNCs by acid hydrolysis with sulfuric acid (H_2SO_4) results in partial replacement of hydroxyl end groups with sulfate half ester (OSO_3) groups on exposed surfaces. These negatively charged surfaces induce electrostatic repulsive forces and discourage agglomeration by CNC-CNC hydrogen bonding. Thus, CNCs extracted by this method (i.e. as opposed to using HCl) exhibit improved dispersibility and more readily form stable colloidal suspensions in water and other polar solvents. Furthermore, the repulsive forces caused by the introduction of these negative sulfate half ester surface charges can lead the CNCs to self-assemble into a liquid crystal [111, 117, 120, 121]. Above a critical concentration, the polymer whiskers arrange into an anisotropic chiral nematic structure in which the CNCs co-align in parallel planes and experience a degree of misorientation from one plane to the next (Figure 1.18). The helical pitch, defined as the length along the rotation axis at which CNCs rotate a full 360°, is a function of the electrostatic forces and can be tailored by changing the concentration of CNCs and ionic strength of the suspension by addition of salt and adjustment of pH [122].

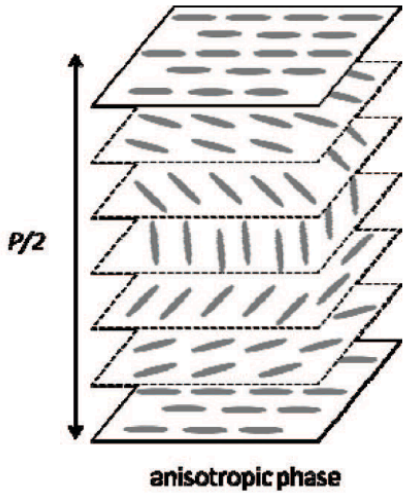

Figure 1.18: Schematic of anisotropic chiral nematic phase of CNCs with helical pitch, p (reprinted with permission from ref. [111]; copyright 2010 American Chemistry Society)

There are also methods to chemically modify surface hydroxyl groups with alternative end groups to further enhance dispersibility and provide CNCs with functionalities desirable in particular applications. For example, (2,2,6,6-Tetramethylpiperidine-1-oxyl)-oxidized (TEMPO-oxidized) CNCs have shown improved dispersion and aversion to flocculation and sedimentation in water. These CNCs are chemically modified such that the exposed primary hydroxyl groups (hydroxymethyl groups) on the surface are converted to carboxyl groups, producing a negatively charged surface. Habibi, Chanzy and Vignon functionalized HCl-hydrolyzed tunicate CNCs by TEMPO-oxidation [119]. They found that this modification permitted the preparation of homogeneously dispersed cellulose whiskers in water without altering the dimensions of the original cellulose. The authors also claimed that the carboxyl groups are more stable than sulfate half esters which tend to detach in basic (pH > 7) conditions. Cellulose can also be chemically modified with positive charges. For example, Hasani et al. used epoxy-propyltrimethylammonium chloride to functionalize H_2SO_4-hydrolyzed CNCs to create cationic hydroxypropyl-trimethylammonium chloride end groups [118]. The charge reversal was confirmed by ζ-potential measurements which switched from -39mV to +30mV after functionalization, suggesting that these cationic CNCs were electrostatically stabilized in aqueous suspension. Cellulose can also be surface modified with non-ionic surfactants to improve dispersion in non-polar solvents. Ljungberg et al. coated the surface of tunicate cellulose with a phosphoric ester of polyoxyethylene(9) nonylphenyl ether surfactant, which enabled successful, stable dispersion in toluene [123]. These modified cellulose whiskers were also incorporated as well-dispersed fillers in an atactic polypropylene matrix and provided reinforcement for the polymer matrix as determined by mechanical testing. Thus, modification of end group chemistry allows CNCs to be used in a wide range of environments and permits the use of their desirable physical properties in a wide range of applications.

The desirable mechanical properties, high aspect ratio, dispersibility, and ability to functionalize the surface chemistry have encouraged the use of CNCs and other cellulose derivatives in a variety of applications. For example, several groups have shown the reinforcing capabilities of CNCs as a filler agent in numerous polymer composites [123–129]. CNCs have also been used to stabilize dispersions and emulsions [130–134] and their biocompatibility allows

their implementation as drug carriers [135–138]. Additionally, the nanometric dimensions, high degree of crystallinity, modifiable end-group chemistry, physical stability, and water-insolubility make CNCs prime hard-templating agents for preparation of porous ceramic materials in colloidal processing routes.

1.4.2. Cellulose-Templated Titania

Several groups have investigated the use of cellulosic materials in templating several mesoporous ceramics [121, 139–142]. When specifically considering cellulose-templated titania, methods can be classified into one of three categories. The first method consists of anchoring previously synthesized ceramic particles onto cellulose fiber surfaces. Kale et al. coated cotton fabric with a mixture of cellulose and titania nanoparticles suspended in an aqueous solution of sulfuric acid [143]. Subsequent washing, neutralization and drying resulted in homogeneous coating of the cotton fabric by a cellulose-TiO_2 thin film. The interaction was established by the formation of interchain linkage between fabric and suspended celluloses in the presence of sulfuric acid solution. Boriboon et al. dissolved cellulose acetate in an aqueous acetic acid solution and added ground titania particles [144]. This mixture was electrospun and the dry mixture was immersed in a solution of KOH in ethanol before being rinsed and dried. The cellulose-titania composite exhibited uniform dispersion of titania particles on the cellulose fiber surfaces with close to 80% porosity and enhanced performance as a cathode/anode separator for Li-ion batteries. While these composites exhibit unique morphologies, the titania-cellulose interactions are limited by the use of already prepared titania particles.

The mixture of cellulose and a ceramic precursor followed by controlled, in-situ nucleation and growth of titania particles around the template grants an additional technique for improving cellulose-TiO_2 interaction and more faithfully replicating the bio-template to tune morphology of the cellulose-ceramic composites [72, 145–150].

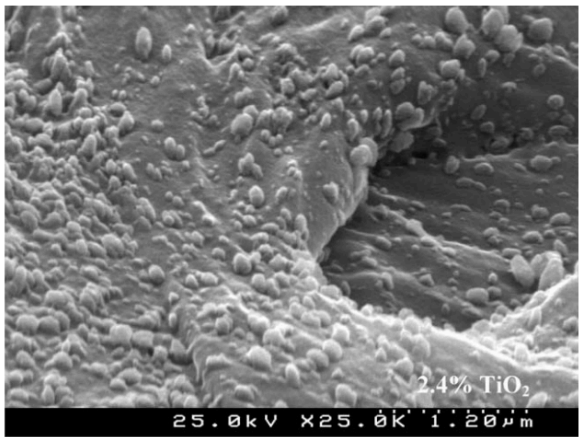

Figure 1.19: SEM image of a cellulose-titania composite prepared by in-situ synthesis from a precursor solution in the presence of the cellulose template show successful adsorption of titania particles [145]

This is shown by Marques, Trindade, and Neto who hydrolyzed $TiOSO_4$ in the presence of aqueous sulfuric acid solution, to which cellulose fibers were added [145]. Figure 1.19 shows an SEM image of a sample prepared by this method and the improved adsorption of titania on the cellulose material. The authors identified aging time and reaction temperature as significant factors for tuning the composite morphology and degree of titania retention on cellulosic fibers. In comparison to a blend of cellulose and commercially available titania, handsheets of these composites exhibited an increase in opacity and greater decrease in tensile strength with increasing TiO_2 content. This change in properties pointed to improved interactions and more uniform distribution of particles in the synthetic titania-cellulose composite than the blend using commercial titania. Liu et al. extracted cellulose nanocrystals at different acid hydrolysis times and suspended the biopolymer in a HNO_3-ethanol solution [146]. Titanium ethoxide was slowly added to this mixture before being diluted with water and freeze-dried to produce composite nanomaterials with tunable content of coated TiO_2, surface area, and morphology. Coating of TiO_2 was achieved by adsorption of precursor molecules on cellulose surfaces and reaction with surface hydroxyl groups, forming water molecules and resulting in strong adsorption of the ceramic molecules. These cellulose-TiO_2 composites demonstrate the feasibility of incorporating cellulose materials in the synthesis of TiO_2 from a precursor solution to successfully alter the final ceramic morphology.

Further porosity and morphological control can be achieved by a third technique which consists of integrating cellulose materials in the synthesis of titania from a precursor and subsequently removing the template by thermal decomposition or chemical extraction [121, 151–157]. Mohamed et al. synthesized C-doped mesoporous titania whose morphology and doping granted it superior photocatalytic efficiency in comparison to commercially available Degussa P25 [151]. This was achieved by adding a solution of TBOT and isopropanol dropwise into water containing regenerated cellulose, adding nitric acid, aging in tight air, and heat treating at 75°C in vacuum. The simultaneous acidic degradation of regenerated cellulose and crystallization of ceramic coating allowed the cellulose to serve as the morphological template and source of carbon dopant. The authors demonstrated the faithful replication of the cellulose structure with formation of titania nanorods that exhibited photocatalytic activity enhanced by

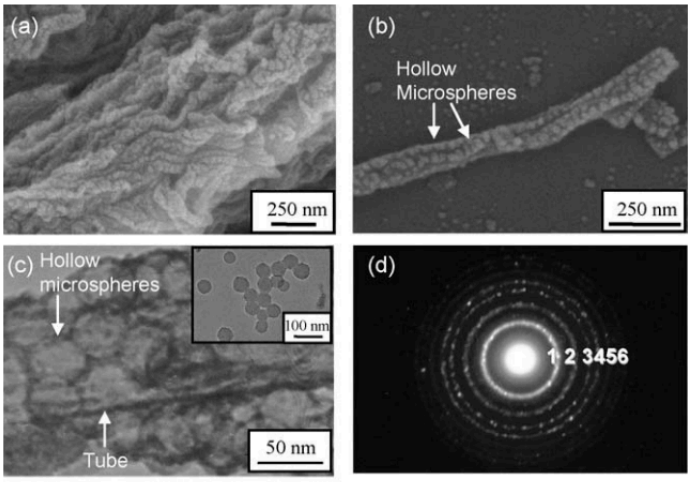

Figure 1.20: SEM images show (a) the successful cellulose-templating and (b) the titania nanotube/hollow sphere hybrid; (c) TEM shows the titania nanotube coated by hollow titania microspheres all consisting of anatase titania according to (d) electron diffraction patterns [153]

the C-doping and change in morphology observed. Shopsowitz et al. successfully replicated the chiral nematic order of CNCs in a silica system by the controlled hydrolysis of TMOS and used the resultant porous silica as an intermediate hard-template to synthesize titania exhibiting a chiral nematic porous structure [121, 152]. The authors' systematic study revealed that a contraction of chiral nematic pitch is observed after calcination of CNCs and identified acid hydrolysis as an alternative method for removing the bio-template without compromising the morphological structure. Gu et al. used a dual-templating technique to create titania nanotubes coated with titania hollow microspheres [153]. Cellulose filter paper, serving as the first hard-template was coated with titania precursor and hydrolyzed by reaction to water to form nanotubes. Prior to calcination, sacrificial microspheres (of silica or PS latex) were deposited and again the sample was coated with titania precursor and hydrolyzed. Subsequent calcination and template removal resulted in a titania nanotube/hollow sphere hybrid as seen in Figure 1.20.

The successful templating of titania by cellulose materials is contingent on the interaction between the template and the ceramic or ceramic precursor. Marques, Trindade and Neto determined from their work that adsorption of TiO_2 particles onto cellulose fibers is unlikely to be by physical interaction due to the retention of high contents of coated TiO_2 after "extensive mechanical agitation" applied during synthesis procedures [145]. Several groups report observations of similarly durable TiO_2-CNC interaction even after rigorous disruption to the mixture in suspension, eliminating weak van der Waals forces as a candidate cause of adsorption. Therefore, interaction must be either electrostatic or chemical. Figure 1.21 schematically represents these two possibilities. Martakov et al. more closely investigated the establishment

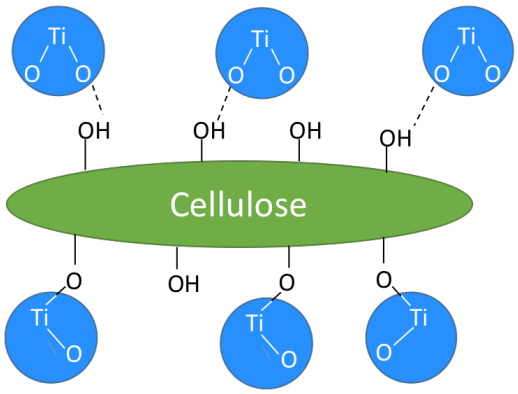

Figure 1.21: Schematic representation of the (top) electrostatic interaction by hydrogen bonding and (bottom) chemical interaction by formation of Ti-O-C bonds between cellulose and titania particles

of cellulose-titania interactions and cited electrostatic attraction of positively charged TiO_2 surfaces and CNC negative surfaces as the cause of adsorption [147]. According to the authors, this led to the formation of hydrogen bonds between Ti-O^- groups and cellulose surface hydroxyl groups, as determined by Fourier-transform infrared (FTIR) spectroscopy, which continued until either charge neutralization was achieved or all TiO_2 particles adsorbed onto CNC surfaces. Mohamed et al. similarly used FTIR to support their claim of hydrogen bonding between cellulose surface hydroxyl groups and TiO_2 particles by looking at the shift of the O-H stretching absorption peak from a high (3336 cm^{-1}) to low (3274 cm^{-1}) wavenumber [151, 158]. The same authors also mention the formation of Ti-O-C bonds as a result of Ti-OH and C-OH interactions. Liu et al. suggested this as the adhesion mechanism between titania nanoparticles and the cellulose template [146]. According to this mechanism, ceramic precursor molecules (e.g. $Ti(OH)_4$) adsorb and react with the surface hydroxyl groups on the cellulose to form Ti-O-C bonds and generate H_2O molecules in a quasi-condensation reaction and leads to “the tight anchoring” of titania on the cellulose surface.

The incorporation of cellulose into the synthesis of titania provides the potential for strong interactions between template and ceramic. These interactions serve as the foundation for using cellulose to successfully template porous titania materials as reported by literature, particularly after template burn-out. However, more work is needed to determine the feasibility of using CNCs as a hard-template simultaneously with other methods in a combined templating technique for fabricating multi-scale porous ceramics.

1.5. Statement of Work

The goal of the following work is to show the feasibility of tuning the mesoporous structure of multi-scale porous titania by the addition of CNCs as sacrificial material in a combined template-free self-assembly and hard-templating technique. In order to accomplish this, a systematic study was necessary to investigate the effect of three variables in the hydrolysis of titania tetra-isopropoxide (TTIP) by the sol-gel method, namely water content, isopropyl alcohol (IPA) solvent content, and drying method, on the morphology and phase behavior of the final ceramic. Water content, defined as H_2O/TTIP molar ratio was explored within a new moderate range (between 15-100) in this work and the results of this study were aligned to identify the optimal synthesis settings for the template-free self-assembly of multi-scale porous titania. This was followed by the introduction of CNCs into the synthesis procedures using the parameters chosen to study their effectiveness in templating the titania meso-structure within the multi-scale porous morphology. Electron microscopy, nitrogen adsorption-desorption, and diffraction were conducted to characterize the morphology and crystallinity of prepared samples. Analysis of these data was performed to determine the optimal synthesis parameters to produce multi-scale porous titania and the feasibility of using CNCs as a hard-template to tailor the meso-scale morphology in these multi-scale porous ceramic structures.

Chapter 2. Fast, Facile Three-Ingredient Recipe for Multi-Scale Porous Titania

2.1. Overview of Work

Titania samples exhibiting a multi-scale pore size distribution were prepared by a facile, rapid technique via hydrolysis of titanium tetra-isopropoxide (TTIP) using varying H_2O/TTIP ratio values within a new moderate range, different drying methods, and with/without the use of isopropanol as solvent. The effect of these parameters on the pore size distribution, particle size, morphology, and crystallinity were systematically studied. Electron microscopy revealed the synthesis of 5-15 nm nanoparticles assembled into multi-scale structures with macrochannels of 1-3 μm in diameter and 20-30 μm length as well as interparticle and inter-agglomerate pores ranging from one to a few hundred nanometers in size. Hydrolysis in excess H_2O increased the frequency of the macrochannels and increased particle packing in the struts, while the introduction of isopropanol dramatically decreased their presence and rendered more homogeneous microstructures. Titania nanoparticles obtained after sintering at 450°C exhibited primarily anatase phase with a secondary phase dependent on synthesis parameters. This simple and fast approach contrasted dramatically with previous, much more complex and ingredient-heavy recipes and enabled the synthesis of titania nanoparticles with high crystallinity, assembled in a multi-scale porous pattern with just three reactants (one of them, water) in less than 12h, without the need for surfactants, dispersants, or pH adjustments.

2.2. Introduction

Much attention has been directed at titanium dioxide (titania, TiO_2) in the past few decades for its application across a multitude of fields [8, 10, 58–64, 66]. The use of titania in photocatalysis, sensing, and biomedicine is reliant on its porous structure and although titania is one of the most suitable candidates for many of these applications, there is still a need to optimize its structure and functionality. For example, photocatalytic efficiency and activity of TiO_2 can be dramatically improved by altering morphology [68, 69]. It has been shown that assembly of a multi-scale porous structure with pores on the meso- and micro-scale to contribute to an

increase in surface area and macropores to improve efficiency by scattering incident light onto more surfaces and generating more electron-hole pairs out-performs mono-scale porosity [15].

As a versatile and facile technique, the hydrolysis of titania precursors by the sol-gel method has been a popular approach to preparing porous titania. This synthesis strategy is often used by researchers due to its adaptability and the ability to apply various templating techniques, such as hard-templating to control porosity. Various templates ranging from ceramic [44] to polymer [43] materials have been used via the sol-gel method to successfully tune titania morphology. In particular, cellulose nanomaterials have shown great potential in shaping meso-structured ceramics [135, 146, 147, 152–155, 159–161]. However, before these templating techniques can be employed to tailor the meso-scale morphology, as discussed in Chapter 3, it is necessary to determine the impact that certain synthesis factors have on forming multi-scale porous titania.

Previous work using the sol-gel method has been performed using a wide variation of synthesis parameters, making it very difficult to identify the roles of each parameter in determining final morphology. Furthermore, investigations of effect of water content in the hydrolysis of titanium alkoxides has been exclusive to low (below a value of 20) [80, 102, 105–107] or high (above 100) [70, 106–109] H_2O/Ti molar ratio values. While some literature reports the self-assembly of multi-scale porous titania at extremely high H_2O/Ti molar ratio values [70, 108], no report was found studying more moderate ratio values or the role of other synthesis parameters such as alcohol solvent and drying method on the preparation of these multi-scale porous titania morphologies. To this end, titania samples exhibiting a multi-scale pore size distribution were prepared by a facile, rapid technique via hydrolysis of titanium tetra-isopropoxide (TTIP) using varying H_2O/TTIP ratio values within a new moderate range, different drying methods, and with/without the use of isopropanol as solvent.

In this study, a facile three-ingredient synthesis technique is identified to develop crystalline titania nanoparticles assembled into a multi-scale porous structure with high surface area. The work presented investigates the effect of water content, the addition of alcohol solvent, and drying method on crystallinity, morphology, and specific surface area of the titania particles and multi-scale porous structures derived from those conditions. The data reveals that multi-scale porous titania can be synthesized at much lower water/precursor molar ratio values than had

been previously reported, more simply and quickly (in less than 12 hours), without the need for dispersants, surfactants or pH changes. The results from this study are aligned to identify the optimal synthesis settings for achieving highly porous, self-assembled titania whose structures can be further tailored using cellulose nanocrystals in a combined template-free self-assembly and hard-templating technique.

2.3. Experimental

2.3.1. Synthesis

Titanium tetra-isopropoxide (TTIP) (Sigma-Aldrich, 97%) and isopropanol (IPA) (Spectrum Chemical HP692 HPLC) were used as the titania precursor and organic solvent, respectively, as received, in the following hydrolysis reaction (Eq. 2.1 and 2.2) by addition of deionized water:

Hydrolysis: $Ti(OCH[CH_3]_2)_4 + 4H_2O \rightarrow Ti(OH)_4 + 4HOCH[CH_3]_2$ (Eq. 2.1)

Condensation: $Ti(OH)_4 \rightarrow TiO_2 + 2H_2O$ (Eq. 2.2)

Figure 2.1 shows the experimental procedure used in this work. Appropriate volumes of TTIP and IPA were magnetically stirred for approximately 5 minutes at 275 rpm. Water was then added to this solution by micropipette, resulting in the instant formation of a white precipitate. This suspension was mixed with a stirring rod until all visible signs of reaction (bubbling, precipitation, color change, off-gassing, exothermic heat) ceased. The white suspension was further mixed in an ice bath with a pulse sonicator (Fisherbrand Model 705 Sonic Dismembrator, USA) at an output of 40% for 2 minutes with a pulse rate of 1 second on, 1 second off, to ensure sufficient dispersion of the produced precipitate in the solvent. The mixture is manually stirred after sonication before being poured into cylindrical steel molds (22 mm internal diameter and 25 mm height) to dry.

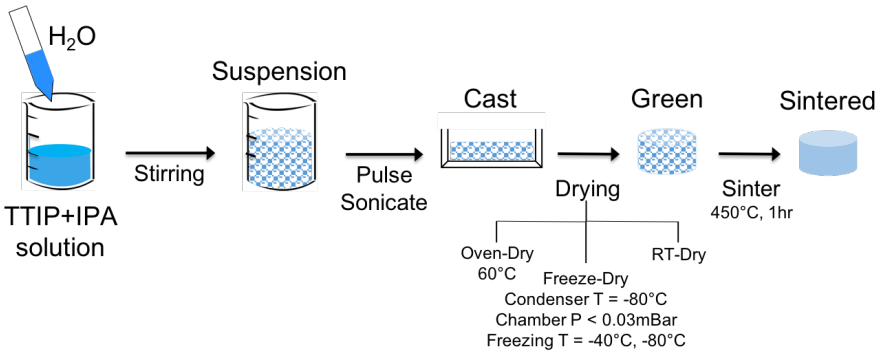

Figure 2.1: Schematic of the facile synthesis of multi-scale porous titania by the sol-gel method

Synthesized samples were dried in three different ways: 1) at room temperature, 2) in an oven at 60°C, or 3) freeze-dried. In the first two methods, the samples dried within 12 hours (marked by the loss of approximately 90% of excess solvent measured by weight). In the case of freeze-drying, samples were frozen at -40°C or -80°C, then freeze-dried for 36 hours with a Labconco FreeZone 2.5L Freeze Dry System (USA), whose condenser coil was held below -80°C while pressure in the chamber remained below 0.03 mBar. Green samples were partially sintered in a box furnace (Deltech Furnaces Front Load DT-31-FL-6, USA) in air at 450°C for 1 hour with a heating rate of 2°C min^{-1} and cooling rate of 5°C min^{-1} in order to initiate necking between particles without compromising the porosity introduced during synthesis.

Table 2.1 summarizes the synthesis conditions used for this study. To study the effect of water content, samples were prepared with H_2O/TTIP molar ratios of 5, 15, 30, and 60 in the absence of IPA; it is proposed that the excess H_2O would serve as solvent. To study the effect of IPA addition, samples were synthesized at a constant H_2O/TTIP molar ratio of 15 at TTIP-IPA concentrations of 0.1M, 0.4M, 0.75M, 1.0M, and 1.5M (calculated as moles of TTIP divided by total volume of TTIP and IPA in liters). Three drying methods were utilized to investigate the effect on the produced microstructure; for this portion of the study, samples were hydrolyzed at a constant H_2O/TTIP ratio of 15 in the absence of IPA. As a naming convention, a single letter is added to the sample name listed to signify whether the sample is green (“G”) or sintered (“S”).

Table 2.1: Synthesis and Processing Conditions

Sample Name	H_2O/TTIP molar ratio	TTIP-IPA concentration	Drying Method
5-0M OD	5	0M	Oven-Dried (60°C)
15-0M OD	15	0M	Oven-Dried (60°C)
30-0M OD	30	0M	Oven-Dried (60°C)
60-0M OD	60	0M	Oven-Dried (60°C)
15-0.1M OD	15	0.1M	Oven-Dried (60°C)
15-0.4M OD	15	0.4M	Oven-Dried (60°C)
15-0.75M OD	15	0.75M	Oven-Dried (60°C)
15-1.0M OD	15	1.0M	Oven-Dried (60°C)
15-1.5M OD	15	1.5M	Oven-Dried (60°C)
15-0M FD(-40)	15	0M	Freeze-Dried (frozen at -40°C)
15-0M FD(-80)	15	0M	Freeze-Dried (frozen at -80°C)
15-0M RT	15	0M	Room Temperature Dried

2.3.2. Characterization

Crystallinity of synthesized samples was analyzed before and after sintering by powder x-ray diffraction (XRD) with a PANalytical X'Pert Powder PRO diffractometer (Netherlands) with a Bragg-Brentano configuration and Cu-Kα radiation with a 1.54 nm wavelength. Standard x-ray diffraction powder patterns [162, 163] were used to identify the titania polymorphs that form.

Morphology was observed with a LEO Zeiss 1550 field-emission scanning electron microscope (FESEM). Samples were coated with 15 nm of iridium using a Leica EM ACE600 (Germany) and imaged at an accelerating voltage of 5 keV. A JEOL S/TEM 2100 transmission electron microscope (TEM) (Japan) at an accelerating voltage of 200 keV was used to measure particle size and confirm crystallinity determined by XRD using selected area electron diffraction.

Nitrogen adsorption was conducted on a Quantachrome NOVA-e Series system (USA) on all green and sintered samples. Samples were de-gassed at 100°C overnight and analyzed at relative pressures ranging 0.01-0.99 with a 41-point spread. Specific surface area (SSA) was calculated by the multi-point Brunauer-Emmett-Teller (BET) method at the relative pressure range of 0.05-0.3. The Barrett-Joyner-Halenda (BJH) method was used to calculate pore volume at the maximum relative pressure and to construct pore size distribution curves by analysis of the desorption branch.

2.4. Results and Discussion

2.4.1. Effect of Water Content in Synthesis

Figure 2.2 shows SEM images of green samples hydrolyzed (in the absence of IPA) at H_2O/TTIP molar ratios of (a, b) 5, (c, d) 15, (e, f) 30, and (g, h) 60. The presence of porous channels is observed as the H_2O/TTIP molar ratio used during hydrolysis increases (left column, Figure 2.2a, c, e, g). These channels form parallel to each other and perpendicular to the surface with diameters on the order of 1-3 µm and lengths of 20-30 µm. The periodicity and presence of the channels seem to increase with increasing H_2O/TTIP molar ratio and are preserved after sintering at 450°C (images not shown). High magnification images (right column, Figure 2.2b, d, f, h) show the formation of titania nanoparticles of 10-15 nm for all conditions, with particle packing in the walls of the porous structures that tends to increase with increasing H_2O/TTIP molar ratio. These images also show smaller interconnected macropores on the order of a few hundred nanometers

and interparticle meso/micropores less than 50 nm in size. Thus, the samples show a multi-scale porous structure that is maintained after sintering and is in agreement with the findings of Yu et al. [70] and Collins et al. [108] However, it is important to highlight that the structures have been

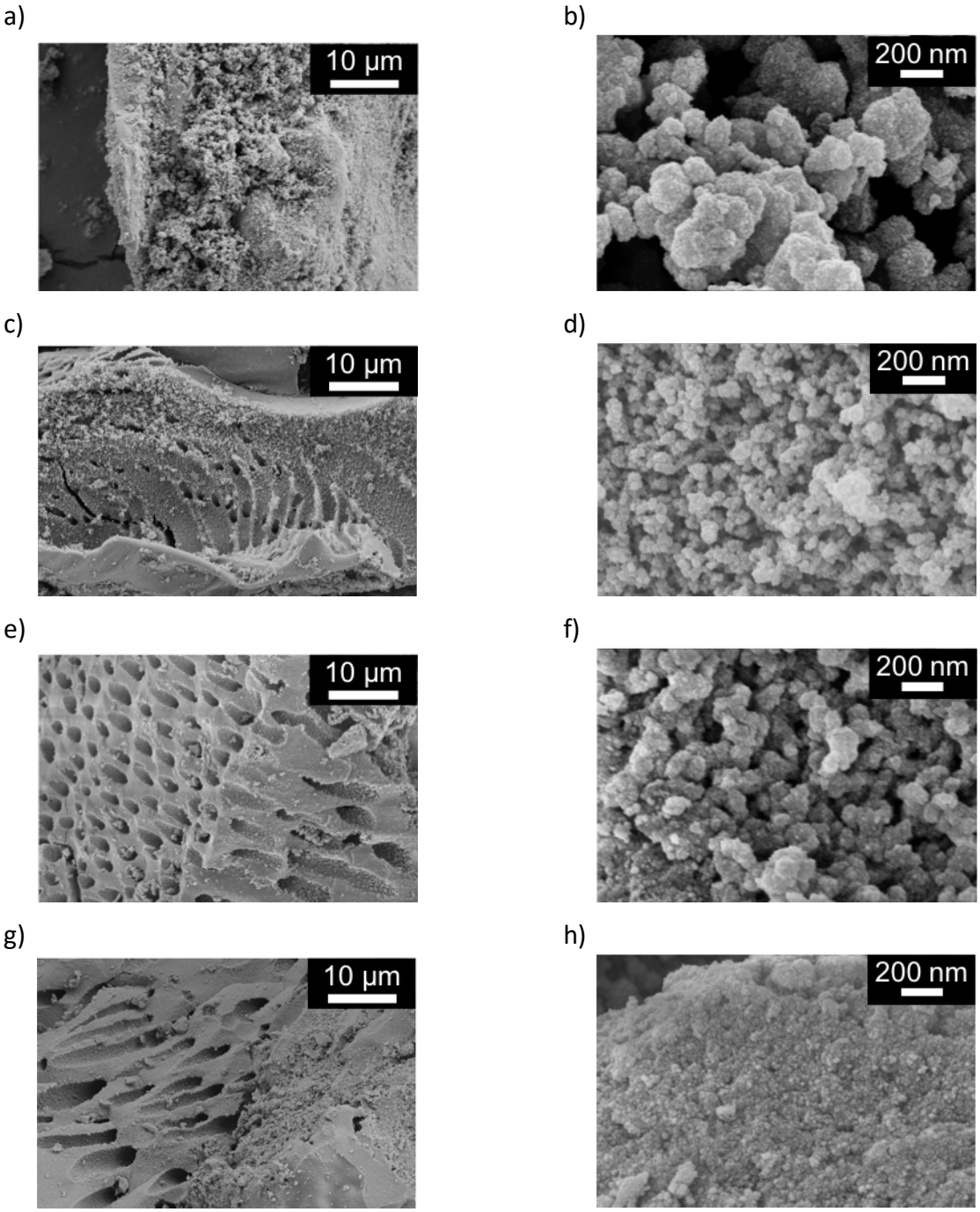

Figure 2.2: SEM images of green samples hydrolyzed in the absence of IPA at H_2O/TTIP molar ratio values of (a, b) 5, (c, d) 15, (e, f) 30, and (g, h) 60

achieved in this work at much more moderate H_2O/TTIP molar ratio values less than a third of those reported by those groups (H_2O/TTIP > 150).

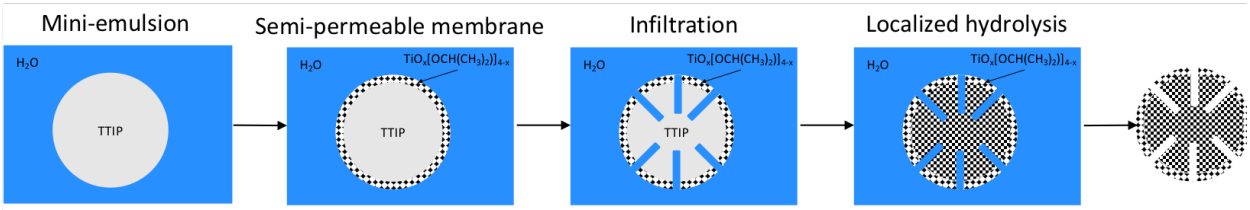

Figure 2.3: Schematic of the macrochannel formation mechanism of TTIP in excess water in the absence of IPA

The formation mechanism of macrochannels from the hydrolysis of Ti-alkoxides in a water-rich environment has been described by Collins et al. [108] and supported by Yu et al. [70] and is schematically represented in Figure 2.3. TTIP and H_2O are immiscible liquids and form a mini-emulsion when mixed. At the interface of the mini-emulsion droplets, the hydrolysis reaction initiates, producing a thin titania layer. This semi-permeable membrane allows reagents to mix as water enters the droplet in radial directions and localizes further hydrolysis within. These channels of water expose previously encapsulated TTIP molecules, which hydrolyze to form nanoparticles. Water diffuses throughout the emulsion by bifurcation as well as capillary pressure caused by already formed nanoparticles. Adding excess water to the solution ensures complete hydrolysis of free and encapsulated TTIP to form titania and minimizes the amount of retained organic groups as reported by Hanaor et al. [106]. The removal of water by drying leaves behind the macrochannels that can be observed by SEM in Figure 2.2. Collins et al. [108] and Yu et al. [70] claim that stirring the suspension of white precipitate destroyed the formed macrochannels. While adding the reagents dropwise and extracting the precipitate by filtration may better preserve channels in greater periodicity, the results of this study demonstrate that stirring and sonicating the suspension lead to the dispersion and re-grouping of these mini-emulsion droplets. The final result is still macroporous titania powders with a multi-scale porous network that has been shown to occur at water molar ratio values as low as 15 and 30 rather than the previously reported values above 150.

Figure 2.4 depicts TEM images with insets of selected area diffraction pattern (SADP) for green samples corresponding to H_2O/TTIP ratios of 15 (Figure 2.4a) and 60 (Figure 2.4b). It can be seen that nanoparticles of approximately 10 nm in diameter can be obtained via this method.

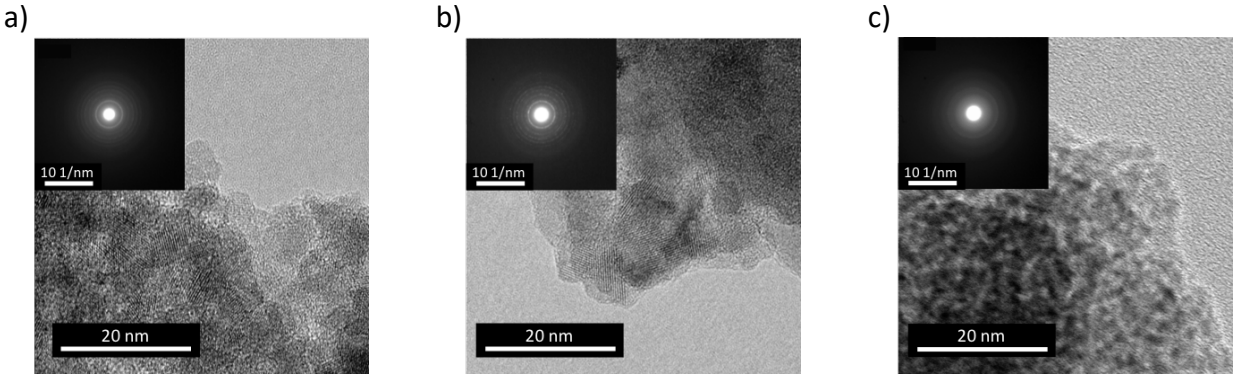

Figure 2.4: TEM images of a) G15-0M OD, b) G60-0M OD, and c) G15-0.4M OD show the increase in crystallinity at higher H_2O/TTIP molar ratio values and absence of IPA

SADP electron diffraction exhibits rings with diameters typical of the anatase titania phase in green samples indicating the arrangement of atoms in long-range order before sintering. Hanaor et al. [106] and Song and Pratsinis [107] reported similar findings at much higher H_2O/TTIP molar ratio values exceeding 100. Moreover, comparative investigation in this work of values within the moderate range reveals a more interesting trend. These diffraction patterns point to an increase in degree of crystallinity of the titania nanoparticles in green samples hydrolyzed at higher H_2O/TTIP molar ratios.

Figure 2.5 shows the XRD patterns of green (Figure 2.5a) and sintered (Figure 2.5b) samples as a function of H_2O/TTIP molar ratio. For green samples, a phase evolution from amorphous to more crystalline phases can be observed with increasing H_2O/TTIP ratio. This trend is in good agreement with the results of Hanaor et al., who determined that crystallization in green samples occurs at a H_2O/TTIP ratio between 6 and 100 [106]. Investigation of moderate H_2O/Ti molar ratio values in this work reveals that crystallization in the green state (Figure 2.5a) is induced at a molar ratio of 15, where the primary anatase peak at 25.3° is initially observed and becomes dominant at a ratio of 30. At this point, peaks corresponding to the brookite phase also appear indicating the synthesis of an anatase-brookite mixture from hydrolysis in excess water. The sample produced in a water-limited environment at a ratio of 5 exhibited more amorphous behavior in the green state. After sintering, this sample crystallized into an anatase-rutile mixture while samples prepared at higher H_2O/TTIP molar ratios preserved their anatase-brookite mixture. This discrepancy may be elucidated by considering stability of the three titania crystal phases. In discussing the factors that affect crystallization and nucleation of titania polymorphs, Kumar and

Rao cited reaction kinetics and particle size as significant factors in determining phase stability [81]. Even though rutile is thermodynamically stable in bulk, theoretical analysis conducted by Zhang and Banfield demonstrated that anatase and brookite are more stable in the nanometer regime [87]. This may explain the crystallization of anatase and brookite in green samples as products of accelerated reaction kinetics in excess water. This phase behavior is preserved after sintering at 450°C due to insufficient energy to induce transformation into the thermodynamically stable rutile phase [81]. On the other hand, sintering of amorphous G5-0M OD primarily nucleates anatase due to its stability in the nanometric size regime and forms rutile as a secondary phase due to its thermodynamic stability and preferred nucleation at the elevated temperature.

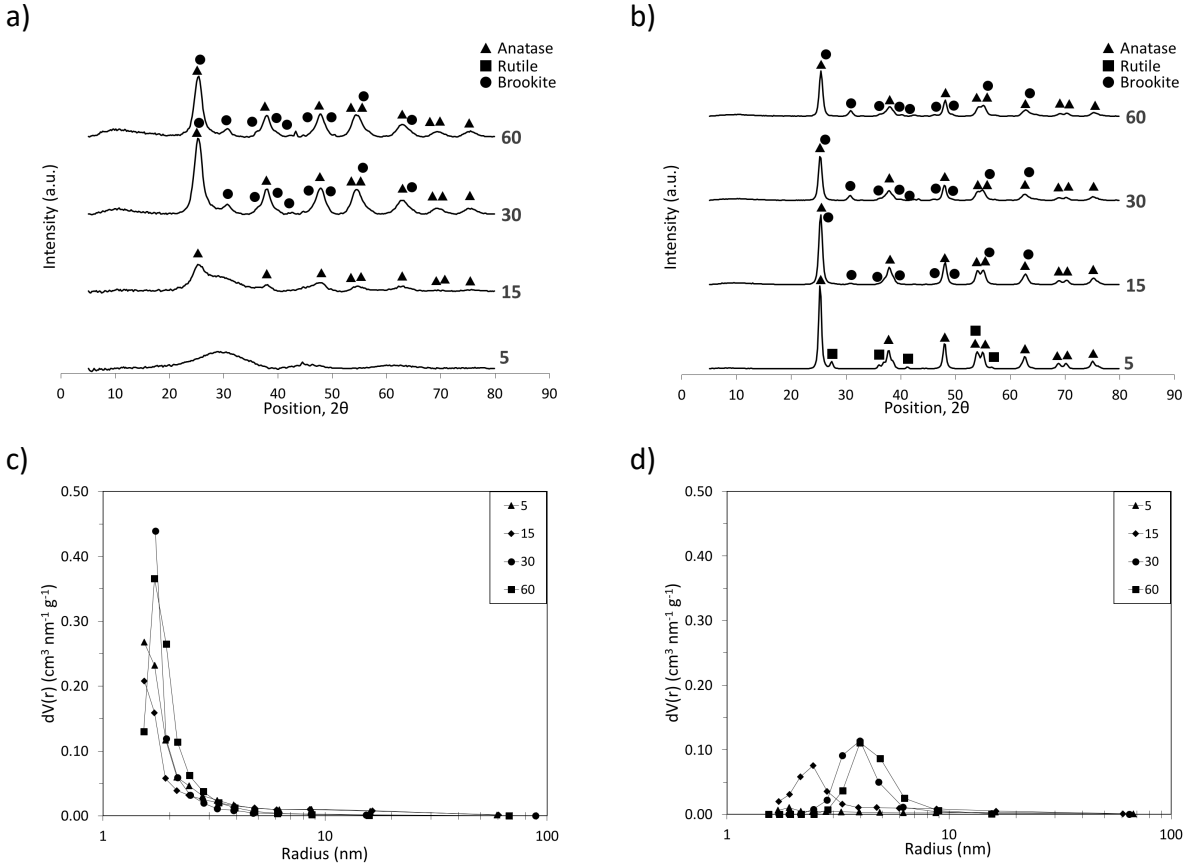

Figure 2.5: XRD patterns of a) green and b) sintered samples and BJH pore size distributions of c) green and d) sintered samples show the dependence of crystallinity and porosity, respectively, on the H_2O/TTIP molar ratio

The surface area of the green samples prepared with increasing H_2O/TTIP ratio ranges from 720 to 290 m^2 g^{-1}, as shown in Table 2.2. These values are in good agreement with other work reported in the literature using similar precursors and synthesis routes [106, 107]. The pore size

distribution of all green samples (Figure 2.5c) shows that a microporous structure exists, corresponding to the interparticle spacing between the nanoparticles of titania. When the H_2O/TTIP ratio increases, there is a closer particle packing within the walls of the macrochannels, as seen in Figure 2.2, resulting in lower overall microporosity and therefore in lower values of surface area. The porosity corresponding to the macrochannels is not seen in the pore size distribution, since their size exceeds the measurement range of the nitrogen adsorption technique. Table 2.2 and Figure 2.5d show the expected decrease in surface area and pore volume as a consequence of the sintering and necking between particles. There is a peak shift towards the mesopore range in the pore size distribution after sintering, resulting in a significant decrease in SSA to a range of 20-80 $m^2\ g^{-1}$. This slight increase of the pore size is due to the necking process and pore rearrangement over this process. While the three samples hydrolyzed in excess water (H_2O/TTIP ratios of 15, 30, and 60) had comparable sintered surface areas around 70-80 $m^2\ g^{-1}$, the sample prepared at a H_2O/TTIP ratio of 5 exhibited a significant decrease from 720 $m^2\ g^{-1}$ to 20 $m^2\ g^{-1}$ upon sintering. This is attributed to the incomplete hydrolysis of TTIP at such low water content [106], resulting in smaller amorphous titania particles more loosely arranged in the green body. Upon sintering, this sample undergoes crystallization into anatase and necking between particles, resulting in the collapse of the more open, less packed structure in the green samples that can be seen in Figure 2.2e.

Table 2.2: Surface Area and Pore Volume of Green and Sintered Samples Under the Different Synthesis Conditions

Sample	BET Surface Area [$m^2\ g^{-1}$]		Pore Volume [$cm^3\ g^{-1}$]	
	Green	Sintered	Green	Sintered
5-0M OD	720	20	0.660	0.110
15-0M OD	510	70	0.540	0.250
30-0M OD	310	80	0.290	0.220
60-0M OD	290	70	0.290	0.240
15-0.1M OD	280	40	0.340	0.220
15-0.4M OD	690	50	0.780	0.220
15-0.75M OD	770	40	1.020	0.220
15-1.0M OD	890	40	1.030	0.330
15-1.5M OD	690	50	0.860	0.250
15-0M FD(-40)	620	60	0.600	0.220
15-0M FD(-80)	440	30	0.410	0.180
15-0M RT	500	60	0.420	0.210

Synthesis of TiO_2 by the hydrolysis of TTIP in excess water in the absence of an alcohol solvent has been shown to produce multi-scale porous ceramic bodies exhibiting aligned macrochannels and inter-agglomerate and interparticle macro- and mesoporosity. Excess water acts as the solvent and drives the reaction to completion resulting in titania nanoparticles with long-range crystalline order before any sintering is applied. Although, these channels are first observed at a H_2O/TTIP molar ratio of 15, SEM images reveal that a molar value of 30 produces more periodic and defined macrochannels.

2.4.2. Effect of the Addition of Isopropanol (IPA) in Synthesis

The addition of IPA in the hydrolysis of TTIP significantly affects the morphology and crystallinity of the synthesized titania powders. Figure 2.6 shows micrographs of green samples hydrolyzed with varying molarities of TTIP-IPA solution, with a lower molarity indicating higher IPA content. Hydrolysis in the presence of IPA produces samples that lack macrochannels or other defined macroporous structure. Instead, these samples exhibit more open, random macroporosity. The particle packing of the titania nanoparticles is more uniform in these samples than in those prepared in the absence of IPA. These samples still exhibit a multi-scale porous network: the open random macroporosity of the green bodies and the microporosity between the titania nanoparticles, as evidenced by high magnification micrographs (right column of Figure 2.6). The addition of IPA into the solution prevents the formation of the mini-emulsions that initiate the macrochannel formation mechanism by acting as a co-solvent for TTIP and H_2O. The addition and subsequent dispersion of water to the already prepared, well-mixed TTIP-IPA solution gives way to the homogeneous nucleation of nanoparticles from liquid interface reactions. IPA prevents the separation of TTIP droplets and formation of a semi-permeable membrane, but rather allows reactions to occur more homogeneously. Random packing of particles occurs during drying, resulting in the more even dispersion of nanoparticles shown in Figure 2.6. The size of the titania nanoparticles synthesized seems to be slightly smaller (below 10 nm) with the addition of IPA, as can be seen in Figure 2.6 and Figure 2.4c. Furthermore, the inset of Figure 2.4c shows a representative electron diffraction pattern of these samples and reveals that hydrolysis in the presence of IPA hinders the establishment of long-range crystalline order, resulting in a halo pattern typical of amorphous nanoparticles.

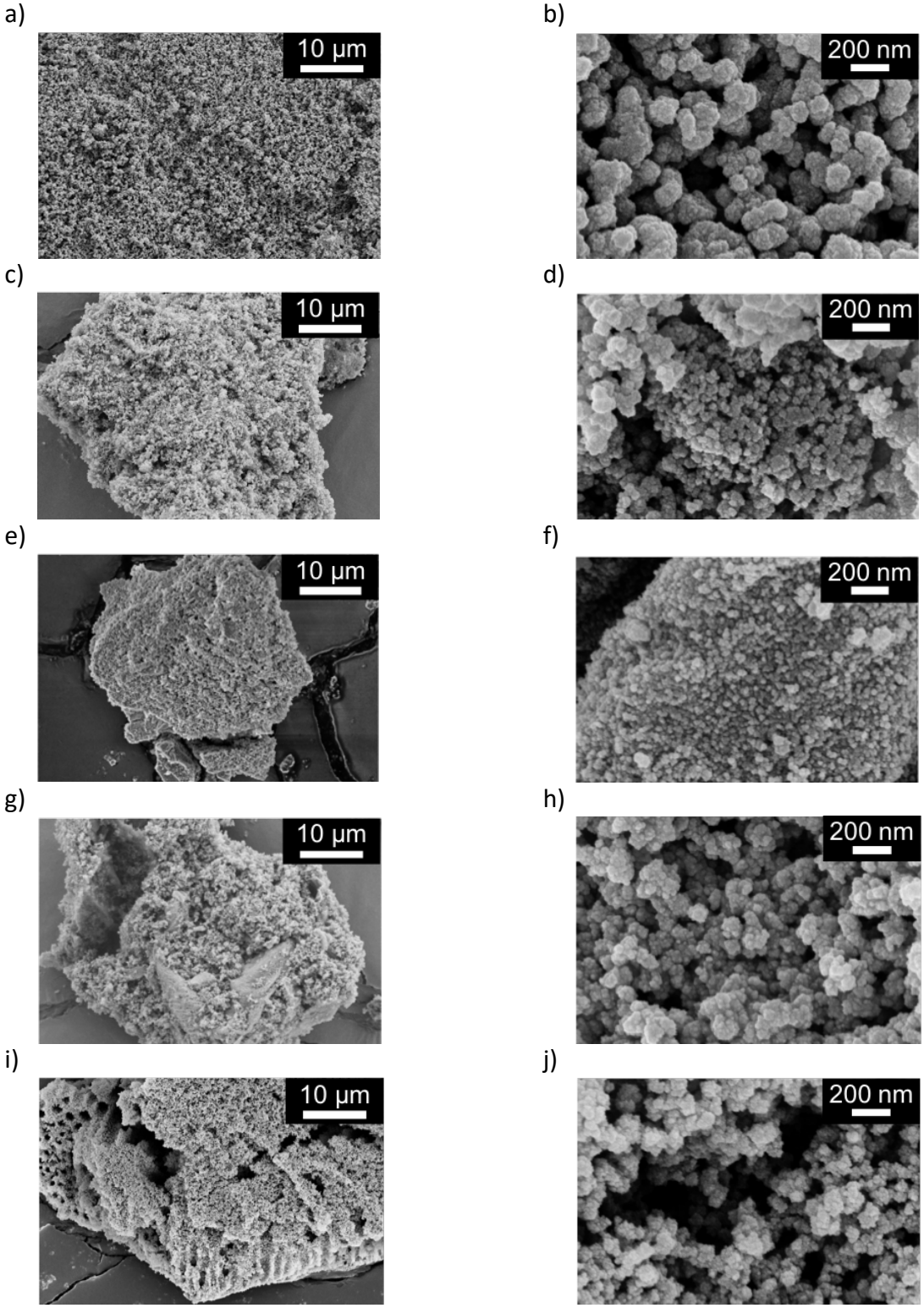

Figure 2.6: SEM images of green samples synthesized in the presence of IPA at a constant H_2O/TTIP ratio of 15 and TTIP-IPA concentrations of (a, b) 0.1M, (c, d) 0.4M, (e, f) 0.75M, (g, h) 1.0M, and (i, j) 1.5M

XRD patterns of the green samples, of which two representative examples are shown in Figure 2.7a, confirm the amorphous nature of the nanoparticles with broad peaks appearing for all green samples hydrolyzed in the presence of IPA. This change in phase behavior can be attributed to the role of IPA in lowering the kinetics of the hydrolysis reaction [102, 104, 106]. By slowing down the reaction kinetics, the samples could only undergo partial hydrolysis, lacking the driving force to form any long-range crystalline order and resulting in the appearance of broad peaks typical of amorphous particles. Song and Pratsinis report similar effects of hydrolyzing in the presence of an alcohol solvent [104]. After sintering, all samples hydrolyzed with IPA formed crystalline anatase-rutile mixtures. This is a similar result to S5-0M OD, where an amorphous green sample (G5-0M OD) resulted in rutile appearing as the secondary crystal phase after sintering. This is due to rutile being the stable phase, making it the preferable polymorph to crystallize from an amorphous sample after sintering.

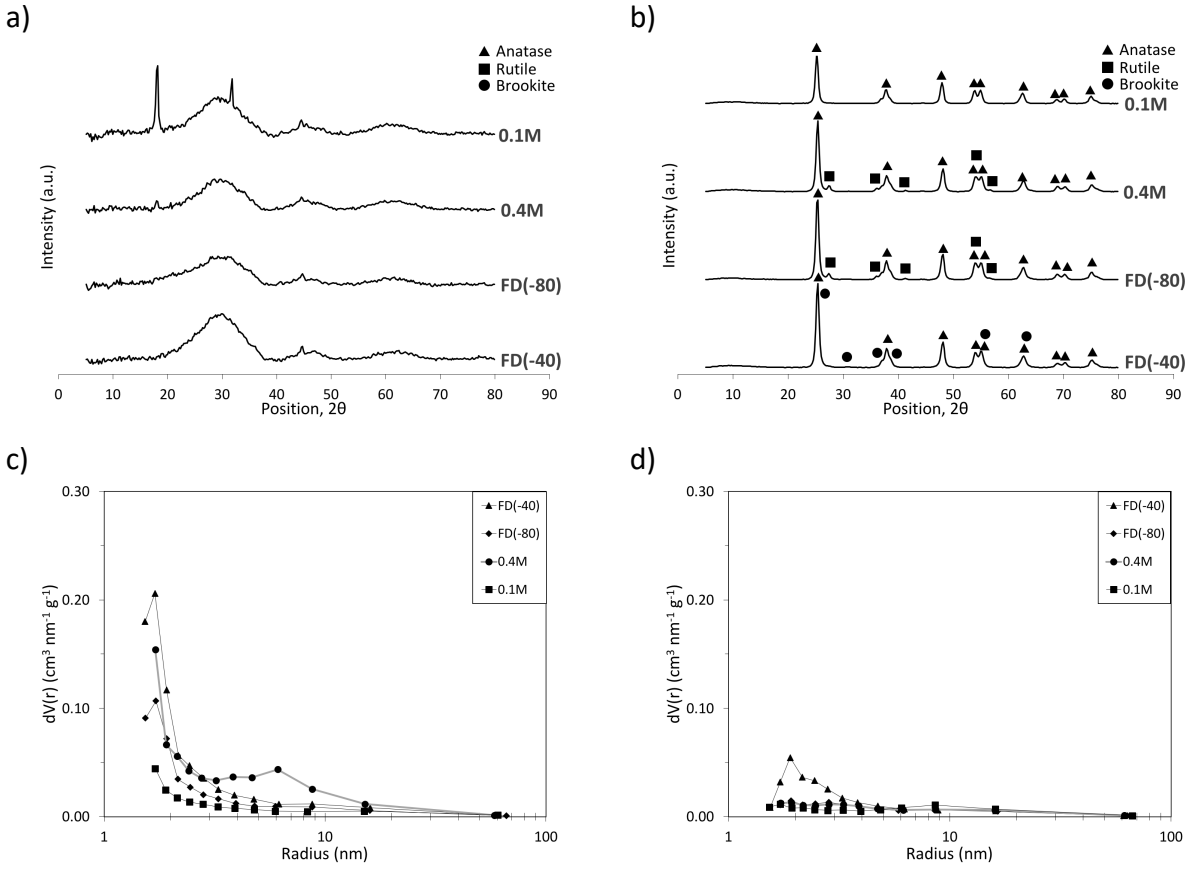

Figure 2.7: XRD patterns of a) green and b) sintered samples and BJH pore size distributions of c) green and d) sintered samples show the dependence of crystallinity and porosity, respectively, on the TTIP-IPA concentration and drying method

The absence of defined macrochannels in the presence of IPA allows the nanoparticles to keep a more random, loose and uniform packing across the green bodies. Therefore, there is a significant increase of pore volume due to the interparticle porosity (Figure 2.7c). The more significant contribution to surface area of pores in this range, in conjunction with the smaller amorphous nanoparticles found in TEM images (Figure 2.4c) leads to an increase in calculated surface area as observed for green samples, reaching a maximum of 890 m^2 g^{-1} (Table 2.2). However, these values experience a significant drop after sintering. All samples synthesized with IPA produced sintered surface area values ranging 40-50 m^2 g^{-1}, which are slightly lower than the surface area of samples hydrolyzed without IPA. This is due to a greater reduction in porosity during particle necking over sintering. The decrease in surface area can be attributed to the densification of particles as well as crystallization and grain growth from the amorphous green samples. Furthermore, since rutile is more stable at larger crystallite sizes [87, 88], its nucleation during sintering may result in lower surface-to-volume ratio values and consequently lower surface area than the anatase-brookite mixtures formed in the absence of IPA.

Adding IPA as solvent to the hydrolysis of TTIP has been shown to adversely affect the macrochannel morphology observed in its absence. Samples prepared in the presence of IPA still exhibit a multi-scale porous structure. However, this morphology consists of a homogeneous spread of macro- and mesopores of random orientation and size rather than aligned macrochannels. Thus, it is concluded that IPA acts as a co-solvent for TTIP and H_2O, retarding the hydrolysis reaction and hindering the macrochannel formation mechanism. This results in homogeneous morphology exhibiting smaller nanoparticles lacking any long-range crystalline order in the green samples. Sintering nucleates anatase-rutile titania and causes significant decrease in surface area.

2.4.3. Effect of Drying Method in Synthesis

Figure 2.8 shows SEM images of green samples synthesized at a constant H_2O/TTIP ratio of 15 with no IPA addition, and dried using various methods. Samples prepared with different drying methods all exhibit macrochannel morphology, confirming the strong dependence of the macrochannel formation mechanism on the H_2O/TTIP ratio and absence of IPA as co-solvent. However, the features of the macrochannels observed in these samples vary with drying method.

As can be seen, freeze-dried samples (Figure 2.8c, e) exhibit a more defined architecture of the macrochannels than oven-dried (Figure 2.2c) and room temperature dried (Figure 2.8a) samples prepared at similar synthesis parameters, with widths of 1-3 µm, lengths of 25-40 µm and inter-channel spacing of 1-5 µm. G15-0M FD(-80) shows fewer macrochannels overall, possibly due to faster freezing of the suspension before complete formation of titania happened. This sample also shows traces of a lamellar architecture typically observed in ice-templating of aqueous mixtures [53]. Investigation of these variously dried samples at higher magnification also reveals an improvement in particle dispersion with increasing rate of solvent removal (i.e. RT < OD < FD(-40) < FD(-80)). Drying at room temperature and at 60°C allowed nanoparticles to continue moving in suspension as the solvent was slowly removed and caused them to agglomerate. On the other hand, freeze-drying has been shown to deter particle agglomeration and better preserve

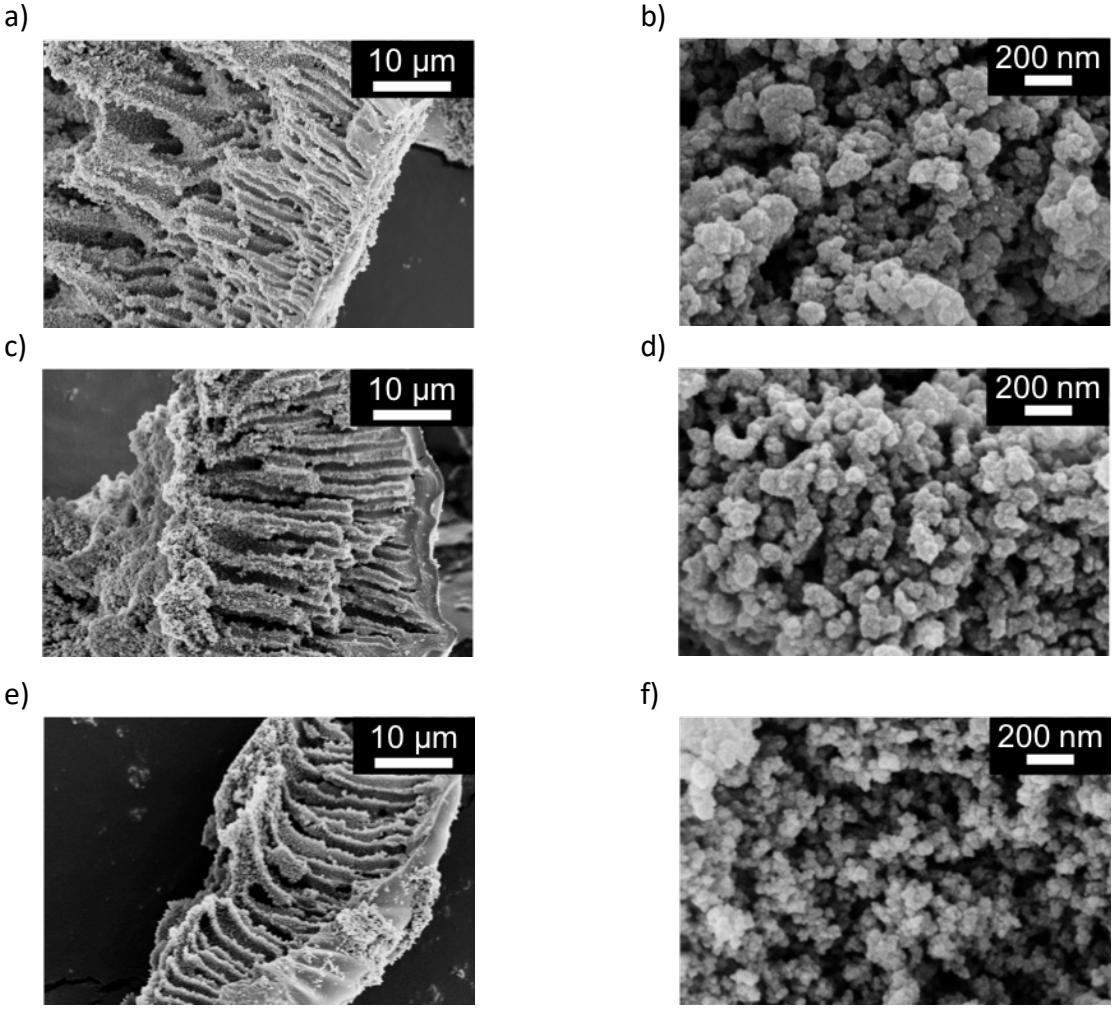

Figure 2.8: SEM images of green samples synthesized at a H_2O/TTIP ratio of 15 in the absence of IPA and (a, b) room temperature dried, (c, d) freeze-dried (frozen at -40°C), and (e, f) freeze-dried (frozen at -80°C)

dispersion by freezing in place the distribution of solids in the suspension [49, 53]. This effect was observed in this work, with freeze-dried samples exhibiting improved dispersion and fewer agglomerates consisting of fewer nanoparticles.

The XRD patterns for green samples dried at room temperature (not shown) and dried in the oven at 60°C (Figure 2.5a) are very similar, with anatase peaks appearing before sintering. The drying temperature and slow removal of excess water by evaporation in these samples may be a sufficient driving force for the condensation reaction and subsequent crystallization of anatase. Both freeze-dried samples (Figure 2.7a, b), however, exhibited more amorphous behavior. Samples placed in the freezer shortly after casting in the steel molds must have frozen before the reaction could be completed, hindering the crystalline arrangement of molecules and establishment of a long-range order. After sintering, an anatase-brookite mixture still appears in all samples except for S15-0M FD(-80), which would have frozen at an accelerated rate, causing the appearance of anatase and rutile peaks after sintering.

Nitrogen adsorption measurements reveal that the drying method does not have a significant effect on surface area. All four samples exhibit relatively large green surface areas ranging 440-620 $m^2 g^{-1}$, with the lowest value corresponding to G15-0M FD(-80) (Table 2.2). The higher value of 620 $m^2 g^{-1}$ for G15-0M FD(-40) can be attributed to improved preservation of macrochannels at longer scales as well as freezing of well-dispersed particles and avoidance of further agglomeration experienced in the samples dried at room temperature or in the oven at 60°C. After sintering, reduction in porosity and surface area are observed (30-60 $m^2 g^{-1}$). While S15-0M FD(-80) experienced a dramatic decrease in surface area, similar to samples prepared in the presence of IPA, S15-0M FD(-40) maintained a higher surface area value comparable to S15-0M RT and S15-0M OD.

Investigation of various drying methods showed that freeze-drying after freezing at -40°C produced multi-scale porous titania with the best architectural macrochannel features and meso-scale dispersion. Slower solvent removal techniques such as air drying at room temperature or in an oven at 60°C allowed particles to agglomerate, while samples prepared by more accelerated freezing at -80°C exhibited fewer macrochannels and showed evidence of lamellar pores typical

of ice-templating. On the other hand, freezing at -40°C seemed to preserve more defined macrochannels with improved particle dispersion and mesoporosity.

2.5. Conclusion

In this study, a fast, facile sol-gel based synthesis technique has been shown to successfully produce crystalline titania nanoparticles exhibiting multi-scale porosity. The use of excess water (H_2O/TTIP molar ratio ≥ 15) and absence of IPA as co-solvent resulted in the formation of macrochannels from the radial penetration of TTIP mini-emulsions. Further hydrolysis was localized within these emulsions and the path of excess water through the emulsion produced interconnected inter-agglomerate open pores after drying. Investigation of various H_2O/TTIP molar ratio values showed that macrochannels form at a value of 15, but that using a value of 30 produces more frequent and periodic macrochannels. Moreover, freeze-drying after freezing at -40°C resulted in more defined macrochannels and was shown to better preserve the lower-scale macro- and mesoporosity in the channel walls by freezing in place the particle dispersion in the suspension.

While hydrolyzing TTIP at a moderate H_2O/TTIP molar ratio of 30 in the absence of an alcohol so-solvent produced multi-scale porosity, the smaller macropores and mesopores produced by the pervasion of water throughout the mini-emulsions were undirected and randomly sized and spaced. Freeze-drying was shown to improve particle dispersion and hinder agglomeration; however, this synthesis method lacks the ability to tune interparticle spacing and morphology on the meso-scale. To resolve this challenge, the addition of a nanometric sacrificial material such as cellulose nanocrystals into this soft-templating technique may provide control over the meso-structure. This concept is explored in Chapter 3 with a combined surfactant-free self-assembly and hard-templating approach to prepare meso-structured multi-scale porous titania.

Chapter 3: Role of Cellulose Nanocrystals in Tailoring the Meso-Scale Morphology of Multi-Scale Porous Titania

3.1. Overview of Work

Investigation of synthesis parameters in the sol-gel hydrolysis of TTIP identified H_2O/TTIP molar ratio of 30, without addition of IPA, and freeze-drying after freezing at -40°C as the optimal settings to produce multi-scale porous titania exhibiting aligned macrochannels and reduced particle agglomeration. In an effort to more closely manage the meso-scale morphology, a sacrificial nanomaterial was used in a combined soft-templating and hard-templating route. Cellulose nanocrystals (CNCs) were incorporated into a fast, simple sol-gel synthesis of titanium dioxide to tune and more closely control the morphology and porosity on the meso-scale. The CNCs formed complex structures which interacted with the titania particles and established a meso-structure template. Freeze-drying preserved CNC dispersion in the colloidal suspension and prevented excessive agglomeration as experienced in oven-dried samples. As a result, the improved CNC dispersion increased opportunity for CNC-TiO_2 interactions and encouraged more faithful replication of the CNC template. After sintering at 450°C, the titania particles were arranged into meso-structures as a direct consequence of CNC templating. Quantification of surface area by the BET method confirmed the tunability of morphology with CNC addition in freeze-dried samples. Thus, multi-scale porous titania formed by the spontaneous formation of macrochannels by the sol-gel reaction of ceramic precursor can be controlled at the meso-scale by the synergetic effects of CNC hard-templating and freeze-casting.

3.2. Introduction

The study discussed in Chapter 2 investigated the effect of water content, IPA content and drying method on the formation of a multi-scale porous titania structure. According to the results reported in Chapter 2, the optimal synthesis parameters for achieving highly porous titania exhibiting self-assembled, aligned macrochannels in the sol-gel hydrolysis of TTIP were identified

as a H_2O/TTIP molar ratio of 30, without isopropyl alcohol, and freeze-drying after freezing at -40°C. However, aside from limited influence of drying method on mesoporosity, this template-free self-assembly technique does not offer a strategy to tailor the meso-structure which may be necessary to improve the performance of titania in various fields.

Several groups have investigated diverse templating techniques, including using an assortment of hard-templates to prepare titania samples with tunable meso-structured morphology [43, 44]. Recent attention has been directed to the nanometric biomaterial cellulose as one of the most promising of these templates. Cellulose can come in numerous forms whose morphological characteristics depend on the source organism (e.g. plant, bacteria, algae, tunicates) and extraction method and can exhibit a range of dimensions (5-50 nm in width and 100 nm-5 µm in length), aspect ratios, crystallinity, and purity [111, 164–167]. This variety of cellulose along with its naturally occurring abundance allows its wide applicability across industries and uses, including as a reinforcing agent in polymer composites [123–129], as a stabilizer of dispersions and emulsions [130–134] and its implementation in drug carriers [135–138]. However, properties of chemical modifiability, physical and chemical inertness, hydrophilicity, and nanometric dimensions make cellulose a very promising candidate for a hard-template in creating meso-structured ceramics [165]. Moreover, its low degradation temperature relative to sintering temperatures of titania allows for a single-step thermal treatment to simultaneously remove the template and partially sinter the ceramic particles.

Literature already reports the success of cellulose nanomaterials in tailoring the final titania morphology [135, 146, 147, 152–155, 159–161]. Shopsowitz et al. used cellulose-templated silica as an intermediate hard-template to produce titania samples with a chiral nematic porous morphology, citing the generally volatile hydrolysis reaction of titania precursors as a major limitation that necessitates an intermediate template [152]. However, other groups show that it is possible to directly template titania with cellulose. Ivanova et al. [154, 159] and Yoon et al. [160] report the tunability of the titania morphology on the meso-scale with varying content of cellulose nanocrystals (CNCs) and sintering parameters. Both sets of authors claim that the CNCs serve multiple purposes acting as sacrificial material to generate pores, confining the growth of titania particles at high compositions, and providing heterogeneous nucleation sites for titania

particles. Thus, the use of CNCs as a sacrificial hard-template has been shown to successfully tailor the meso-morphology of titania. However, these CNC-templated titania samples do not exhibit a multi-scale porous structure, which has been reported to improve performance in applications such as photocatalysis [15, 22, 70–72].

Several reports by Huang and his group have shown the feasibility of combining cellulose with other strategies in a dual-template synthesis of titania [153, 155, 168]. Nanotube/hollow sphere hybrids were prepared by depositing titania precursor solution on cellulose fibers followed by deposition of colloidal sacrificial microspheres (silica and polystyrene were investigated) and an additional deposition cycle of titania precursor solution, before the templates were removed by thermal burn-out and chemical extraction methods. Thus, cellulose nanomaterials can be used in a combined templating strategy to prepare a complex titania nanotube/hollow sphere hybrid. However, the authors resorted to using another hard-template and rather complicated synthesis procedures. It remains to be shown whether cellulose nanomaterials can be incorporated into a self-assembly technique in a more facile combined templating strategy to produce meso-structured multi-scale porous titania.

The following investigation incorporates cellulose nanocrystals in a combined soft-templating and hard-templating technique to tailor the meso-scale morphology of multi-scale porous titania. The data reveals that samples prepared with CNCs as hard-templates in this combined templating technique continue to exhibit aligned macrochannels as a result of the formation mechanism previously described and whose meso-morphology is effectively tailored by the addition of CNCs and their interaction with titania precursor particles. Thus, CNCs successfully meso-structure multi-scale porous titania by incorporating the bio-template into the facile and versatile sol-gel method using the synthesis settings chosen in Chapter 2. The work presented shows the feasibility of tuning the mesoporous structure of multi-scale porous titania by the addition of CNCs as sacrificial material in a combined template-free self-assembly and hard-templating technique.

3.3. Experimental

3.3.1. Synthesis

Titanium tetra-isopropoxide (TTIP), used as received (Sigma-Aldrich, 97%), served as the ceramic precursor in the hydrolysis reaction with deionized water to form titanium dioxide. Cellulose nanocrystals (5-20 nm in diameter and 100-200 nm in length) from a 11.8wt% slurry (University of Maine, Process Development Center, Maine, USA) were incorporated as templates.

A desired mass of cellulose slurry was diluted with the appropriate volume of water and stirred magnetically at 275 rpm for approximately 5 minutes. The amount of CNC slurry added is varied to achieve compositions of 0, 5, 10, 20, and 50vol% CNC in the dry, green CNC-TiO_2 composites. To this diluted slurry, TTIP was added by micropipette, forming a white precipitate. Amounts of TTIP and water added were chosen such that H_2O/TTIP molar ratio = 30, as the findings described in Chapter 2 point to this as the optimal value for forming periodic macrochannels. The suspension was mixed with a stirring rod before being pulse sonicated (Fisherbrand Model 705 Sonic Dismembrator, USA) in an ice bath for 2 minutes at a 40% power output with a rate of 1 second on, 1 second off. After sonication, the suspension was manually stirred again with a stirring rod before being cast into a stainless steel cylindrical mold (25 mm height and 22 mm internal diameter) and dried. Samples were either oven dried at 60°C or freeze-dried. In the latter case, casts were frozen at -40°C and dried for 36 hours with a Labconco FreeZone 2.5L Freeze Dry System (USA) whose condenser coil was held below -80°C at a chamber pressure below 0.03 mBar. All green samples were sintered in a box furnace (Deltech Furnaces Front Load DT-31-FL-6, USA) at 450°C for 1 hour with a heating rate of 2°C min^{-1} and cooling rate of 5°C min^{-1}. This single sintering step served to simultaneously burn-out the CNCs and partially sinter the titania nanoparticles. The prefixes “G” and “S” are again used to distinguish between green and sintered samples, respectively. This is followed by the CNC content (0, 5, 10, 20, or 50) and the drying method (OD or FD) to identify individual samples.

3.3.2. Characterization

Morphology of multi-scale porous samples was investigated with a LEO Zeiss 1550 field-emission scanning electron microscope (FESEM) at an accelerating voltage of 5 keV (samples were coated with 15 nm of iridium with a Leica EM ACE600, Germany). A JEOL S/TEM 2100

(Japan) transmission electron microscope (TEM) at an accelerating voltage of 200 keV was used to study nanoparticle size, shape, and crystallinity. Porosity and surface area were measured by nitrogen adsorption-desorption in a Quantachrome NOVA-e Series system (USA). Samples were degassed overnight at 100°C and analyzed with a 41-point spread in the relative pressure range 0.01-0.99. Specific surface area was calculated according to the multi-point Brunauer-Emmett-Teller (BET) method from the adsorption data in the relative pressure range of 0.05-0.3. Pore volume and pore size distribution curves were calculated with the Barrett-Joyner-Halenda (BJH) method at the maximum relative pressure and by analysis of the desorption branch, respectively.

3.4. Results and Discussion

3.4.1. Preservation of Multi-Scale Porosity

Figure 3.1 depicts the macrochannels that form in all samples as a result of the hydrolysis mechanism of TTIP in excess water in the absence of an organic alcohol solvent. According to the mechanism identified in Chapter 2, in the absence of a co-solvent and retarding agent such as isopropyl alcohol, TTIP droplets react at the surface to form mini-emulsions with semi-permeable membranes and their infiltration by water forms the macrochannels observed. When CNCs are incorporated into the synthesis procedures by preparing an aqueous suspension in the form of a diluted slurry before initiating the hydrolysis reaction by adding TTIP, this macrochannel formation mechanism is unimpeded. Thus, the presence of CNCs does not disrupt the development of a multi-scale porous structure similar to those observed in Chapter 2. Although literature reports the ability of CNCs and other cellulose nanomaterials to stabilize emulsions [132, 133], analysis of the macrochannel diameters and periodicity in this work shows no significant dependence on CNC addition. Therefore, the accelerated reaction kinetics of the hydrolysis of TTIP in excess water along with the small relative portion of CNCs (up to 6wt%) in the diluted CNC-H_2O slurry inhibit any potential contribution from CNCs to the early

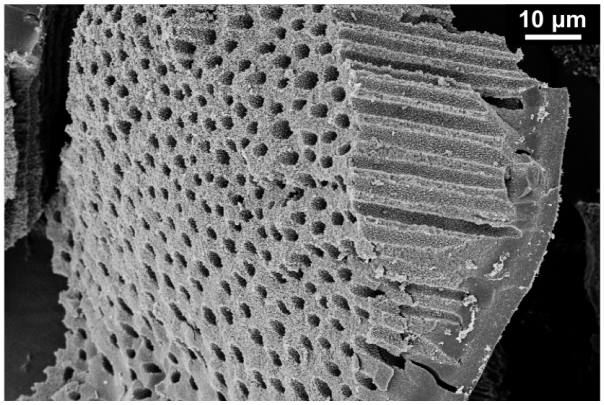

Figure 3.1: SEM image of G5%-FD shows the macrochannels (1-3 µm in diameter, 20-40 µm in length) present in all samples as a result of hydrolysis of TTIP at H_2O/TTIP ratio of 30 and unhindered by the CNCs

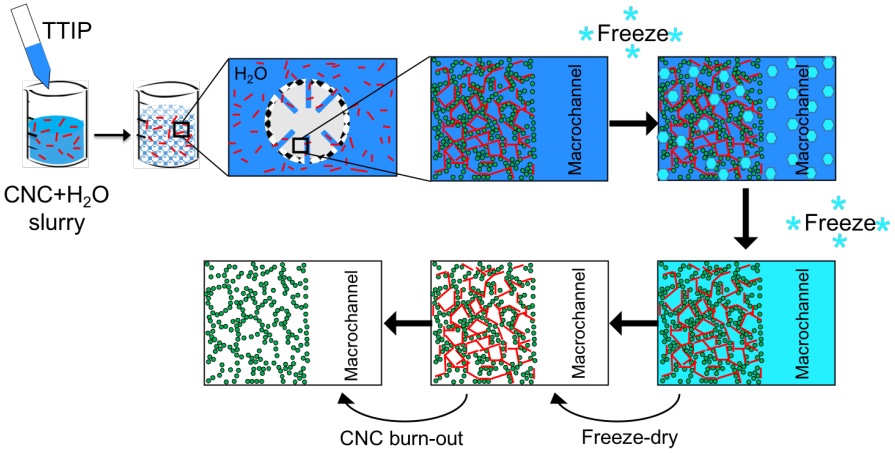

Figure 3.2: Schematic depicts the role of CNCs in tailoring the meso-scale morphology of multi-scale titania

stages of the emulsion formation process and nucleation of titania precursor particles. However, once water begins to infiltrate the mini-emulsion, the hydrophilic nature of CNCs leads the polymer whiskers to accompany the water molecules and penetrate the TTIP droplets via the macrochannels formed, as depicted in Figure 3.2. As the water continues to react with the channel walls and propagates through the emulsion, the CNCs follow and interact among themselves and with the titania nanoparticles, causing changes in the meso-morphology.

3.4.2. Effect of CNC Addition on Freeze-Dried Samples

3.4.2.1. Green Samples

Figure 3.3 shows SEM images of freeze-dried samples and gives some insight into the role CNCs play in changing the morphology of the final ceramic. In the absence of CNCs, the blank G0%-FD sample (Figure 3.3a) exhibits sizable aggregates of titania nanoparticles separated by macropores of a few hundred nanometers. As CNC concentration increases, the whiskers tend to shift from being isolated to interacting and connecting to form complex structures. This leads to reduction of titania aggregation and increase in interconnectivity. As water diffuses through the mini-emulsion during localized hydrolysis, the CNC whiskers become inter-dispersed with the titania precursor spheroidal particles that nucleate, as is observed. At low relative contents, individual CNC whiskers can be seen bridging small aggregates of titania particles (examples are circled in Figure 3.3b, c). The low compositions of 5% and 10% allows the CNCs to be sufficiently distributed as separate whiskers and individually interact with titania particles to disrupt aggregates and form smaller particle assemblies and connect otherwise separate aggregates. At

higher concentrations, the CNCs become more connected and form a complex web-like structure (some examples are circled in Figure 3.3d, e). Abundant hydroxyl groups at the CNC surfaces interact by hydrogen bonding and lead CNCs to agglomerate and form complex structures. According to literature, CNCs tend to agglomerate by co-aligning and stacking in parallel [116, 117, 120]. However, the web morphology observed in these freeze-dried samples is characterized by non-aligned CNCs and increased spacing between whiskers as a result of the freeze-casting method. Similar to observations made in Chapter 2, freezing the solvent effectively locks the particles and whiskers in place as they were positioned in suspension. This is particularly advantageous in maintaining the dispersion of CNCs as generally discrete, albeit interconnected whiskers, which otherwise tend to extensively agglomerate by hydrogen bonding of surface hydroxyl groups as confirmed by comparison to OD samples and reported by literature [111, 167, 169, 170]. This improved dispersion and prevention of CNC agglomeration in FD samples preserves the availability of surface hydroxyl groups and increases opportunity for CNC-TiO_2 interaction and adsorption.

The available hydroxyl groups at the CNC surfaces interact with the titania precursor particles and allow the establishment of adsorption between the particles and the CNCs [147]. The interaction

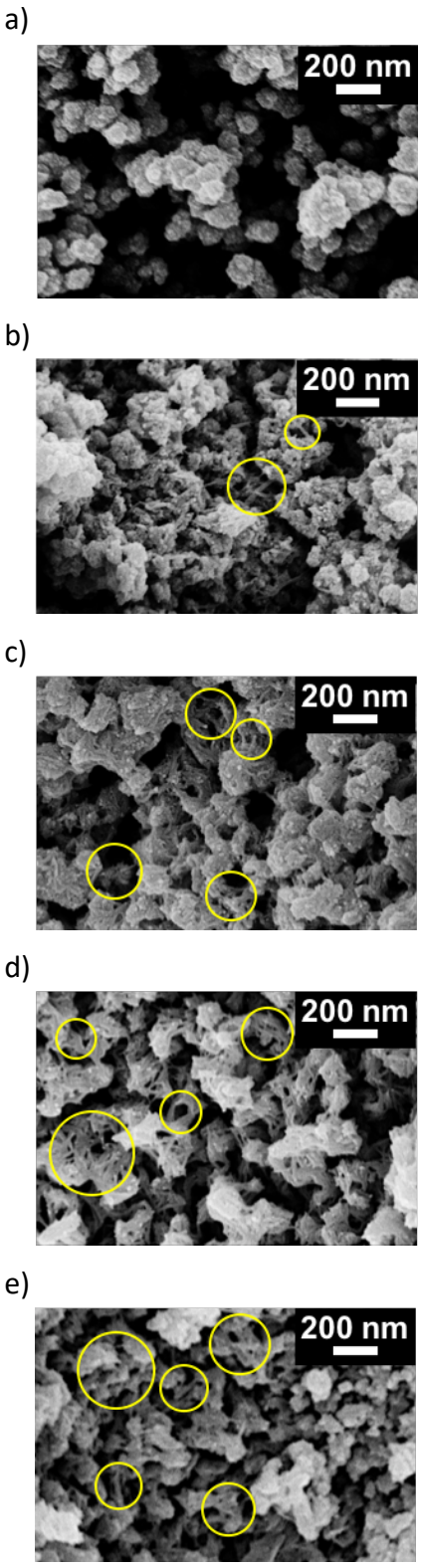

Figure 3.3: SEM images of green FD samples at CNC contents of a) 0%, b) 5%, c) 10%, d) 20%, and e) 50% show bridging of titania aggregates and formation of complex web structure by the CNCs

between these materials is evidenced by the bridging of titania aggregates by CNC whiskers and adsorption of titania nanoparticles onto the cellulose complex structures seen in Figure 3.3 and is supported by literature [72, 145–147, 151, 158, 171]. The retention of these interparticle effects even after disruption to the mixture by sonication eliminates physisorption by weak van der Waals forces as the root cause of the interaction [145]. Therefore, these strong interactions must be either electrostatic or chemical in nature. However, since samples are prepared at the natural, unadjusted pH, purely electrostatic interaction is unlikely. The natural suspension pH of approximately 6 coincides with the IEP of titania, which is reported to be between 5 and 7 [89–93]. Therefore, titania particles exhibit both positively and negatively charged surfaces in suspension, disqualifying electrostatic interaction by attraction of negatively charged CNC surfaces as the dominant adsorption mechanism of titania particles and CNC whiskers. Therefore, chemisorption in the formation of Ti-O-C bonds may also play a role in the strong CNC-TiO_2 interaction observed [146, 151, 158]. Ceramic precursor molecules may react at the CNC surfaces with the exposed hydroxyl groups in a quasi-condensation reaction to form these Ti-O-C chemical bonds and establish strong CNC-TiO_2 interparticle adsorption. More work is needed to further elucidate the nature of the adsorption of titania particles to the CNC whiskers. However, these interactions lay the foundation for using CNCs to meso-structure titania, as observed in sintered samples after template burn-out.

3.4.2.2. Sintered Samples

Green samples were sintered at 450°C to simultaneously decompose the CNC template and initiate particle necking and growth of the titania particles in a single sintering step. This relatively low sintering temperature allows the ceramic particles to partially sinter and burns out the CNCs without risking premature template structure collapse as can sometimes occur with polymer and bio-templates. By partially sintering the ceramic particles, the final body can preserve the structure established by the hard-template while conserving the micro- and mesoporosity found in the green samples by limiting densification. This can be seen in Figure 3.4 where the arrangement of titania particles is observed to replicate the CNC structures established in the dry, green samples.

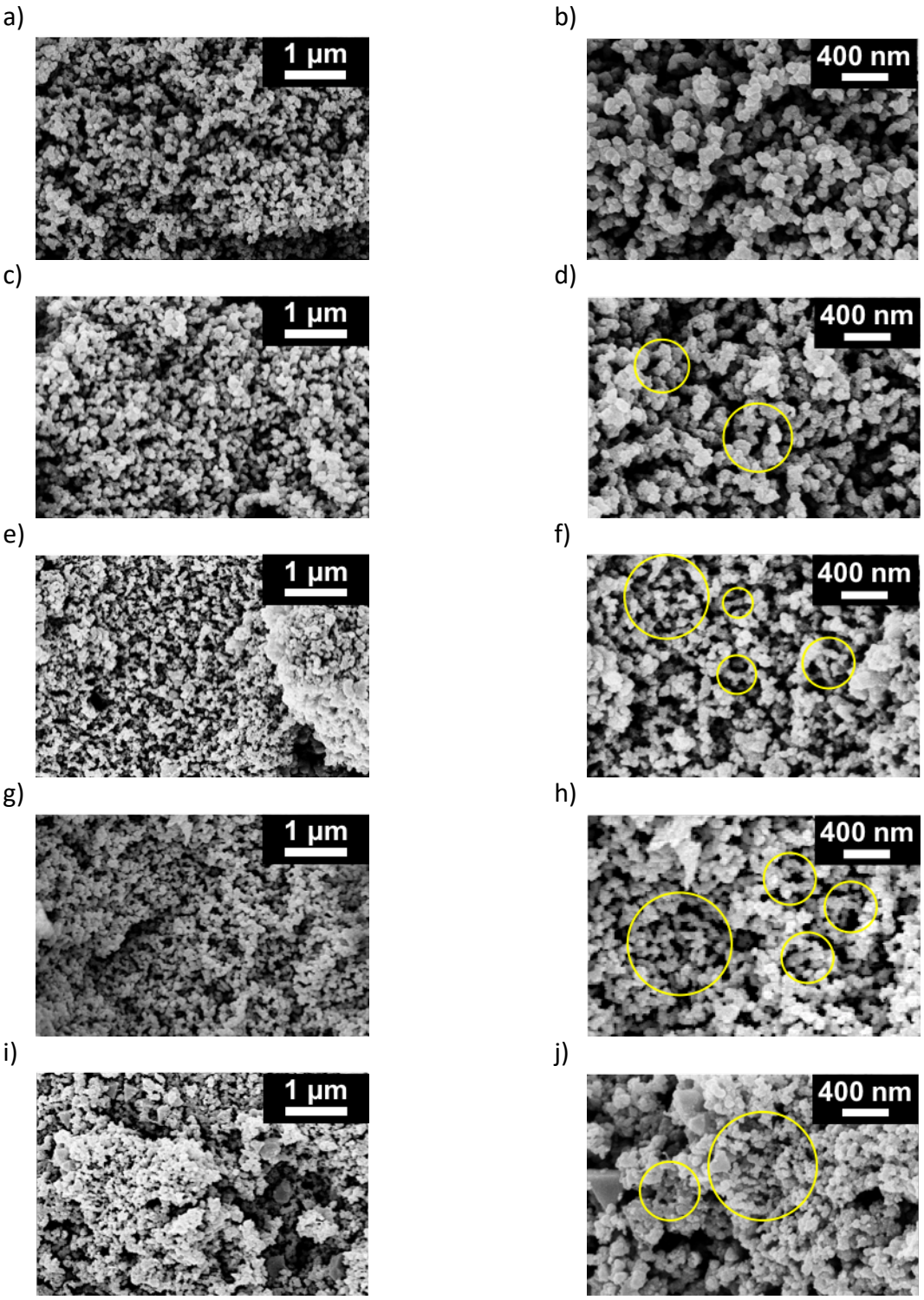

Figure 3.4: SEM images of sintered FD samples at CNC contents of (a, b) 0%, (c, d) 5%, (e, f) 10%, (g, h) 20%, and (i, j) 50% show successful tailoring of the TiO_2 meso-structure as evidenced by a decrease in titania aggregation and pore size and increase in interconnectivity with increasing CNC content

Figure 3.4 shows SEM images of sintered samples and typifies the changes in morphology observed with increasing CNC content. As CNC concentration during synthesis increases, sintered

samples exhibit morphologies consisting of titania particles that are less aggregated and more interconnected. While the blank S0%-FD sample consists of large titania agglomerates separated by macropores (Figure 3.4a, b), samples that were prepared with CNCs exhibit smaller mesopores and smaller titania aggregates that are more interconnected. Chen, Kuo, and Lu similarly show an improvement in particle dispersion with CNC templating in a complex procedure to prepare N-doped mesoporous titania [157]. In this work, the presence of CNCs and their low degree of agglomeration in FD samples increases opportunity for the development of CNC-TiO_2 interaction and hinders TiO_2-TiO_2 interaction and particle agglomeration. At low CNC concentrations of 5% and 10% (Figure 3.4c-f), sintered samples exhibit fewer aggregates composed of fewer titania particles than the blank sample prepared in the absence of the CNC template. This is due to the tendency of individual CNC whiskers to inter-disperse between titania particles and disrupt agglomeration of ceramic particles during synthesis as is observed in the green samples (Figure 3.3b, c). Moreover, the CNCs' dispersion and bridging of titania aggregates in the green samples translate in sintered samples, as observed, to increased interconnectivity among ceramic aggregates and a more open structure with CNC addition.

At higher CNC concentrations of 20% and 50%, sintered samples exhibit morphologies that mimic the complex web structure observed in Figure 3.3. These samples continue to experience less aggregation of titania particles and increased interconnectivity as can be observed in Figure 3.4g-j. More significantly, however, the arrangement of titania particles and the structures at a larger scale replicate the CNC interconnected complex structures that form from CNC-CNC interactions in the suspension. Caruso and Schattka show a similar effect in producing a porous TiO_2 network by soaking a cellulose acetate membrane in a precursor solution [156]. Coating of the membrane features and subsequent controlled hydrolysis in a water-isopropanol solution and sintering resulted in faithful replication of the template. However, these samples did not exhibit a multi-scale porous structure as is accomplished in this work by incorporating individual CNC whiskers in a combined soft- and hard-templating strategy. The successful templating of these titania complex structures in sintered samples is reliant on proper interaction between template and ceramic. This is granted by the freeze-casting effect of securing increased porosity between CNC whiskers and preventing excessive agglomeration and co-aligned stacking of the

template. Thus, the strong interaction between titania particles and CNC whiskers afforded by the freeze-casting effect allowed the CNCs to template the final ceramic and resulted in titania morphologies that mimic the CNC interconnected structures seen prior to sintering.

3.4.3. Effect of CNC Addition on Oven-Dried Samples

These findings of the synergetic effects of CNC templating and freeze-drying were confirmed by comparison to similar samples prepared by oven-drying. Figure 3.5 consists of SEM images of green and sintered oven-dried samples prepared with 0%, 10% and 20% CNC content. It was observed that CNCs are less effective in templating the final titania structure in oven-dried samples than after freeze-drying. CNCs can still assemble into a complex structure in oven-dried samples, as is seen for G20%-OD (Figure 3.5e). However, the mobility of CNCs during slow solvent removal in oven-drying and the resultant CNC-CNC hydrogen bonding due to the abundant hydroxyl end groups prompt the template to agglomerate to a higher degree than is observed in

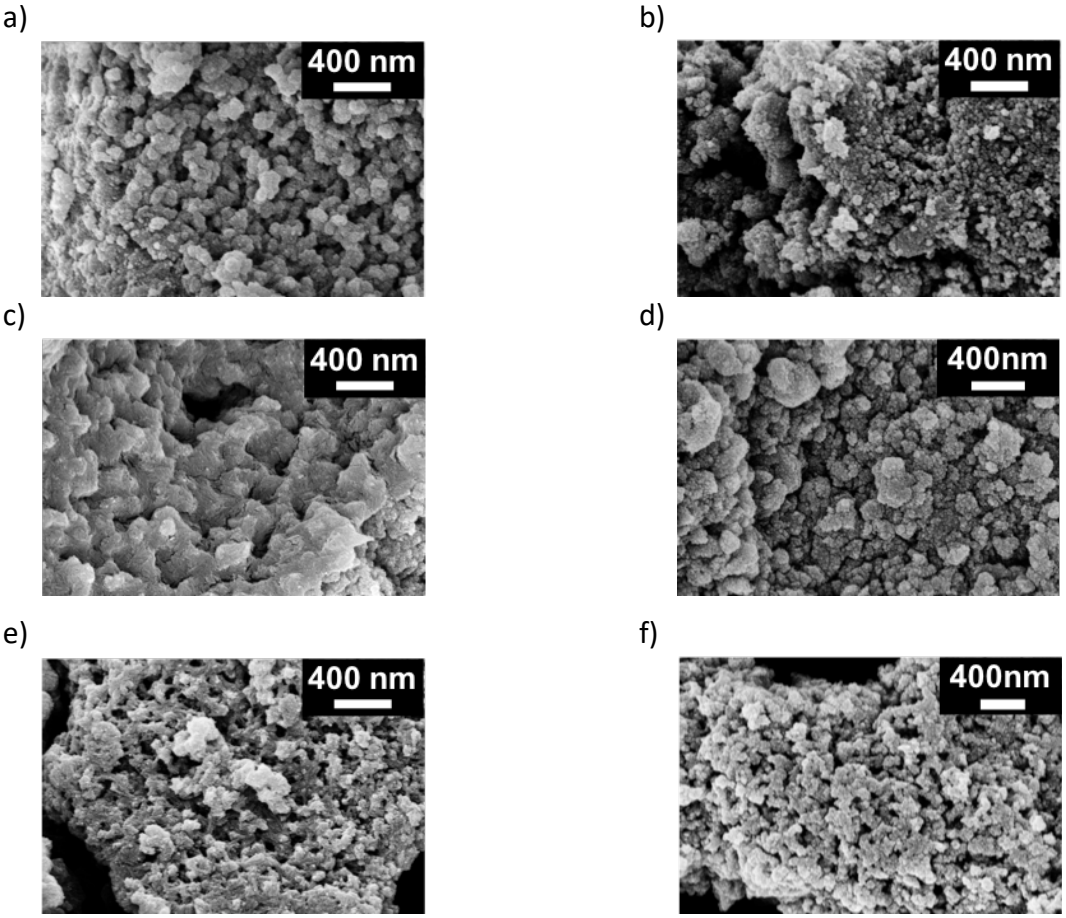

Figure 3.5: SEM images of a) G0%-OD, b) S0%-OD, c) G10%-OD, d) S10%-OD, e) G20%-OD, and f) S20%-OD show CNC agglomeration in green samples and limited replication in TiO_2 samples after sintering

freeze-dried samples. This causes thick struts in the architecture of the template structure composed of agglomerated, co-aligned CNCs. This is in contrast to the web structure observed in FD samples, which exhibits better CNC dispersion and thinner features. In extreme cases, the CNCs agglomerate to the point of covering the macrochannel walls, as is seen in Figure 3.5c. Additionally, excessive CNC-CNC bonding and agglomeration of the template in OD samples limit the possibility for CNC-TiO_2 interactions [147]. This lack of sufficient bonding between CNCs and the titania particles inhibits the replication of the template in the final ceramic body. This is evidenced by observation of the sintered ceramic samples which are not successfully templated by the CNCs (Figure 3.5d, f), and whose structures resemble those found in the blank sample prepared in the absence of CNCs (Figure 3.5a, b).

3.4.4. Physical Properties of CNC-Templated Titania

Nitrogen adsorption-desorption studies were conducted to support and quantify the morphologies observed by SEM. Figure 3.6 shows plots of average surface area of sintered samples (calculated according to the multi-point BET method) and reveals its dependence on CNC content, particularly for FD samples. The data shows an increase in surface area at a CNC concentration of 5% followed by a decreasing trend with further CNC addition. TEM analysis was conducted to investigate whether variations in particle size in samples contribute to the surface area trends observed. While literature reports the formation of smaller titania particles with increased CNC content [157, 159, 160], no such trend was observed in this work. According to TEM analysis, samples exhibited an average particle size of 11-12.5 nm with a standard deviation of 3-5 nm, independent of CNC content and drying method. This lack of an observable trend in

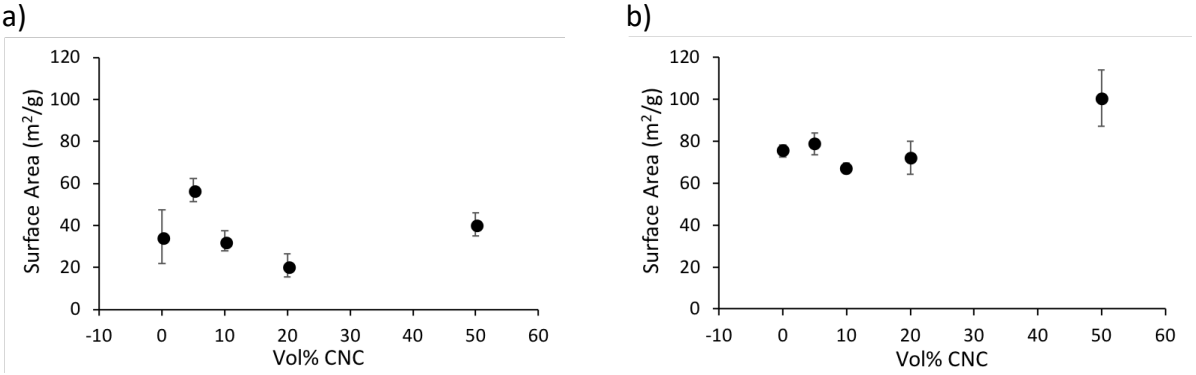

Figure 3.6: Average BET specific surface area measurements with one standard deviation of a) FD and b) OD sintered samples plotted with CNC content show the dependence of FD surface area on CNC content, while OD surface area exhibits no significant changes as function of CNC content

particle size may be attributed to the use of lower CNC contents than reported in literature and the absence of HCl [159, 160] and other solvents [157] during synthesis, which would have retarded the nucleation rate and amplified the impact of the CNCs on the titania particle size. This suggests that the changes in surface area are a direct effect of the meso-structure and confirms the morphological evidence that CNCs successfully altered the meso-structure of the titania samples.

As surface area is dependent on porosity (volume and size distribution), particle size and aggregation, the higher surface area value of S5%-FD may point to a favorable balance between reduced aggregation, interconnectivity, and porosity. This balance is a result of the dispersion of CNCs in the green sample as isolated whiskers that bridge and disrupt aggregates. This is supported by literature which reports that CNCs are optimally dispersed at a concentration below 10% [111, 170]. Above this concentration, CNCs begin to interact and connect together to eventually form complex structures. Thus, samples prepared with 10% and 20% CNC content exhibit further interconnectivity as observed by SEM (Figure 3.4), tilting the balance found in S5%-FD, reducing exposed surfaces and resulting in the trend of decreasing SSA that is observed. As for S50%-FD, the restoration of a higher surface area value indicates insufficient templating of the titania structure, possibly due to increased agglomeration of CNCs at such a high concentration. This diminishes the ability of CNCs to interact with TiO_2 particles and disrupt titania aggregation and leads to a surface area value comparable to that of the blank S0%-FD sample. This is even more true in OD samples, where excessive CNC agglomeration experienced during slow solvent removal inhibits the CNCs from effectively altering the titania morphology. This is confirmed by surface area measurements of OD samples that show no trend and no correlation to CNC content. Thus, the synergetic effect of CNC templating and freeze-drying led to the successful tailoring of the meso-structure of multi-scale porous titania whose morphology can be tuned by varying CNC content used during synthesis.

3.5. Conclusion

The addition of CNCs as hard-template to the sol-gel reaction of titania tetra-isopropoxide provided a tool to tune the meso-scale morphology of multi-scale porous titania in a facile, and versatile combined templating strategy. This novel technique simultaneously induced a multi-

scale porous structure by the template-free self-assembly of aligned macrochannels and tailored the titania meso-structure by incorporating CNCs as the nanometric template in the synthesis procedures. The formation mechanism of aligned macrochannels by the hydrolysis of TTIP in excess water was uncompromised by the CNCs, which inter-dispersed within the mini-emulsions and laid the foundation for titania replication on the meso-scale. Freezing and freeze-drying assisted the development of the CNC structures by freezing them in place in suspension and reducing CNC agglomeration. This resulted in the dispersion of individual CNC whiskers at low concentrations and the formation of a complex web-like structure characterized by non-aligned whiskers at high concentrations. This reduction in excessive agglomeration and co-aligned stacking of CNCs and improvement in porosity from the freeze-casting effect increased opportunity for CNC-TiO_2 interactions and encouraged more faithful replication of the CNC template by the ceramic nanoparticles.

A single sintering step simultaneously burned out the template and partially sintered the ceramic particles. At low concentrations of 5% and 10%, individual CNC whiskers disrupted particle aggregation and bridged aggregates, resulting in sintered samples exhibiting smaller titania aggregates that are more interconnected. At higher concentrations of 20% and 50%, CNCs interacted to form a complex web structure that is successfully replicated by the titania particles and their meso-structured arrangement after sintering. Measurement of surface area and particle size confirmed the successful tailoring of the titania morphology with CNCs. A high surface area for S5%-FD with a decreasing trend at higher compositions was observed and attributed to changes in the balance between reduced aggregation, interconnectivity, and porosity. The results were shown to be unique to freeze-dried samples by comparison to oven-dried samples, which exhibited excessive CNC agglomeration and limited CNC-TiO_2 interactions. Thus, a novel combined templating technique consisting of surfactant-free self-assembly, CNC hard-templating and freeze-casting successfully produced meso-structured multi-scale porous titania bodies exhibiting aligned macrochannels with tunable mesoporosity and morphology.

Chapter 4. Suggested Future Work

To further elucidate the tunability of the multi-scale porous structures observed, the following future work is suggested. While the scope of the work presented in this thesis was limited, there is evidence that the H_2O/IPA ratio plays a crucial role in determining whether hydrolysis and nucleation occurs homogeneously or locally within emulsion droplets. Therefore, expansion of the ratio values tested in this thesis and formation of a TTIP-IPA-H_2O ternary phase diagram will help guide future work on the formation of macrochannels by setting compositional limits within which each nucleation mechanism dominates. Microscopy in-situ and in real time of the hydrolysis reaction of TTIP in excess water and absence of IPA will confirm the macrochannel formation mechanism and may reveal insight into methods to tune the macrochannel dimensions and periodicity. While electron microscopy is preferred for these in-situ studies, an optical microscope may be sufficient and more practical. To better understand the establishment of long-range crystalline order observed in oven-dried and room temperature dried samples, samples can be collected from the oven in intervals throughout the drying duration, quickly frozen in liquid nitrogen and freeze-dried. XRD analysis of these samples will reveal the time needed at particular drying temperatures for the crystalline order to set.

If more direct replication of individual CNC whiskers is desired, reaction kinetics and CNC-TiO_2 interactions must be more closely managed. This can be accomplished by various techniques. IPA can be used as a co-solvent to slow down the reaction and potentially allow CNCs to interact more intimately with the hydrolysis-condensation reaction and nucleation of titania particles. However, this forfeits the multi-scale porous structure observed. The order in which the materials are mixed may also play a role. While this work was conducted by adding TTIP into an aqueous suspension of CNCs, first dispersing dry CNCs in TTIP followed by addition of H_2O may give TTIP opportunity to coat the CNCs and possibly begin hydrolyzing with the surface hydroxyl groups to establish bonding between the ceramic precursor and template. The subsequently added H_2O will react with the remaining TTIP at the accelerated rate observed in this work and theoretically still will prompt the macrochannel formation mechanism. Alternatively, CNC-TiO_2 interactions can be tailored using colloidal processing routes including adjusting pH such that it

lies below the isoelectric point of titania (pH ~ 5-7). This will cause the titania particles to take on positive surface charges, while the CNCs will maintain their negative charges. These charges should promote dispersion by hindering CNC-CNC and TiO_2-TiO_2 interactions and encourage CNC-TiO_2 interactions by attraction of opposite charges. However, it is important to keep in mind that titania phase evolution may also be affected as certain polymorphs are preferred in certain environments.

The simple synthesis of these multi-scale porous titania by the sol-gel method is very versatile and can be easily adapted to achieve the desired final morphology. The synthesis of titania in suspension allows for a combination of templating techniques to be used and permits the investigation and exploitation of the benefits presented by colloidal processing techniques.

Chapter 5. Summary and Conclusions

The fabrication of multi-scale porous titania has been successfully achieved by the simultaneous use of three templating techniques: template-free self-assembly, freeze-casting, and CNC hard-templating. A systematic study was conducted to identify the effects of synthesis parameters on the formation of a multi-scale porous body. Reaction kinetics and the nucleation mechanism were recognized as crucial factors in determining the morphology of the final ceramic. The spontaneous formation of aligned macrochannels was directly linked to the hydrolysis of TTIP at moderate H_2O/TTIP molar ratio values (15, 30, 60) in the absence of IPA. The accelerated reaction kinetics and immiscibility of TTIP and water prompted the formation of mini-emulsions upon mixing of the two liquids. The partial hydrolysis at the interface created a semi-permeable membrane that allowed penetration by water in radial macrochannels and localized further hydrolysis within the formed emulsion droplets. It was further revealed that hydrolysis at these molar ratios in the absence of IPA as a reaction retarding agent gave way to the arrangement of TiO_2 molecules in long-range order exhibiting biphasic anatase-brookite crystallinity after oven-drying before sintering. However, freezing at -40°C and subsequently freeze-drying the samples produced more defined macrochannels and preserved the dispersion of particles in the suspension preventing agglomeration and promoting more mesoporosity. It was proposed that IPA acted as a co-solvent and promoted homogeneous nucleation rather than the production of emulsions and consequent localized hydrolysis, hindering the formation of macrochannels. The common use of organic solvents in hydrolysis of titania precursors to better manage the reaction kinetics explains the scarcity of reports on this macrochannel structure in literature. Consideration of these findings led to the identification of H_2O/TTIP molar ratio = 30, in the absence of IPA and freeze-drying as the optimal parameters for the hydrolysis of TTIP and formation of multi-scale porous titania with aligned macrochannels.

As this strategy did not provide a method for tailoring the meso-structure, this facile self-assembly synthesis of multi-scale porous titania was combined with the hard-templating technique using CNCs as sacrificial material to more closely control the mesoporosity and arrangement of titania particles. The macrochannel formation mechanism was unimpeded by the

addition of CNCs into the procedure due to the accelerated kinetics of the hydrolysis reaction. However, once the macrochannels formed, the CNCs accompanied the water molecules in penetrating the mini-emulsion droplets and played more significant roles in the local hydrolysis and arrangement of titania nanoparticles. Morphological studies revealed that the CNCs reduced titania aggregation and increased interconnectivity. At low concentrations of 5% and 10%, the freeze-casting effect of preserving particle dispersion in suspension allowed individual CNC whiskers to inter-disperse, disrupt titania aggregation and bridge titania aggregates that formed, resulting in sintered samples that exhibited smaller aggregates that are more interconnected. At higher concentrations of 20% and 50%, CNCs interacted among themselves to form complex web structures characterized by non-aligned, interconnected whiskers afforded by the freeze-casting effect and resulted in meso-structured titania samples that mimic this structure after sintering. It is proposed that improved dispersion of CNC whiskers in freeze-dried samples encouraged CNC-TiO_2 interactions and resulted in more successful replication of the CNC complex structure by the titania nanoparticles. This is confirmed by comparison to samples prepared by oven-drying, which revealed increased CNC agglomeration as result of slow solvent removal. This hampered CNC-TiO_2 interactions and prevented successful templating of the titania meso-structures. Specific surface area measurements confirmed and quantified the changes observed in morphology, showing a correlation to CNC content in freeze-dried samples, whereas oven-dried samples showed no significant dependence on CNC content. Thus, the morphology of titania samples on the meso-scale was tuned by the synergetic effects of CNC hard-templating and freeze-casting and maintained the template structures after a single CNC burn-out and sintering step.

It has been shown that meso-structured multi-scale porous titania can be synthesized in a combined templating technique by the simple hydrolysis of TTIP at a moderate hydrolysis ratio (H_2O/TTIP) in the absence of IPA, whose macroporosity consisted of aligned macrochannels, which self-assembled as a byproduct of the accelerated reaction kinetics and whose meso-structure and local arrangement of titania particles can be tailored by the synergetic effects of freeze-casting and CNCs as hard-templates.

References

1. Hubadillah SK, Othman MHD, Ismail AF, et al (2018) Fabrication of low cost, green silica based ceramic hollow fibre membrane prepared from waste rice husk for water filtration application. Ceram Int 44:10498–10509
2. Zhang Y-G, Zhu Y-J, Xiong Z-C, et al (2018) Bioinspired Ultralight Inorganic Aerogel for Highly Efficient Air Filtration and Oil-Water Separation. ACS Appl Mater Interfaces 10:13019–13027
3. Ahmad N, Binti Mohd Zaidan N, Bazin MM (2013) Fabrication and Characterization of ceramic membrane by Gel Cast technique for water filtration. Adv Mater Res 686:280–284
4. Acosta G FA, Castillejos E AH, Almanza R JM, Flores V A (1995) Analysis of liquid flow through ceramic porous media used for molten metal filtration. Metall Mater Trans B Process Metall Mater Process Sci 26:159–171
5. Gehre P, Schmidt A, Dudczig S, et al (2018) Interaction of slip- and flame-spray coated carbon-bonded alumina filters with steel melts. J Am Ceram Soc 101:3222–3233
6. Liang L, Li J, Lin H, et al (2006) Relation between porosity and permeability of ceramic membrane supports. In: Advanced Materials Research. Beijing, China, pp 39–42
7. Yamakawa O, Shirakawa H, Sakurada O, Hashiba M (2010) Evaluation of filtration efficiency for single layer and double layers alumina filter using aqueous suspension. J Jpn Inst Light Met 60:505–510
8. Damodaran VB, Bhatnagar D, Leszczak V, Popat KC (2015) Titania nanostructures: A biomedical perspective. RSC Adv 5:37149–37171
9. Nathanael AJ, Im YM, Oh TH, et al (2015) Biomimetic hierarchical growth and self-assembly of hydroxyapatite/titania nanocomposite coatings and their biomedical applications. Appl Surf Sci 332:368–78
10. Liu Y, Yang Y (2016) Recent Progress of TiO2-Based Anodes for Li Ion Batteries. 2016:
11. Yang MC, Lee YY, Xu B, et al (2012) TiO2 flakes as anode materials for Li-ion-batteries. J Power Sources 207:166–172 . doi: 10.1016/j.jpowsour.2012.01.155
12. Medri V, Mazzocchi M, Bellosi A (2011) ZrB2-based sponges and lightweight devices. Int J

Appl Ceram Technol 8:815–823

13. Franks G V, Tallon C, Studart AR, et al (2017) Colloidal processing: enabling complex shaped ceramics with unique multiscale structures. J Am Ceram Soc 100:458–490 . doi: 10.1111/jace.14705
14. Rouquerol J, Avnir D, C WF, et al (1994) Recommendations for the characterization of porous solids (Technical Report). Pure Appl Chem 66:1739–1758 . doi: 10.1351/pac199466081739
15. Li X, Yu J, Jaroniec M (2016) Hierarchical photocatalysts. Chem Soc Rev 45:2603–2636
16. Zheng W, Yan Z, Dai Y, et al (2017) Interpenetrated Networks between Graphitic Carbon Infilling and Ultrafine TiO2Nanocrystals with Patterned Macroporous Structure for High-Performance Lithium Ion Batteries. ACS Appl Mater Interfaces 9:20491–20500 . doi: 10.1021/acsami.7b02345
17. Ferrari L, Barbato M, Esser B, et al (2016) Sandwich structured ceramic matrix composites with periodic cellular ceramic cores: an active cooled thermal protection for space vehicles. Compos Struct 154:61–68 . doi: https://doi.org/10.1016/j.compstruct.2016.07.043
18. Tobin A, Feldman C, Russak M, Reichman J (1973) Development of a Closed Pore Insulation Material. NASA Contract Reports
19. Green DJ, Colombo P (2003) Cellular ceramics: Intriguing structures, novel properties, and innovative applications. MRS Bull 28:296–300
20. Bourret J, Tessier-Doyen N, Naït-Ali B, et al (2013) Effect of the pore volume fraction on the thermal conductivity and mechanical properties of kaolin-based foams. J Eur Ceram Soc 33:1487–1495 . doi: https://doi.org/10.1016/j.jeurceramsoc.2012.10.022
21. Gauckler LJ, Waeber MM, Conti C, Jacob-Duliere M (1985) Ceramic Foam for Molten Metal Filtration. J Met 37:47–50
22. Parlett CMA, Wilson K, Lee AF (2013) Hierarchical porous materials: catalytic applications. Chem Soc Rev 42:3876–3893 . doi: 10.1039/C2CS35378D
23. Zhou Q, Chen W, Xu L, Peng S (2013) Hydrothermal Synthesis of Various Hierarchical ZnO Nanostructures and Their Methane Sensing Properties. Sensors (Switzerland) 13:6171–82

24. Li Y, Liu T, Zhang H (2016) New insight into gas sensing performance of nanoneedle-assembled and nanosheet-assembled hierarchical SnO2structures. Mater Lett 176:9–12
25. Lewis JA (2000) Colloidal processing of ceramics. J Am Ceram Soc 83:2341–2359 . doi: 10.1111/j.1151-2916.2000.tb01560.x
26. Verwey EJW, Overbeek JTG (1946) Long distance forces acting between colloidal particles. Trans Faraday Soc 42:B117–B123
27. Derjaguin B, Landau L (1993) Theory of the stability of strongly charged lyophobic sols and of the adhesion of strongly charged particles in solutions of electrolytes. Prog Surf Sci 43:30–59
28. (2012) Colloidal Stability: DLVO Theory. In: Silver Colloids. http://www.silver-colloids.com/Tutorials/Intro/pcs8.html. Accessed 8 Jun 2018
29. Sun J, Velamakanni B V, Gerberich WW, Francis LF (2004) Aqueous latex/ceramic nanoparticle dispersions: colloidal stability and coating properties. J Colloid Interface Sci 280:387–399 . doi: https://doi.org/10.1016/j.jcis.2004.08.014
30. Karimian H, Babaluo AA (2007) Halos mechanism in stabilizing of colloidal suspensions: Nanoparticle weight fraction and pH effects. J Eur Ceram Soc 27:19–25 . doi: https://doi.org/10.1016/j.jeurceramsoc.2006.05.109
31. Leong YK (1994) Exploitation of interparticle forces in the processing of colloidal ceramic materials. Mater Des 15:141–7
32. Pal N, Bhaumik A (2013) Soft templating strategies for the synthesis of mesoporous materials: Inorganic, organic–inorganic hybrid and purely organic solids. Adv Colloid Interface Sci 189–190:21–41 . doi: https://doi.org/10.1016/j.cis.2012.12.002
33. Ramesh D, Prasad G, Raaj A (2015) Thermal Conductivity Enchancement Techniques and thermal Aging of Nanofluids - A Review. Int J Mech Prod Eng 3:124–127
34. Peng T, Zhao D, Dai K, et al (2005) Synthesis of titanium dioxide nanoparticles with mesoporous anatase wall and high photocatalytic activity. J Phys Chem B 109:4947–52
35. Sepulveda P, Ortega FS, Innocentini MDM, Pandolfelli VC (2000) Properties of highly porous hydroxyapatite obtained by the gelcasting of foams. J Am Ceram Soc 83:3021–3024
36. Idesaki A, Colombo P (2012) Synthesis of a Ni-Containing Porous SiOC Material From

Polyphenylmethylsiloxane by a Direct Foaming Technique. Adv Eng Mater 14:1116–22

37. de Moraes E, Li D, Colombo P, Shen Z (2015) Silicon nitride foams from emulsions sintered by rapid intense thermal radiation. J Eur Ceram Soc 35:3263–72
38. Towata A, Sivakumar M, Yasui K, et al (2007) Ultrasound induced formation of paraffin emulsion droplets as template for the preparation of porous zirconia. Ultrason Sonochem 14:705–710
39. Zeschky J, Höfner T, Arnold C, et al (2005) Polysilsesquioxane derived ceramic foams with gradient porosity. Acta Mater 53:927–937 . doi: https://doi.org/10.1016/j.actamat.2004.10.039
40. Ghosh S, Roy M, Naskar MK (2014) Template-free synthesis of mesoporous single-crystal CuO particles with dumbbell-shaped morphology. Mater Lett 132:98–101
41. Yang T, Huang Z, Liu Y, et al (2014) Controlled synthesis of porous FeCO3 microspheres and the conversion to α-Fe2O3 with unconventional morphology. Ceram Int 40:11975–83
42. Liu H, Zhang H, Xu H, et al (2018) Hierarchically nanostructured vanadium nitride microspheres assembled with porous nanosheets fabricated by a template-free route. Ceram Int 44:1583–1588 . doi: https://doi.org/10.1016/j.ceramint.2017.10.078
43. Fu LJ, Zhang T, Cao Q, et al (2007) Preparation and characterization of three-dimensionally ordered mesoporous titania microparticles as anode material for lithium ion battery. Electrochem commun 9:2140–2144 . doi: http://dx.doi.org/10.1016/j.elecom.2007.06.009
44. Lee D-W, Park S-J, Ihm S-K, Lee K-H (2007) Synthesis of bimodal mesoporous titania with high thermal stability via replication of citric acid-templated mesoporous silica. Chem Mater 19:937–941 . doi: 10.1021/cm062465f
45. Zhao W, Lang M, Li Y, et al (2009) Fabrication of uniform hollow mesoporous silica spheres and ellipsoids of tunable size through a facile hard-templating route. J Mater Chem 19:2778–2783
46. Shin Y, Exarhos GJ (2007) Conversion of cellulose materials into nanostructured ceramics by biomineralization. Cellulose 14:269–279 . doi: 10.1007/s10570-006-9101-0
47. Sieber H, Rambo C, Cao J, et al (2002) Manufacturing of porous oxide ceramics by replication

of plant morphologies. Key Eng Mater 206–213:2009–12

48. Gaudillere C, Serra JM (2016) Freeze-casting: Fabrication of highly porous and hierarchical ceramic supports for energy applications. Bol la Soc Esp Ceram y Vidr 55:45–54
49. Tallon C, Franks G V (2011) Recent trends in shape forming from colloidal processing: A review. Nippon Seramikkusu Kyokai Gakujutsu Ronbunshi/Journal Ceram Soc Japan 119:147–160
50. Li WL, Lu K, Walz JY (2012) Freeze casting of porous materials: Review of critical factors in microstructure evolution. Int Mater Rev 57:37–60 . doi: 10.1179/1743280411Y.0000000011
51. Deville S (2008) Freeze-casting of porous ceramics: a review of current achievements and issues. Adv Eng Mater 10:155–69
52. Liu R, Xu T, Wang C (2016) A review of fabrication strategies and applications of porous ceramics prepared by freeze-casting method. Ceram Int 42:2907–2925
53. Tallon C, Moreno R, Nieto MI (2009) Shaping of porous alumina bodies by freeze casting. Adv Appl Ceram 108:307–313 . doi: 10.1179/174367608x369280
54. Naglieri V, Bale HA, Gludovatz B, et al (2013) On the development of ice-templated silicon carbide scaffolds for nature-inspired structural materials. Acta Mater 61:6948–57
55. Ren L, Zeng Y-P, Jiang D (2009) Preparation of porous TiO2 by a novel freeze casting. Ceram Int 35:1267–70
56. Hu Z, Hua Z, Cai S, et al (2012) Fabrication of three-dimensionally ordered macro-/mesoporous titania monoliths by a dual-templating approach. In: Materials Research Society Symposium Proceedings. Materials Research Society, Key Lab. for Nanomaterials, Ministry of Education, Beijing University of Chemical Technology, Beijing 100029, ChinaDepartment of Chemical and Environmental Engineering, University of California at Riverside, Riverside, CA 92521, United States, pp 33–38
57. Naglieri V, Colombo P (2017) Ceramic microspheres with controlled porosity by emulsion-ice templating. J Eur Ceram Soc 37:2559–68
58. Wakefield G, Green M, Lipscomb S, Flutter B (2004) Modified titania nanomaterials for sunscreen applications - Reducing free radical generation and DNA damage. In: Materials

Science and Technology. pp 985–988

59. Faure B, Salazar-Alvarez G, Ahniyaz A, et al (2013) Dispersion and surface functionalization of oxide nanoparticles for transparent photocatalytic and UV-protecting coatings and sunscreens. Sci Technol Adv Mater 14:
60. Sabet M, Salavati-Niasari M (2015) Deposition of Lead Sulfide Nanostructure Films on TiO2 Surface via Different Chemical Methods due to Improving Dye-Sensitized Solar Cells Efficiency. 169:168–179
61. Wang C-T, Siao H-L (2014) Improving photovoltaic performance of titanium oxide thin films by integration of iron doping and dye sensitization. 244:63–68
62. Zhang Z, Zuo F, Feng P (2010) Hard template synthesis of crystalline mesoporous anatase TiO2 for photocatalytic hydrogen evolution. J Mater Chem 20:2206–2212 . doi: 10.1039/B921157H
63. Pan H (2016) Principles on design and fabrication of nanomaterials as photocatalysts for water-splitting. Renew Sustain Energy Rev 57:584–601 . doi: https://doi.org/10.1016/j.rser.2015.12.117
64. Ahmad H, Kamarudin SK, Minggu LJ, Kassim M (2015) Hydrogen from photo-catalytic water splitting process: A review. Renew Sustain Energy Rev 43:599–610 . doi: https://doi.org/10.1016/j.rser.2014.10.101
65. Maeda K (2011) Photocatalytic water splitting using semiconductor particles: History and recent developments. J Photochem Photobiol C Photochem Rev 12:237–268 . doi: https://doi.org/10.1016/j.jphotochemrev.2011.07.001
66. Yan H, Wang X, Yao M, Yao X (2013) Band structure design of semiconductors for enhanced photocatalytic activity: The case of TiO2. Prog Nat Sci Mater Int 23:402–407 . doi: 10.1016/j.pnsc.2013.06.002
67. Choi H, Stathatos E, Dionysiou DD (2006) Sol–gel preparation of mesoporous photocatalytic TiO2 films and TiO2/Al2O3 composite membranes for environmental applications. Appl Catal B Environ 63:60–67 . doi: http://dx.doi.org/10.1016/j.apcatb.2005.09.012
68. Zhang RY, Elzatahry AA, Al-Deyab SS, Zhao DY (2012) Mesoporous titania: From synthesis to application. Nano Today 7:344–366 . doi: 10.1016/j.nantod.2012.06.012

69. Gupta NM (2017) Factors affecting the efficiency of a water splitting photocatalyst: A perspective. Renew Sustain Energy Rev 71:585–601 . doi: https://doi.org/10.1016/j.rser.2016.12.086

70. Yu J, Su Y, Cheng B (2007) Template-free fabrication and enhanced photocatalytic activity of hierarchical macro-/mesoporous titania. Adv Funct Mater 17:1984–1990 . doi: 10.1002/adfm.200600933

71. Li X-Y, Chen L-H, Li Y, et al (2012) Self-generated hierarchically porous titania with high surface area: Photocatalytic activity enhancement by macrochannel structure. J Colloid Interface Sci 368:128–138 . doi: 10.1016/j.jcis.2011.10.018

72. Luo Y, Huang J (2014) Hierarchical-Structured Anatase-Titania/Cellulose Composite Sheet with High Photocatalytic Performance and Antibacterial Activity. Chem – A Eur J 21:2568–2575 . doi: 10.1002/chem.201405066

73. Bakardjieva S, Stengl V, Szatmary L, et al (2006) Transformation of brookite-type TiO2 nanocrystals to rutile: correlation between microstructure and photoactivity. J Mater Chem 16:1709–1716 . doi: 10.1039/b514632a

74. Hurum DC, Agrios AG, Gray KA, et al (2003) Explaining the enhanced photocatalytic activity of Degussa P25 mixed-phase TiO2 using EPR. J Phys Chem B 107:4545–4549 . doi: 10.1021/jp0273934

75. Khataee AR, Aleboyeh H, Aleboyeh A (2009) Crystallite phase-controlled preparation, characterisation and photocatalytic properties of titanium dioxide nanoparticles. J Exp Nanosci 4:121–137 . doi: 10.1080/17458080902929945

76. Di Paola A, Bellardita M, Palmisano L (2013) Brookite, the least known TiO2 photocatalyst. Catalysts 3:36–73 . doi: 10.3390/catal3010036

77. Boppella R, Basak P, Manorama S V (2012) Viable method for the synthesis of biphasic TiO2 nanocrystals with tunable phase composition and enabled visible-light photocatalytic performance. ACS Appl Mater Interfaces 4:1239–1246

78. Wang H, Zhang L, Chen Z, et al (2014) Semiconductor heterojunction photocatalysts: design, construction, and photocatalytic performances. Chem Soc Rev 43:5234–5244 . doi: 10.1039/C4CS00126E

79. Ding X, Liu X, He Y (1996) Grain size dependence of anatase-to-rutile structural transformation in gel-derived nanocrystalline titania powders. J Mater Sci Lett 15:1789–1791 . doi: 10.1007/BF00275343

80. Ding X-Z, Qi Z-Z, He Y-Z (1995) Effect of hydrolysis water on the preparation of nano-crystalline titania powders via a sol-gel process. J Mater Sci Lett 14:21–22 . doi: 10.1007/BF02565273

81. Kumar SG, Rao KSRK (2014) Polymorphic phase transition among the titania crystal structures using a solution-based approach: from precursor chemistry to nucleation process. Nanoscale 6:11574–11632 . doi: 10.1039/C4NR01657B

82. Kumar KNP, Keizer K, Burggraaf AJ (1994) Stabilization of the porous texture of nanostructured titanic by avoiding a phase transformation. J Mater Sci Lett 13:59–61 . doi: 10.1007/BF02352920

83. Hu Y, Tsai HL, Huang CL (2003) Phase transformation of precipitated TiO2 nanoparticles. Mater Sci Eng A 344:209–214 . doi: http://dx.doi.org/10.1016/S0921-5093(02)00408-2

84. Chiarello GL, Di Paola A, Palmisano L, Selli E (2011) Effect of titanium dioxide crystalline structure on the photocatalytic production of hydrogen. Photochem Photobiol Sci 10:355–360 . doi: 10.1039/C0PP00154F

85. Zhang J, Zhou P, Liu J, Yu J (2014) New understanding of the difference of photocatalytic activity among anatase, rutile and brookite TiO2. Phys Chem Chem Phys 16:20382–20386 . doi: 10.1039/C4CP02201G

86. Mitsuhashi T, Kleppa OJ (1979) Transformation enthalpies of the TiO2 polymorphs. J Am Ceram Soc 62:356–7

87. Zhang H, Banfield JF (2000) Understanding polymorphic phase transformation behavior during growth of nanocrystalline aggregates: insights from TiO2. J Phys Chem B 104:3481–7

88. Zhu K-R, Zhang M-S, Hong J-M, Yin Z (2005) Size effect on phase transition sequence of TiO2 nanocrystal. Mater Sci Eng A 403:87–93 . doi: 10.1016/j.msea.2005.04.029

89. Finnegan MP, Zhang H, Banfield JF (2007) Phase stability and transformation in titania nanoparticles in aqueous solutions dominated by surface energy. J Phys Chem C 111:1962–

1968

90. Preocanin T, Kallay N (2006) Point of Zero Charge and Surface Charge Density of TiO2 in Aqueous Electrolyte Solution as Obtained by Porentiometric Mass Titration. Croat Chem ACTA 79 (1):95–106
91. Fernández-Nieves A, de las Nieves FJ, Richter C (1998) Point of zero charge estimation for a TiO2/water interface. In: Koper GJM, Bedeaux D, Cavaco C, Sager WFC (eds) Trends in Colloid and Interface Science XII. Steinkopff, Darmstadt, pp 21–24
92. Lebrette S, Pagnoux C, Abélard P (2004) Stability of aqueous TiO2 suspensions: influence of ethanol. J Colloid Interface Sci 280:400–408 . doi: https://doi.org/10.1016/j.jcis.2004.07.033
93. Janusz W, Galgan A, Skwarek E (2004) Effects of the adsorption of Ba(2+) ions on the electrical double layer at the 4th group metal oxide/electrolyte interface. Adsorpt Sci Technol 22:795–806 . doi: 10.1260/0263617053498989
94. Zhang H, Banfield JF (2000) Phase transformation of nanocrystalline anatase-to-rutile via combined interface and surface nucleation. J Mater Res 15:437–48
95. Zhang H, Banfield JF (2007) Polymorphic transformations and particle coarsening in nanocrystalline titania ceramic powders and membranes. J Phys Chem C 111:6621–9
96. Wolff K, Heljo P, Lupo D (2013) Growth of ultra-thin titanium dioxide films by complete anodic oxidation of titanium layers on conductive substrates. In: Materials Research Society Symposium Proceedings. Boston, MA, United states, pp 159–164
97. Im JH, Kang E, Yang SJ, et al (2014) Simple preparation of anatase titanium dioxide nanoparticles by heating titanium-organic frameworks. Bull Korean Chem Soc 35:2477–2480
98. Zheng W, Liu X, Yan Z, Zhu L (2009) Ionic Liquid-Assisted Synthesis of Large-Scale TiO2 Nanoparticles with Controllable Phase by Hydrolysis of TiCl4. ACS Nano 3:115–122 . doi: 10.1021/nn800713w
99. Li G, Liu Z, Zhang Z, Yan X (2009) Preparation of Titania Nanotube Arrays by the Hydrothermal Method. Chinese J Catal 30:37–42 . doi: https://doi.org/10.1016/S1872-2067(08)60088-1

100. Rashad MM, Shalan AE (2013) Surfactant-assisted hydrothermal synthesis of titania nanoparticles for solar cell applications. J Mater Sci Mater Electron 24:3189–3194
101. Shin H, Jung HS, Hong KS, Lee J-K (2004) Crystallization process of TiO2 nanoparticles in an acidic solution. Chem Lett 33:1382–1383 . doi: 10.1246/cl.2004.1382
102. Khalil KMS, Baird T, Zaki MI, et al (1998) Synthesis and characterization of catalytic titanias via hydrolysis of titanium (IV) isopropoxide. Colloids Surfaces A Physicochem Eng Asp 132:31–44 . doi: http://dx.doi.org/10.1016/S0927-7757(97)00156-8
103. Vorkapic D, Matsoukas T (1998) Effect of Temperature and Alcohols in the Preparation of Titania Nanoparticles from Alkoxides. J Am Ceram Soc 81:2815–2820 . doi: 10.1111/j.1151-2916.1998.tb02701.x
104. Song KC, Pratsinis SE (2000) The Effect of Alcohol Solvents on the Porosity and Phase Composition of Titania. J Colloid Interface Sci 231:289–298 . doi: http://dx.doi.org/10.1006/jcis.2000.7147
105. Karmakar B, Ganguli D (1985) Alkoxide hydrolysis and preparation of TiO2 powders. Trans Indian Ceram Soc 44:10–14 . doi: 10.1080/0371750X.1985.10822720
106. Hanaor DAH, Chironi I, Karatchevtseva I, et al (2012) Single and mixed phase TiO2 powders prepared by excess hydrolysis of titanium alkoxide. Adv Appl Ceram 111:149–158
107. Song KC, Pratsinis SE (2000) Synthesis of bimodally porous titania powders by hydrolysis of titanium tetraisopropoxide. J Mater Res 15:2322–2329 . doi: 10.1557/JMR.2000.0334
108. Collins A, Carriazo D, Davis S a, Mann S (2004) Spontaneous template-free assembly of ordered macroporous titania. Chem Commun (Camb) 44:568–569 . doi: 10.1039/b315018f
109. Grzeskowiak M, Wrobel RJ, Grzechulska J, Przepiorski J (2014) Preparation and characterization of titania powders obtained via hydrolysis of titanium tetraisopropoxide. Mater Sci Pol 32:71–79 . doi: 10.2478/s13536-013-0163-z
110. Ragauskas AJ (2016) Physicochemical Structural Changes of Cellulosic Substrates during Enzymatic Saccharification. J Appl Biotechnol Bioeng 1: . doi: 10.15406/jabb.2016.01.00015
111. Habibi Y, Lucia LA, Rojas OJ (2010) Cellulose nanocrystals: chemistry, self-assembly, and applications. Chem Rev 110:3479–3500 . doi: 10.1021/cr900339w

112. Reid MS, Villalobos M, Cranston ED (2016) Cellulose nanocrystal interactions probed by thin film swelling to predict dispersibility. Nanoscale 8:12247–12257 . doi: 10.1039/C6NR01737A
113. Phan-Xuan T, Thuresson A, Skepo M, et al (2016) Aggregation behavior of aqueous cellulose nanocrystals: the effect of inorganic salts. Cellulose 23:3653–3663
114. Zhong L, Fu S, Peng X, et al (2012) Colloidal stability of negatively charged cellulose nanocrystalline in aqueous systems. Carbohydr Polym 90:644–649
115. Xu Y, Atrens AD, Stokes JR (2017) Rheology and microstructure of aqueous suspensions of nanocrystalline cellulose rods. J Colloid Interface Sci 496:130–140 . doi: https://doi.org/10.1016/j.jcis.2017.02.020
116. Liu D, Chen X, Yue Y, et al (2011) Structure and rheology of nanocrystalline cellulose. Carbohydr Polym 84:316–322
117. Shafiei-Sabet S, Hamad WY, Hatzikiriakos SG (2012) Rheology of nanocrystalline cellulose aqueous suspensions. Langmuir 28:17124–17133
118. Hasani M, Cranston ED, Westman G, Gray DG (2008) Cationic surface functionalization of cellulose nanocrystals. Soft Matter 4:2238–2244
119. Habibi Y, Chanzy H, Vignon MR (2006) TEMPO-mediated surface oxidation of cellulose whiskers. Cellulose 13:679–687
120. Moon RJ, Martini A, Nairn J, et al (2011) Cellulose nanomaterials review: structure, properties and nanocomposites. Chem Soc Rev 40:3941–3994 . doi: 10.1039/C0CS00108B
121. Shopsowitz KE, Kelly JA, Hamad WY, MacLachlan MJ (2014) Biopolymer Templated Glass with a Twist: Controlling the Chirality, Porosity, and Photonic Properties of Silica with Cellulose Nanocrystals. Adv Funct Mater 24:327–338 . doi: 10.1002/adfm.201301737
122. Lagerwall JPF, Schutz C, Salajkova M, et al (2014) Cellulose nanocrystal-based materials: From liquid crystal self-assembly and glass formation to multifunctional thin films. NPG Asia Mater 6:
123. Ljungberg N, Bonini C, Bortolussi F, et al (2005) New nanocomposite materials reinforced with cellulose whiskers in atactic polypropylene: Effect of surface and dispersion characteristics. Biomacromolecules 6:2732–2739

124. Sapkota J, Kumar S, Weder C, Foster EJ (2015) Influence of processing conditions on properties of poly (Vinyl acetate)/cellulose nanocrystal nanocomposites. Macromol Mater Eng 300:562–571
125. Sapkota J, Jorfi M, Weder C, Foster EJ (2014) Reinforcing poly(ethylene) with cellulose nanocrystals. Macromol Rapid Commun (Germany) 35:1747–53
126. Nicharat A, Sapkota J, Foster EJ (2016) Pre-mixing and masterbatch approaches for reinforcing poly(vinyl acetate) with cellulose based fillers. Ind Crops Prod 93:244–250 . doi: http://dx.doi.org/10.1016/j.indcrop.2016.02.061
127. Natterodt JC, Meesorn W, Zoppe JO, Weder C (2018) Functionally Graded Polyurethane/Cellulose Nanocrystal Composites. Macromol Mater Eng
128. Natterodt JC, Sapkota J, Foster EJ, Weder C (2017) Polymer Nanocomposites with Cellulose Nanocrystals Featuring Adaptive Surface Groups. Biomacromolecules 18:517–525
129. Cao Y, Zavattieri P, Youngblood J, et al (2016) The relationship between cellulose nanocrystal dispersion and strength. Constr Build Mater 119:71–79
130. Hajian A, Lindstrom SB, Pettersson T, et al (2017) Understanding the Dispersive Action of Nanocellulose for Carbon Nanomaterials. Nano Lett 17:1439–1447
131. Hu Z, Ballinger S, Pelton R, Cranston ED (2015) Surfactant-enhanced cellulose nanocrystal Pickering emulsions. J Colloid Interface Sci 439:139–148
132. Li X, Li J, Gong J, et al (2018) Cellulose nanocrystals (CNCs) with different crystalline allomorph for oil in water Pickering emulsions. Carbohydr Polym 183:303–310 . doi: https://doi.org/10.1016/j.carbpol.2017.12.085
133. Angkuratipakorn T, Sriprai A, Tantrawong S, et al (2017) Fabrication and characterization of rice bran oil-in-water Pickering emulsion stabilized by cellulose nanocrystals. Colloids Surfaces A Physicochem Eng Asp 522:310–319
134. Ojala J, Sirviö JA, Liimatainen H (2016) Nanoparticle emulsifiers based on bifunctionalized cellulose nanocrystals as marine diesel oil–water emulsion stabilizers. Chem Eng J 288:312–320 . doi: https://doi.org/10.1016/j.cej.2015.10.113
135. Lin N, Huang J, Chang PR, et al (2011) Effect of polysaccharide nanocrystals on structure, properties, and drug release kinetics of alginate-based microspheres. Colloids Surfaces B

Biointerfaces 85:270–279 . doi: https://doi.org/10.1016/j.colsurfb.2011.02.039

136. Lin N, Dufresne A (2013) Supramolecular Hydrogels from In Situ Host–Guest Inclusion between Chemically Modified Cellulose Nanocrystals and Cyclodextrin. Biomacromolecules 14:871–880 . doi: 10.1021/bm301955k
137. Taheri A, Mohammadi M (2014) The Use of Cellulose Nanocrystals for Potential Application in Topical Delivery of Hydroquinone. Chem Biol Drug Des 86:102–106 . doi: 10.1111/cbdd.12466
138. Drogat N, Granet R, Le Morvan C, et al (2012) Chlorin-PEI-labeled cellulose nanocrystals: Synthesis, characterization and potential application in PDT. Bioorg Med Chem Lett 22:3648–3652 . doi: https://doi.org/10.1016/j.bmcl.2012.04.044
139. Zhou Z, Peng X, Zhong L, et al (2016) Electrospun cellulose acetate supported Ag@AgCl composites with facet-dependent photocatalytic properties on degradation of organic dyes under visible-light irradiation. Carbohydr Polym 136:322–328
140. Kong L, Zhang C, Wang J, et al (2014) Ultrahigh intercalation pseudocapacitance of mesoporous orthorhombic niobium pentoxide from a novel cellulose nanocrystal template. Mater Chem Phys
141. Busuioc C, Ghitulica CD, Stoica A, et al (2018) Calcium phosphates grown on bacterial cellulose template. Ceram Int 44:9433–9441
142. Liang H, Liu K, Ni Y (2015) Synthesis of mesoporous α-Fe2O3via sol-gel methods using cellulose nano-crystals (CNC) as template and its photo-catalytic properties. Mater Lett 159:218–220
143. Kale BM, Wiener J, Militky J, et al (2016) Coating of cellulose-TiO2 nanoparticles on cotton fabric for durable photocatalytic self-cleaning and stiffness. Carbohydr Polym 150:107–113 . doi: https://doi.org/10.1016/j.carbpol.2016.05.006
144. Boriboon D, Vongsetskul T, Limthongkul P, et al (2018) Cellulose ultrafine fibers embedded with titania particles as a high performance and eco-friendly separator for lithium-ion batteries. Carbohydr Polym 189:145–151 . doi: https://doi.org/10.1016/j.carbpol.2018.01.077
145. Marques PAAP, Trindade T, Neto CP (2006) Titanium dioxide/cellulose nanocomposites

prepared by a controlled hydrolysis method. Compos Sci Technol 66:1038–1044 . doi: https://doi.org/10.1016/j.compscitech.2005.07.029

146. Liu S, Tao D, Bai H, Liu X (2012) Cellulose-nanowhisker-templated synthesis of titanium dioxide/cellulose nanomaterials with promising photocatalytic abilities. J Appl Polym Sci 126:281–9
147. Martakov IS, Torlopov MA, Mikhaylov VI, et al (2017) Interaction of cellulose nanocrystals with titanium dioxide and peculiarities of hybrid structures formation. J Sol-Gel Sci Technol. doi: 10.1007/s10971-017-4447-3
148. Yan Y, Hao B, Chen G (2011) Biomimetic synthesis of titania with chitosan-mediated phase transformation at room temperature. J Mater Chem 21:10755–10760 . doi: 10.1039/C1JM11056J
149. Goncalves G, Marques PAAP, Pinto RJB, et al (2009) Surface modification of cellulosic fibres for multi-purpose TiO2 based nanocomposites. Compos Sci Technol 69:1051–1056 . doi: https://doi.org/10.1016/j.compscitech.2009.01.020
150. Uddin MJ, Cesano F, Bonino F, et al (2007) Photoactive TiO2 films on cellulose fibres: synthesis and characterization. J Photochem Photobiol A Chem 189:286–294 . doi: https://doi.org/10.1016/j.jphotochem.2007.02.015
151. Mohamed MA, W. Salleh WN, Jaafar J, et al (2016) Regenerated cellulose membrane as bio-template for in-situ growth of visible-light driven C-modified mesoporous titania. Carbohydr Polym 146:166–173 . doi: https://doi.org/10.1016/j.carbpol.2016.03.050
152. Shopsowitz KE, Stahl A, Hamad WY, MacLachlan MJ (2012) Hard templating of nanocrystalline titanium dioxide with chiral nematic ordering. Angew Chemie - Int Ed 51:6886–6890 . doi: 10.1002/anie.201201113
153. Gu Y, Liu X, Niu T, Huang J (2010) Titania nanotube/hollow sphere hybrid material: Dual-template synthesis and photocatalytic property. Mater Res Bull 45:536–541 . doi: https://doi.org/10.1016/j.materresbull.2010.02.009
154. Ivanova A, Fravventura MC, Fattakhova-Rohlfing D, et al (2015) Nanocellulose-Templated Porous Titania Scaffolds Incorporating Presynthesized Titania Nanocrystals. Chem Mater 27:6205–6212

155. Huang H, Liu X, Huang J (2011) Tubular structured hierarchical mesoporous titania material derived from natural cellulosic substances and application as photocatalyst for degradation of methylene blue. Mater Res Bull 46:1814–1818 . doi: https://doi.org/10.1016/j.materresbull.2011.07.045
156. Caruso RA, Schattka JH (2000) Cellulose Acetate Templates for Porous Inorganic Network Fabrication. Adv Mater 12:1921–1923 . doi: 10.1002/1521-4095(200012)12:24<1921::AID-ADMA1921>3.0.CO;2-B
157. Chen X, Kuo D-H, Lu D (2016) N-doped mesoporous TiO2 nanoparticles synthesized by using biological renewable nanocrystalline cellulose as template for the degradation of pollutants under visible and sun light. Chem Eng J 295:192–200 . doi: https://doi.org/10.1016/j.cej.2016.03.047
158. Mohamed MA, Abd Mutalib M, Mohd Hir ZA, et al (2017) An overview on cellulose-based material in tailoring bio-hybrid nanostructured photocatalysts for water treatment and renewable energy applications. Int J Biol Macromol 103:1232–1256 . doi: https://doi.org/10.1016/j.ijbiomac.2017.05.181
159. Ivanova A, Fattakhova-Rohlfing D, Kayaalp BE, et al (2014) Tailoring the Morphology of Mesoporous Titania Thin Films through Biotemplating with Nanocrystalline Cellulose. J Am Chem Soc 136:5930–5937 . doi: 10.1021/ja411292u
160. Yoon YH, Lee SY, Gwon JG, et al (2018) Mesoporous titania films templated by cellulose nanocrystals: morphological and spectrophotometric properties. Cellulose. doi: 10.1007/s10570-018-2035-5
161. Gu YQ, Huang JG (2010) Natural Cellulosic Substance Derived Nanostructured Materials. Nanostructured Biomater 133–164 . doi: Doi 10.1007/978-3-642-05012-1_4
162. Swanson HE, Morris MC, Evans EH, Ulmer L (1964) Standard X-ray diffraction powder patterns. Section 3 - data for 51 substances. Natl Bur Stand Monogr 57
163. Swanson HEE, McMurdie HFF, Morris MCC, Evans EHH (1969) Standard X-ray diffraction powder patterns. Nat. Bur. Stand., Washington, DC, USA
164. Foster EJ, Moon RJ, Agarwal UP, et al (2018) Current characterization methods for cellulose nanomaterials. Chem Soc Rev 47:2609–2679 . doi: 10.1039/C6CS00895J

165. Foster EJ, Zahed N, Tallon C (2018) The Transformative and Versatile Role of Cellulose Nanomaterials in Templating and Shaping Multiscale Mesostructured Ceramics. Small 0:1802068 . doi: 10.1002/smll.201802068
166. Klemm D, Schumann D, Kramer F, et al (2009) Nanocellulose Materials - Different Cellulose, Different Functionality. Macromol Symp 280:60–71 . doi: 10.1002/masy.200950608
167. Klemm D, Kramer F, Moritz S, et al (2011) Nanocelluloses: a new family of nature-based materials. Angew Chem Int Ed Engl 50:5438–5466 . doi: 10.1002/anie.201001273
168. Huang J, Kunitake T (2003) Nano-precision replication of natural cellulosic substances by metal oxides. J Am Chem Soc 125:11834–11835 . doi: 10.1021/ja037419k
169. Espino-Perez E, Bras J, Almeida G, et al (2016) Cellulose nanocrystal surface functionalization for the controlled sorption of water and organic vapours. Cellulose 23:2955–2970 . doi: 10.1007/s10570-016-0994-y
170. Peng BL, Dhar N, Liu HL, Tam KC (2011) Chemistry and applications of nanocrystalline cellulose and its derivatives: A nanotechnology perspective. Can J Chem Eng 89:1191–1206 . doi: 10.1002/cjce.20554
171. Virkutyte J, Jegatheesan V, Varma RS (2012) Visible light activated TiO2/microcrystalline cellulose nanocatalyst to destroy organic contaminants in water. Bioresour Technol 113:288–293 . doi: https://doi.org/10.1016/j.biortech.2011.12.090